Copper foam catalysts in CO_2 electroreduction – Development of an experimental measuring procedure and the structural and chemical modification of the catalyst

Kupferschaumkatalysatoren in der elektrochemischen CO_2 Reduktion – Entwicklung eines experimentellen Messkonzepts und der strukturellen und chemische Modifikation des Katalysator.

Dissertation – Dipl.-Chem. Sascha-Dominic Straub

TECHNISCHE
UNIVERSITÄT
DARMSTADT

vom Fachbereich Chemie
der Technischen Universität Darmstadt

zur Erlangung des Grades
Doktor-Ingenieur
(Dr.-Ing.)

Dissertation
von Diplom-Chemiker Sascha-Dominic Straub

Erstgutachter: Prof. Dr.-Ing. Dipl.-Kfm. Bastian J. M. Etzold
Zweitgutachter: Prof. Dr. Karl Mayrhofer

Darmstadt 2021

Tag der Einreichung: 25.Mai 2021

Tag der mündlichen Prüfung: 12.Juli 2021

Straub, Sascha-Dominic: Copper foam catalysts in CO2 electroreduction – Development of an experimental measuring procedure and the structural and chemical modification of the catalyst
Darmstadt, Technische Universität Darmstadt
Jahr der Veröffentlichung der Dissertation auf TUprints: 2021
Tag der mündlichen Prüfung: 12.07.2021

„Ich beschäftige mich nicht mit dem, was getan worden ist.

Mich interessiert, was getan werden muss.“

\- Marie Curie -

Diese Arbeit wurde am Ernst-Berl-Institut für Technische und Makromolekulare Chemie der Technischen Universität Darmstadt unter Leitung von Herrn Prof. Dr.-Ing. Dipl.-Kfm. Bastian J. M. Etzold in der Zeit vom 01. November 2016 bis 31. Oktober 2019 durchgeführt.

Teile dieser Arbeit wurden bereits veröffentlicht bzw. auf Tagungen vorgestellt:

S.-D. Straub, M. Curic, G.-R. Zhang, A. Reichert, M. Löffler, K. Mayrhofer, I. Katsounaros, B. J. M. Etzold: *"Tuning morphology of electrodeposited Cu foams for electrochemical reduction of* CO_2*"*, EuropaCat 2019, Aachen, Deutschland, 18. – 23.08.2019.

S.-D. Straub, G.-R. Zhang, B. J. M. Etzold: *"Influence of IL-modification on Cu based catalysts for the electrochemical reduction of* CO_2*"*, 69th Annual Meeting of the International Society of Electrochemistry, Bologna, Italien, 02. – 07.09.2018.

G.-R. Zhang, S.-D. Straub, L.-L. Shen, Y. Hermans, P. Schmatz, A. M. Reichert, J. P. Hofmann, I. Katsounaros, B. J. M. Etzold, *Angew. Chem. Int. Ed.*, **2020**, 59, 18095 – 18102.

Erklärungen laut Promotionsordnung

§8 Abs. 1 lit. c PromO

Ich versichere hiermit, dass die elektronische Version meiner Dissertation mit der schriftlichen Version übereinstimmt und für die Durchführung des Promotionsverfahrens vorliegt.

§8 Abs. 1 lit. d PromO

Ich versichere hiermit, dass zu einem vorherigen Zeitpunkt noch keine Promotion versucht wurde und zu keinem früheren Zeitpunkt an einer in- oder ausländischen Hochschule eingereicht wurde. In diesem Fall sind nähere Angaben über Zeitpunkt, Hochschule, Dissertationsthema und Ergebnis dieses Versuchs mitzuteilen.

§9 Abs. 1 PromO

Ich versichere hiermit, dass die vorliegende Dissertation selbstständig und nur unter Verwendung der angegebenen Quellen verfasst wurde.

§9 Abs. 2 PromO

Die Arbeit hat bisher noch nicht zu Prüfungszwecken gedient.

Darmstadt, 25.Mai 2021 ______________________________

Acknowledgements

I hereby want to thank…

…Prof. Dr.-Ing. Dipl.-Kfm. Bastian J. M. Etzold for the opportunity to do my Ph.D. in his working group on such an interesting topic and his kind supervision.

…Dr. Gui-Rong Zhang for the kind supervision over the whole Ph.D. time.

…the whole AK Etzold for the kind atmosphere all over the time.

…my bachelor students, master students and interns for their reliable work.

…the mechanical workshop of the department of chemistry for their fast and reliable work.

…my friends and my family for their unconditionally support over the whole time.

…and the ERC grand council of the European Union for the financial support.

Deutsche Zusammenfassung/German abstract

Aufgrund der aktuellen Klimaproblematik [1, 2], stellt die Energiewende eine wichtige Richtung für unsere Zukunft dar. Ziel hierbei ist es, die direkte Nutzung von elektrischer Energie in allen Sektoren voranzutreiben [3]. Begleitet wird diese durch die Rohstoffwende. Kohlenstoffdioxid (CO_2), ist hierbei ein interessanter Rohstoff, der z.B. heute bereits in Kraftwerken, Müllverbrennungsanlagen und der Stahl- oder Zementproduktion in hohen Konzentrationen anfällt [4, 5, 6]. Hierbei spielt eine CO_2-Kreislaufwirtschaft eine wichtige Rolle. Als vielversprechen werden diesbezüglich Technologien zum Einfang und zur Konvertierung oder Lagerung von CO_2 angesehen [7]. Die elektrochemische CO_2 Reduktion (CO_2RR) setzt bei beiden Herausforderungen an, weswegen sie Bestandteil intensiver aktueller Forschung ist. Verschiedene Katalysatormaterialien zeigen unterschiedlich starke Selektivitäten zu unterschiedlichen Hauptprodukten. Entlang dieser Hauptprodukte kann eine Einteilung der CO_2RR Katalysatoren in verschiedene Gruppen erfolgen [8, 9]. Inmitten dieser Materialien nimmt Kupfer eine Sonderstellung ein. Es ist das einzig bekannte Material, welches in der Lage ist, CO_2 direkt in Kohlenwasserstoffe umzusetzen. Neben polykristallinem Kupfer [10, 11], Kupfereinkristallen [12] oder Kupfernanopartikeln [13], wurden auch dentritische Kupferstrukturen untersucht, beispielsweise Kupferschaummaterialien [14]. Die Struktur der Kupferschäume scheint zur Selektivitätssteuerung geeignet zu sein. Neue Möglichkeiten die Struktur der Kupferschäume in der Synthese unabhängig zu beeinflussen ist nötig. Die Möglichkeit der Modifikation mit Ionischen Flüssigkeiten (IL) könnte ebenfalls interessant sein und ist bisher nicht untersucht. Weiterhin hat sich jüngst gezeigt, dass die experimentellen Untersuchungen sehr herausfordernd sind. Oft werden nicht relevante hohe Stromdichten erreicht, experimentelle Parameter wie die Strömungsführung beeinflussen das Ergebnis und weiterhin sind geringste Mengen an Verunreinigungen zu vermeiden. Die neuesten Erkenntnisse sind in der Entwicklung eines neuen experimentellen Aufbaues umzusetzen, um Einflüsse der Katalysatorstruktur und IL Modifikation sinnvoll untersuchen zu können.

Ziel dieser Arbeit ist die Etablierung eines experimentellen Aufbaus und Messprotokolls zur reproduzierbaren Messung der CO_2 Reduktion an Kupferkatalysatoren, sowie Untersuchungen zur Modifikation der Struktur von Kupferschaumkatalysatoren und chemischen Modifikation mit ILs.

Zunächst sollen die Reaktortypen der H-Typ Zelle und des modularen Plattenreaktors hinsichtlich ihrer Eignung untersucht werden. Weiterhin muss das experimentelle Vorgehen entwickelt werden und die kritischen Parameter der CO_2RR evaluiert werden. Vor der Evaluierung der IL Modifikation wurden Materialeigenschaften der Kupferschäume hinsichtlich ihrer Kontrollierbarkeit durchgeführt. Hierzu wurde eine neue Synthesemethode mittels Anwendung erzwungener Konvektion entwickelt. Der Einfluss auf die katalytische Aktivität der Kupferschäume wurde angeschlossen.

Die Untersuchungen mit der H-Typ Zelle fokussierten sich auf die Untersuchung der Stromdichte. Mit dem Einsatz des Kupferschaumes konnten höhere Stromdichten erreicht werden. Mit einem geometrieoptimierten PMMA Elektrolyseur führten Experimente bei hohen Überspannungen immer wieder zu Abbrüchen des Experimentes aufgrund von zu hohen Spannungen an der Gegenelektrode. Erste Ergebnisse der IL Modifikation erwiesen sich hinsichtlich der Stromdichte als vielversprechend. Jedoch konnte mit der Zeit ein Stromabfall beobachtet werden, der auf eine potentielle Kontamination des Reaktormaterials zurückzuführen war. Die Reinigung des PMMA Materials erwies sich an dieser Stelle als schwierig.

Mit der Verwendung von PEEK konnte das Reinigungsproblem behoben werden. Faraday Effizienzen konnten in Richtung CO_2RR Produkte durch Vorbehandlung der Kupferträgerplatte und Optimierung des CO_2 Volumenstromes erreicht werden.

Die Synthese von Kupferschaummaterialien anhand des Literaturprotokolls führte zu einem Anstieg der abgeschiedenen Masse, des Oberflächenporendurchmessers, der Schaumdicke und des Rauhigkeitsfaktors mit steigender Coulomb-Zahl bei der Abscheidung. Dies besagt, dass die reproduzierte Syntheseroute mehr als eine Materialeigenschaft gleichzeitig verändert. Im Gegensatz hierzu konnten Mithilfe der Synthese unter Anwendung erzwungener Konvektion die Parameter abgeschiedene Masse, Schaumdicke und der Rauhigkeitsfaktor konstant gehalten werden. Einzig der Oberflächenporendurchmesser änderte sich mit Erhöhung der Rührerdrehzahl bei konstanter Coulomb-Zahl.

Für die Kupferschaumkatalysatoren zeigte sich, dass mit steigender Coulomb-Zahl die Stromdichte hin zu höheren Überspannung weniger stark anstieg. Zudem wurde die Wasserstoffentwicklung im Vergleich zu Gasphasenprodukte der CO_2RR bevorzugt. Das gleiche zeigte sich für die Flüssigphasenprodukte mit Ausnahme der von Ethylenglykol. Die neu entwickelte Synthesemethode zeigte hinsichtlich der katalytischen Eigenschaften der Materialen starke Unterschiede hinsichtlich der Stromdichten. Faraday Effizienzen (FE's) der Gasphasenprodukte wurden nicht beeinflusst. Vor allem die Bildung von Alkoholen in der Flüssigphase unterlag einem starken Einfluss.

Der Einfluss der IL Modifikation wurde mit den ionischen Flüssigkeiten [BMIm][NTf_2] und [BMMIm][NTf_2] untersucht.

Durch IL Modifizierung des Kupferschaumes konnte die Stromdichte nicht beeinflusst werden. Einzig eine leichte Steigerung der H_2 FE und eine Unterdrückung der Ethen-Bildung konnte festgestellt werden. In der Flüssigphase konnte die Bildung von Alkoholen komplett unterdrückt werden.

Content

Acknowledgements

Deutsche Zusammenfassung/German abstract

Content

Abbreviations

List of figures, schemes and tables

Abbreviations

List of Abbreviations

CO_2RR	electrochemical reduction of CO_2
IL	Ionic liquid
SCILL	supported catalyst with ionic liquid layer
iR	internal resistance
[BMIm][NTf_2]	1-butyl-3-methylimidazolium bis(trifluoromethylsulfonyl)imide
[BMMIm][NTf_2]	1-butyl-2,3-dimethylimidazolium bis(trifluoromethylsulfonyl)imide
PMMA	Polymethylmethacrylate
PEEK	Polyetheretherketone
FE	Faradaic efficiency
SEM	Scanning electron microscopy
EDS	Energy dispersive scattering
XPS	X-ray photoelectron spectroscopy
MtC	million metric tons carbon equivalents
HER	hydrogen evolution reaction
RHE	reversible hydrogen electrode
LSV	linear sweep voltammetry
ORR	oxygen reduction reaction
n-Bu	n-butyl
[BMIm][OTf]	1-butyl-3-methylimidazolium trifluoromethanesulfonate
PEIS	Potentiostatic electrochemical impedance spectroscopy
WE	working electrode
RE	reference electrode

CE	counter electrode
OER	oxygen evolution reaction
ECAS	electrochemical active surface
$DMVCl_2$	dimethyl viologen chloride
OCP	open circuit potential
R_f	roughness factor
CV	cyclovoltammetry
PFA	perfluoroalkoxy alkane
wt.-%	weight percent
OD	outer diameter
MFC	mass flow controller
SCV	stair case voltammetry
FID	flame ionization detector
TCD	thermal conductivity detector

List of symbols

x	mole fraction [mol/mol]
A	area [m^2]
I, i	current [A]
E	potential [V]
J	current density [A/m^2]
R	resistance [Ω]
d	diameter [m]
p	pressure [Pa]
n	moles [mol]
V	volume [m^3]

$\dot{n}$	mole flux [mol/s]
$\dot{V}$	volume flux [m^3/s]
c	concentration [mol/m^3]
z	electron transfer number
D	diffusion coefficient [m^2/s]
v	potential sweep rate [V/s]

List of indices

ads	adsorbed
solv	dissolved
geo	geometric
max	maximum
tot	total, overall
i	product species i

1. Introduction

The energy transition is one important approach to face the recent climate change problem [1, 2]. This includes providing the direct usage of electrical energy in all economic sectors [3]. The energy transition goes along with a raw materials change. Here, carbon dioxide (CO_2) is an interesting raw material, which is produced in higher concentrations in power plants, waste incineration plants and the steel or cement industry [4, 5, 6]. Important for the usage of carbon dioxide as raw material will we a circular economy. Promising technologies therefore are technologies for capturing and converting carbon dioxide or to store it [7].

One major research focus of the recent years for converting CO_2 is the electrochemical reduction of CO_2 (CO_2RR). Here, both aspects of raw materials change from fossil raw materials to CO_2 and to directly use electrical energy for chemical conversions are combined.

Different catalysts materials can be used for this reaction depending on the major product of interest. Along the synthesized products, the CO_2RR catalysts can be classified in different groups [8, 9]. Among these materials, copper is the unique one to be able to produce hydrocarbons directly out of carbon dioxide [10]. *Hori et al.* is known as a pioneer for the CO_2RR with copper catalysts and he was successful in studying fundamental knowledge about this reaction [11, 12]. Since it is important to increase the resulting current density and thus the productivity of copper catalysts, research was focused on copper catalysts with higher surface areas. Therefore, research focused on nano-particles [13] or dentritic copper materials, like copper foams [14]. These copper foam materials showed high selectivities for ethylene [15], which is one of the most interesting products in CO_2RR.

Further investigations on the selectivity of copper foam materials and how to influence the product formation is of a high interest. Besides the selectivity issue, also to achieve high current densities is important. Both issues will be investigated in this thesis.

2. State of the Art

2.1. Electrochemical reduction of CO_2 (CO_2RR)

2.1.1. Introduction and overview

The electrochemical pathway to convert CO_2 to chemicals and fuels is one of the big research topics. One effort is to include the electrochemical CO_2 reduction in a potential carbon circle, as shown in scheme 1 [10]. This circle, includes the use of renewable energies, as electrical energy, to convert CO_2 into fuels or chemicals. The carbon sources are, for example, CO_2 emissions.

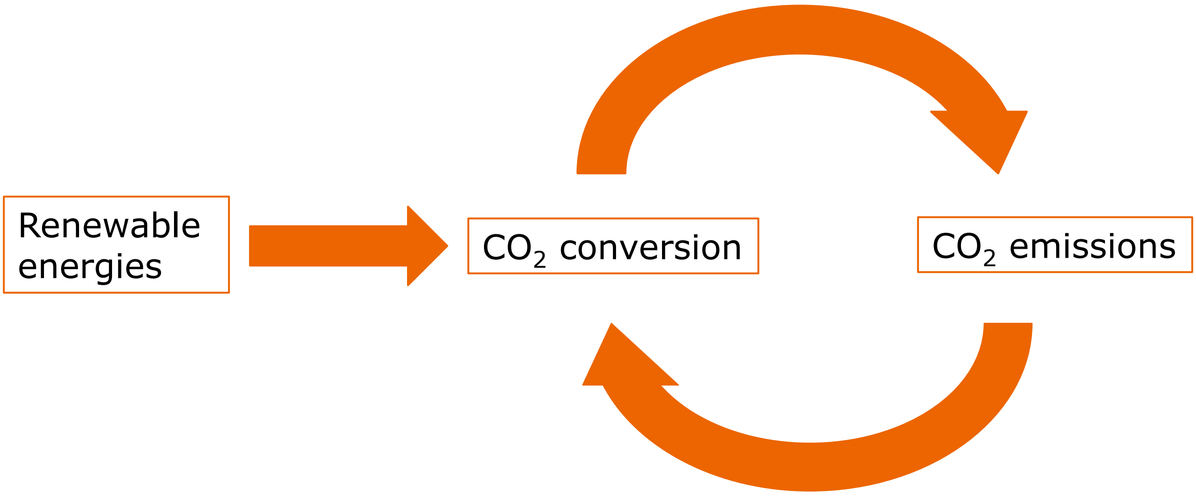

Scheme 1: CO_2 conversion and emission cycle with the help of renewable energies.

The CO_2RR is intensively studied in many fields of catalysis. In homogeneously catalyzed CO_2RR, the catalyst is a metal complex in the electrolyte solution. CO_2 as substrate is complexated by the metal complex and the electron transfer from the cathode to the metal complex enables the catalytic conversion of CO_2 [16]. Herein, active metals are for example copper, palladium, nickel or cobalt [17]. Typical ligands are containing nitrogen, like pyridine or porphyrins. By exchanging the metal complex with an enzyme, a biocatalytic CO_2RR is developed. Further details on homogeneous or biocatalytic CO_2RR can be obtained in several review articles [17, 18, 19]. In contrast to the previous ones, the heterogeneously catalyzed CO_2RR uses a working electrode, which serves as electron support as well as catalyst (scheme 2). Here, the substrate needs to be adsorbed on the electrode surface before reacting to the final product.

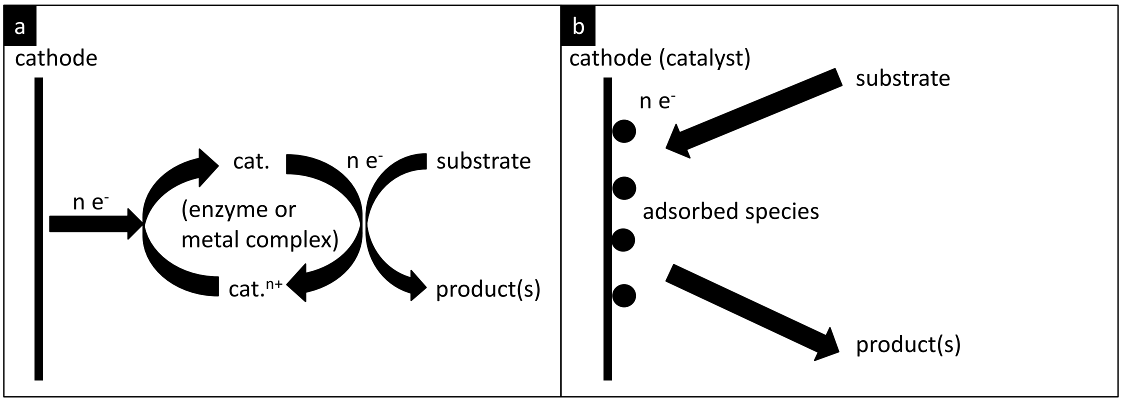

Scheme 2: Difference between homogeneous/bioelectrocatalysis (a) and heterogeneous electrocatalysis (b).

Hori could show, that different metals can be classified by the main products obtained by their use [8, 9]. Roughly four groups can be distinguished (scheme 3). The first group contains the metals Ni, Fe, Pt, Ti, Ga. Their activity towards CO_2RR is so low that water splitting will be the predominating reaction with H_2 as major product. The second group around Pb, Hg, In, Sn, Cd, Tl is known for formate as major product. One big advantage of these metals is their known high overpotential for hydrogen evolution reaction (HER). In terms of a technical process, this high overpotential towards an undesired coproduct is of advantage. One technical example therefore is the amalgam-process for chlorine production [20]. Metals as Au, Ag, Zn are mainly catalyzing the reaction of CO_2 to CO.

Unique among all the metals in the periodic system of elements is copper. Copper is the only metal known to build up hydrocarbons with significant faradaic efficiencies (FE). Since the focus of this work will be on copper catalysts, the following sections will focus on literature results with different copper materials.

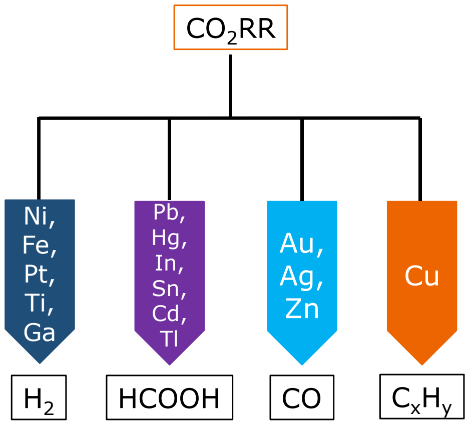

Scheme 3: Groups of metals and their main products during CO_2 electrolysis.

2.1.2. Copper catalysts in CO_2RR

Different morphologies of copper were studied towards their behavior in CO_2RR. First results were obtained by *Hori et al.* in the 1980's with poly crystalline copper [11]. Different electrolytes and electrolyte concentrations were screened by chronopotentiometric measurements regarding their impact on product faradaic efficiencies (FE's) in an H-type glass cell. For the typical CO_2RR electrolyte 0.1 M potassium bicarbonate, ethylene FE of 30 % could be reached at a constant current density of 5 mAcm^{-2}. Switching to 0.1 M potassium chloride as electrolyte increased the FE of ethylene from 30 % to 48 % and decreased the methane FE from 29 % for potassium bicarbonate to 14 % for potassium chloride. Products found by *Hori et al.* were methane, ethylene, ethanol, propanol, carbon monoxide, formate and hydrogen as coproduct of the water splitting reaction. In 2012, the group of Jaramillo was able to find even more products in the liquid phase [10]. Beside the products found by *Hori et al.*, further C_2 and C_3 oxygenates were found and reported for the first time. From the mechanistic point of view, *Kuhl et al.* suggest enol-like surface intermediates for the reaction pathways towards C_2 and C_3 products, depicted in scheme 4 [10].

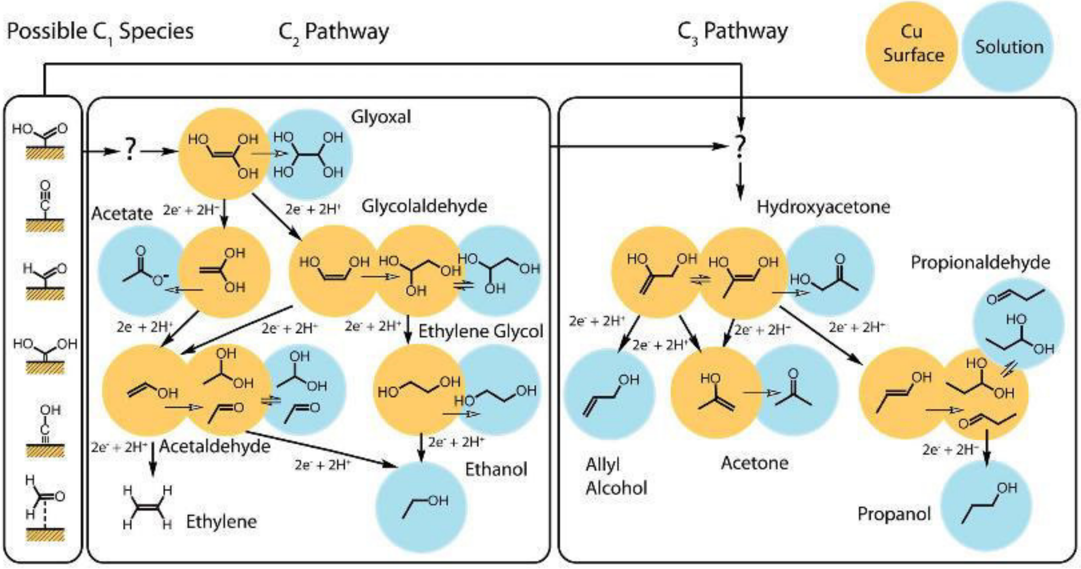

Scheme 4: Mechanism for CO2RR products formation, suggested by *Kuhl et al.* [10]. Reproduced from K. P. Kuhl, E. R. Cave, D. N. Abram and T. F. Jaramillo, *Energy Environ. Sci.*, 2012, **5**, 7050 (***https://doi.org/10.1039/C2EE21234J***) with permission from the Royal Society of Chemistry.

Beside studying polycrystalline copper, *Hori et al.* also did investigations with copper single crystals [12], as some other groups also did [21, 22]. Furthermore, he intensified his research in terms of the facet dependence on the product formation. The main conclusion out of these investigations are that Cu(111) facets drive the reaction pathway to C_1 products while Cu(100) or higher facets are mainly catalyzing the formation of C_2 and C_3 products. These results have been verified by theoretical calculations of binding energies of different species on different Cu facets [23, 24, 25, 26]. Within these calculations, also different pathways for high overpotentials (< -0.8 V vs. reversible hydrogen electrode, RHE) and low overpotentials were found [24].

Since the current density correlates with the reaction kinetics and therefore the productivity of an electrochemical process, it is an important parameter for an electrochemical process. In order to increase the current density of copper catalysts, copper nanoparticles were used. *Reske et al.* intensively studied the impact of copper nanoparticle sizes on current densities as well as on faradaic efficiencies [13]. Below a particle size of 5 nm, current density raised by a factor of two from about -23 mA/cm^2_{Cu} with particle sizes of 5 nm to about -48 mA/cm^2_{Cu} with particle sizes of 2.5 nm at -1.1 V vs. RHE. Above 5 nm particle size, current density stayed at about -22 to -23 mA/cm^2_{Cu} and is comparable to electro polished copper foil current density. This shows that the electrochemical active surface area plays an important role in reaching high current densities. But the faradaic efficiencies show, that below 15 nm, the FE's are nearly constant for all detected gas phase products. The trend for hydrocarbons (CH_4, C_2H_4) shows a decrease in FE with decreasing particle size and is the highest for the electro polished copper foil. The decrease is more pronounced for methane (55 % FE to 15 % FE) than for ethylene (20 % FE to 5 % FE). In contrast, FE of carbon monoxide and hydrogen were increasing with decreasing particle size. Hydrogen increased by a factor of three from 20 % FE to 65 % FE and carbon monoxide by a factor of 5 from below 5 % FE to 25 % FE.

Based on these results, *Mistry et al.* investigated the influence of the interparticle distance [27]. For a particle size of 4.7 nm, three different interparticle distances of 53 nm, 31 nm and 24 nm were established. The current density could be increased by a factor of two from about -10 mA/cm^2_{Cu} for 53 nm to -20 mA/cm^2_{Cu} for 31 nm at -1.1 V vs. RHE, investigated by linear sweep voltammetry (LSV). A further increase by a factor of 2.5 could be achieved when decreasing the interparticle distance from 31 nm to 24 nm. A closer look to the obtained FE's shows that there is a dependence of FE from copper particle size as well as interparticle distance. For copper particle sizes of 4.7 nm for example, hydrocarbons showed an increase in FE with decreasing interparticle distance. Methane increased from 20 % to 40 % FE when decreasing the interparticle size from 58 to below 25 nm. This trend is less pronounced for ethylene, where in the same interparticle distance range the FE increased from 0 to 10 % FE. By decreasing the interparticle distance, hydrogen evolution could be suppressed (from 65 % to 50 % FE).

Many other papers dealing with copper nanoparticles as CO_2RR catalysts were published with different preparation methods [28, 29, 30, 31] or different supports [32, 33]. They all have in common, that the relation between copper catalyst structure, activity and faradaic efficiencies was found.

Therefore, other working groups were testing different copper catalyst structures to investigate their behavior in CO_2RR. *Smith et al.* intensively worked with copper nanowire catalysts [34, 35]. The group of Guido Mul developed a porous hollow fiber electrode made of copper [36]. This electrode is able to convert CO_2 to CO with 70 % FE at -0.4 V vs. RHE. Another approach is growing porous copper surfaces on flat supports. *Sargent et al.* synthesized different copper structures by a simultaneous dissolution and redeposition process of copper [37]. Depending on the applied potential, structures from copper nanoclusters at -0.7 V vs. RHE to dendrites at -1.4 V vs. RHE are possible.

Porous copper surfaces can also be synthesized by chemical dealloying [38]. In a first step, an electro polished copper plate is covered with zinc by electrodeposition. Thermal treatment leads to Cu-Zn alloys at the surface. Chemical dealloying solves the zinc out of the alloys and a porous copper surface results. The catalysts are able to produce ethylene with FE up to 40 % while suppressing the formation of methane compared to copper foil catalysts. Another method for porous copper surface synthesis is the additive-controlled electrodeposition with 3.5-diamino-1.2.4-triazole (DAT) [39]. Figure 1 shows the influence of the adapted pH value on the surface morphology obtained by electrodeposition. As a result, the higher the pH value, the thicker the copper threads. When current density was increased from -4 mA/cm² to -8 mA/cm², the threads are growing thicker. An exception here was the case for pH 1. At -4 mA/cm², copper threads were growing while at -8 mA/cm² spherical particles were existent.

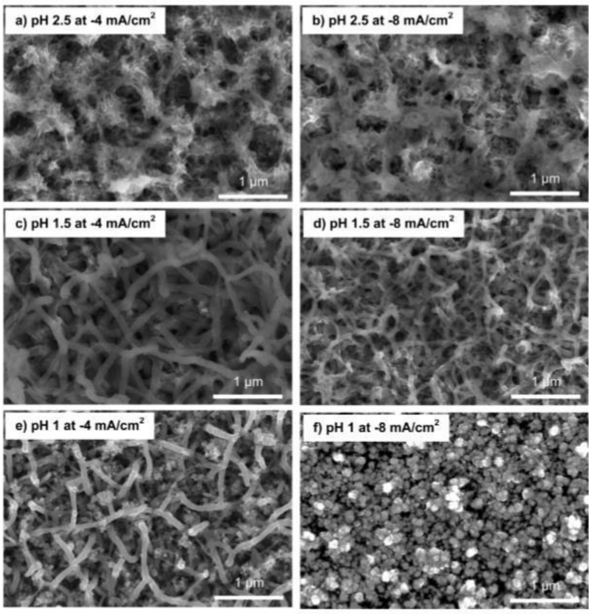

Figure 1: Morphology of copper structures synthesized by additive-controlled electrodeposition at different pH values and different applied current densities [39]. Reprinted (adapted) with permission from (*ACS Catal.* 2017, 7, 5, 3313–3321, Publication Date: March 22, 2017, DOI: 10.1021/acscatal.6b03613.). Copyright (2017) American Chemical Society.

In 2004, *Shin et al.* were the first to publish copper with a well-defined dentritic porous structure [40]. It could be shown, that under harsh conditions, hierarchical pore structures could be obtained when using an acidic copper sulfate solution as electrolyte. A closer insight into these structures reveals a dentritic copper structure. Acidic additives like acetic acid or hydrochloric acid influenced the copper foam structures. When adding acetic acid to the electrolyte, surface pore sizes were reduced at the same deposition time. When adding hydrochloric acid, the dentritic structure got more and more lost with increasing concentration of hydrochloric acid. In 2014, the group of Palmore was the first that used copper foam catalysts in CO_2RR [14]. Under typical CO_2RR conditions of 0.1 M $KHCO_3$ (pH 6.8) electrolyte, room temperature and atmospheric pressure, FE of reduction products were determined in an H-type glass cell. At -1.5 V vs. Ag/AgCl, nearly 40 % FE of formate were reached as main product out of CO_2RR. Ethylene FE droped to below 1.5 % compared to typical values of over 20 % for copper foil. But it was the first time that ethane was reported although only with 1.2 % FE. Investigations with copper foam catalysts synthesized at different deposition times showed an increasing FE for formate with increasing deposition time at -1.7 V vs. Ag/AgCl. Furthermore, with increasing deposition time, hydrogen FE is reduced. On top, increasing the electrolyte concentration increased the overall current density. The last point stated was seen for copper foil electrodes as well as for copper foam catalysts independent from the deposition time. But the increase in overall current density is more pronounced for copper foam catalysts than for copper foil catalysts and even more pronounced for longer deposition times. *Dutta et al.* improved the CO_2RR with copper foam catalysts by using an ultra-pure copper substrate as support and switching to 0.5 M sodium carbonate [15]. He agrees with the mechanistic hypothesis of a hydrogen assisted electrodeposition of copper. This mechanistic point of view is supported by growing pore sizes obtained with growing deposition time, depicted in figure 2. This underlines the imagination of the hierarchical pore structure development.

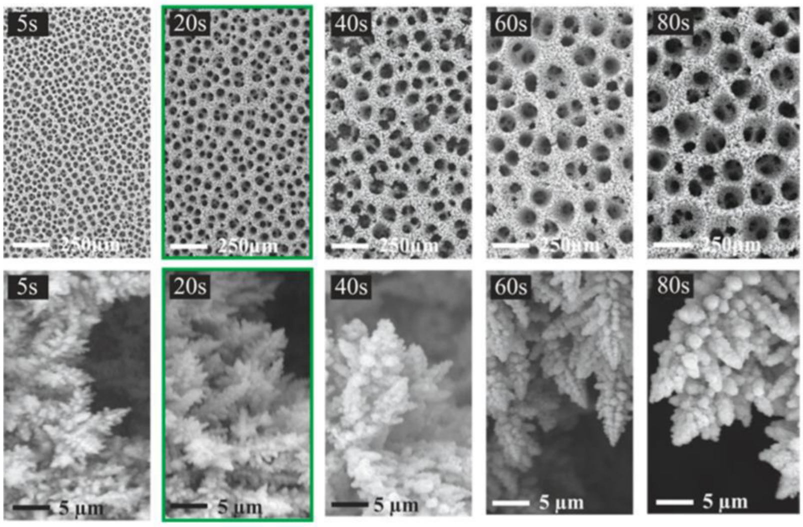

Figure 2: Copper foam catalyst morphology recorded by SEM at different deposition times [15]. Reprinted (adapted) with permission from (*ACS Catal.* 2016, 6, 6, 3804–3814, Publication Date: May 5, 2016, DOI: 10.1021/acscatal.6b00770.). Copyright (2016) American Chemical Society.

Broekmann's group was able to increase the faradaic efficiencies for gas phase products with copper foam catalysts. The main difference to copper wafer catalysts was the shift in selectivity totally to C_2 products in the gas phase. Formate FE is similar over the whole investigated potential range for copper wafer and copper foam catalysts. An interesting result was gained concerning C_2 products. Ethylene FE could be increased at -0.7 V vs. RHE from 10 % with the copper wafer to about 38 % for the copper foam catalyst. Ethane FE reached with both cases about 20 % FE at -0.8 V vs. RHE, but the FE at potentials higher than -0.8 V vs. RHE is also about 20 % FE. This is not the case for the copper wafer as catalyst, where at potentials higher than -0.8 V vs. RHE, the FE for ethane drops. This deposition method was also successfully established for copper mesh or copper sponge as substrate [41, 42]. This provides further surface area for CO_2RR.

2.1.3. Mechanism of CO_2RR at copper catalysts

The formation of CO_2RR products is quite complex on the mechanistic level. Important for the formation of hydrocarbons is the competition between CO_2RR and the hydrogen evolution reaction. *Zhang et al.* investigated this competition for the Cu(111) facet by DFT calculations [43]. Both consecutive reactions need an adsorption step at the surface as first step. In case of CO_2RR, it is the adsorption of CO on the surface while for the HER, it is the adsorption of protons either according to the Volmer-Heyrovsky or the Volmer-Tafel mechanism. Different surface coverage degrees of CO and H_2 were applied and the influence on the binding energy was studied. At coverages 3/9 of a monolayer, the binding energy of CO is increasing with a high linear slope of about 0.3 eV for each further surface coverage of 1/9 of a monolayer. This means, that the binding of CO is more and more decreasing. For hydrogen, the effect is less dramatic. *Zhang et al.* concluded, that CO coverage is at least 3/9 of a monolayer and thus, CO hydrogenation is the limiting step for CO_2 reduction to hydrocarbons. Another important step for the formation of C_2 products is the dimerization of adsorbed CO, as discussed in [44, 45]. *Montoya et al.* [44] compared the CO coupling activity on Cu(111) and Cu(100). The transition state energy for the formation of CO dimers is around 0.35 eV lower for the Cu(100) facet. This is in agreement with the experimental results described in the previous section. *Goodpaster et al.* improved this calculation with an improved Fixed Electrode Potential Self-Consistent Field Procedure, based on the Poisson-Boltzmann equation [45]. The formation of CO dimer and the hydrogenation of this dimer are depicted in their paper. It is shown, that applying higher overpotentials starting from -0.0 V vs. RHE to -1.0 V vs. RHE is increasing the free energy barrier of the transition state from 0.6 eV to 0.7 eV. But the energy of the resulting CO dimer is decreased by applying higher overpotentials. The hydrogenation of the CO dimer shows the opposite trend. Applying higher overpotentials from -0.0 V vs. RHE to -1.0 V vs. RHE increased the free energy barrier of the transition state from slightly below 0.5 eV to around 0.65 eV. Here, the lower the overpotential, the more stable the final configuration.

Beside the CO dimerization pathway, also the hydrogenation of CO is viable as intermediate for C-C-coupling. On Cu(100), there are two possibilities to form the resulting adsorbed CHO intermediate. The first one is the Tafel process, where adsorbed CO and adsorbed H are reacting to adsorbed CHO

$$CO_{ads} + H_{ads} \rightarrow CHO_{ads}. \tag{I}$$

Compared to the CO dimerization pathway, the transition state energy of the Tafel process is higher in free energy. The difference is around 0.25 eV at -0.0 V vs. RHE and around 0.1 eV at -1.0 V. vs. RHE. This indicates, that especially at lower overpotentials, the CO dimerization pathway is favored. The same can be seen for the final configuration. At -0.0 V vs. RHE, the *CHO intermediate is around 0.65 eV higher in free energy than the CHOCO intermediate, while the difference is 0.35 eV at -1.0 V vs. RHE [45].

The second possibility is the Heyrovsky reaction, where adsorbed CO is directly reacting with water by reducing the latter one

$$CO_{ads} + H_2O_{aq} + e^- \rightarrow CHO_{ads} + OH^-_{aq}. \tag{II}$$

Here, the transition state energy is very high at -0.0 V vs. RHE with around 1.4 eV. At this potential, also the final configuration is nearly at the same energy level as the transition state [45]. At -1.0 V vs. RHE, the transition state free energy is as high as around 0.6 eV and therefore around 0.05 eV lower than for the CO dimerization pathway. For the final configuration, the free energy of 0.5 eV is around 0.35 eV higher than for the CO dimerization.

This indicates, that at low overpotentials, the CO dimerization seems to be the predominant pathway, while at higher overpotentials, especially the Heyrovsky mechanism is a competing pathway towards C-C coupling products.

A further intermediate for C-C coupling described in literature is the COH species [23, 46]. Here, the COH intermediate has different possibilities to be converted to C_2 products as depicted in scheme 5. By direct dihydroxylation, C-Cu species are formed. This species can be hydrated by protons to form a CH-Cu intermediate. This intermediate can be also built up by (OH)CH-Cu intermediate, previously formed by hydration of the COH species. The CH-Cu intermediate is further hydrated to CH_2-Cu. Alternatively, the formation can be made by dehydroxylation of a chemisorbed methanol species (CH_2OH), resulting from the hydration of the (OH)CH-Cu intermediate.

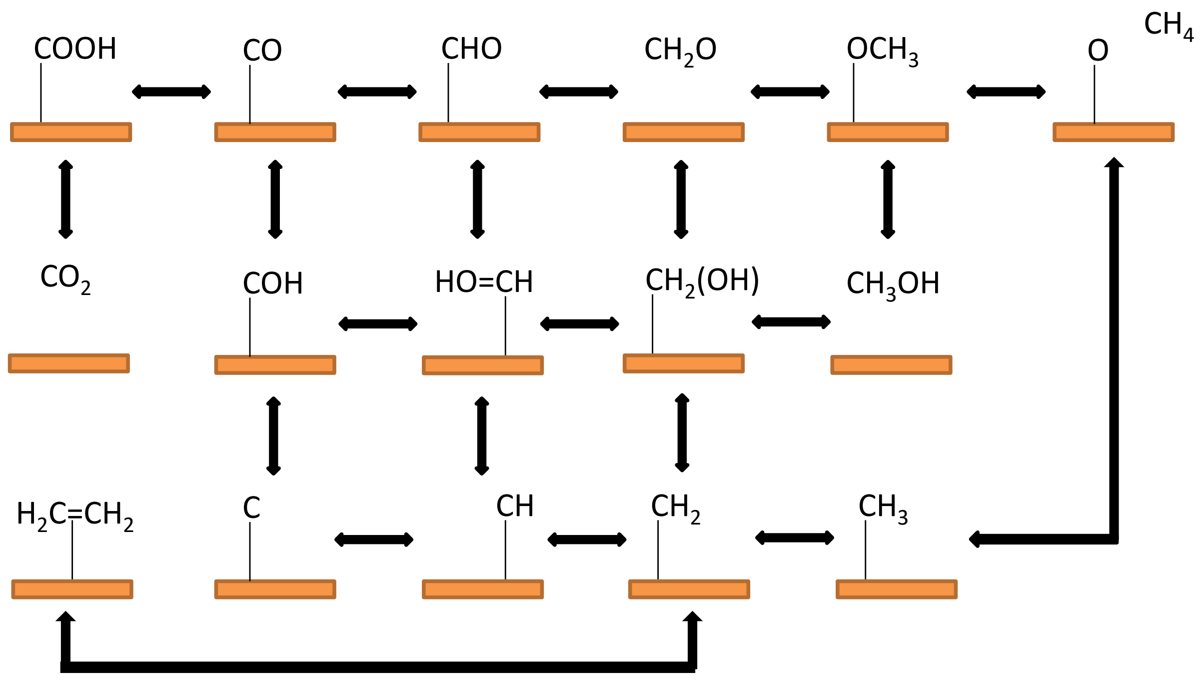

Scheme 5: Reaction pathways towards methane, methanol and ethylene on Cu(111).

The formation of higher alcohols as ethanol or n-propanol is depicted in scheme 6 [47]. For ethanol, two pathways are possible. The first one goes via CO dimerization. After several hydrogenation steps, a CH_3CH_2O-Cu intermediate is formed. This intermediate can be electrochemically hydrogenated to form ethanol. The second route goes via the methylene route. Instead of methylene dimerization to ethylene as described before, surface bound methylene can react with CO. This insertion of CO into the CH-bond is followed by hydrogenation steps which lead to the same intermediate as described in the first pathway (CH_3CH_2O-Cu). The n-propanol pathway goes via the reduction of adsorbed CO to adsorbed C. After hydrogenation of C to methylene, CO insertion and hydrogenation to CH_3CH-Cu is followed. Here, further CO insertion and hydrogenation leads to a CH_3CH_2CHO-Cu intermediate. N-propanol is resulting by hydrogenation of the intermediate.

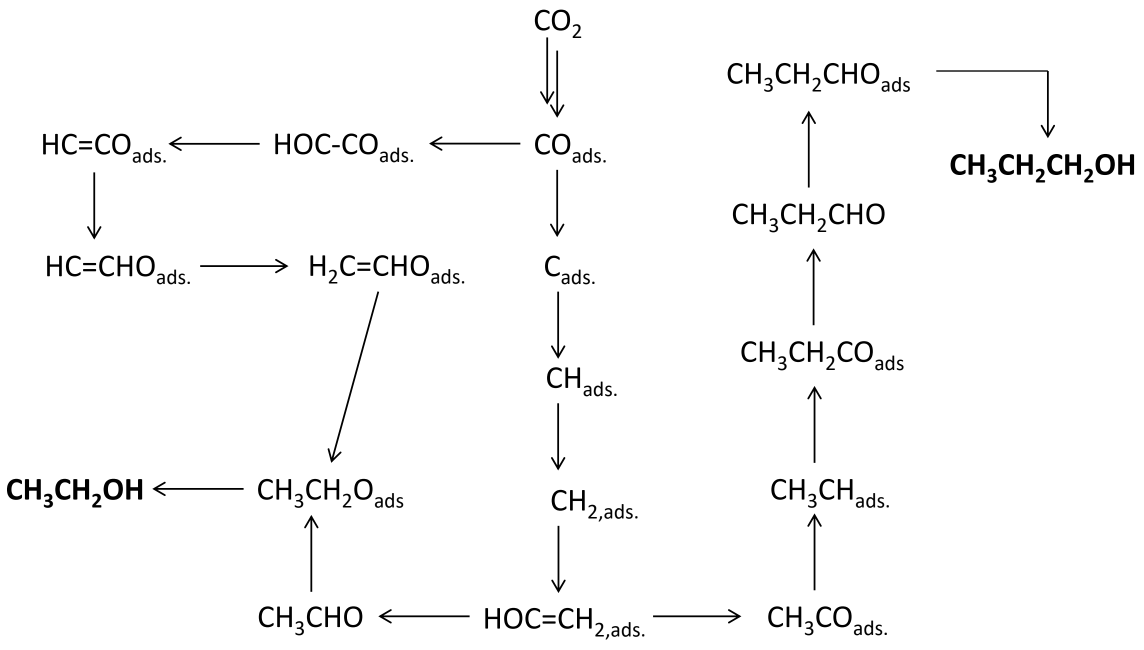

Scheme 6: Reaction pathways towards ethanol and n-propanol.

Therefore, in literature, two major pathways were postulated [48]. The ethanol pathway and the ethylene pathway. While the ethanol pathway mainly results in C_2 alcohols and aldehydes, the ethylene pathway results in ethylene and carbonic acids. It is stated here, that the pathways are potential dependent. Furthermore, the formation of hydrocarbons is also pH dependent [49].

2.2. SCILL concept and ionic liquids in CO_2RR

2.2.1. Reasons for ionic liquids in CO_2RR

Beside the ideas presented in the prior section, ionic liquids (IL) as electrolyte have been studied in CO_2RR. The motivation for ionic liquids in CO_2RR consists of three major parts (figure 3). First of all, more CO_2 can be dissolved in ionic liquids than in water. This can be easily seen, if the Henry's constants of CO_2 in ionic liquids [50] and CO_2 in water are compared [51]. The imidazole based ionic liquid [BMIm][NTf$_2$] for example, has a Henry's constant of 33.0 bar, while for water, the Henry's constant is 1627.7 bar with the definition of the Henry's constant

$$H = \frac{p_{CO_2}}{x_{solv}} \qquad \text{(III)}$$

where pCO_2 is the partial pressure of CO_2 in the gas phase and x_{solv} is the mole fraction of CO_2 in the liquid phase.

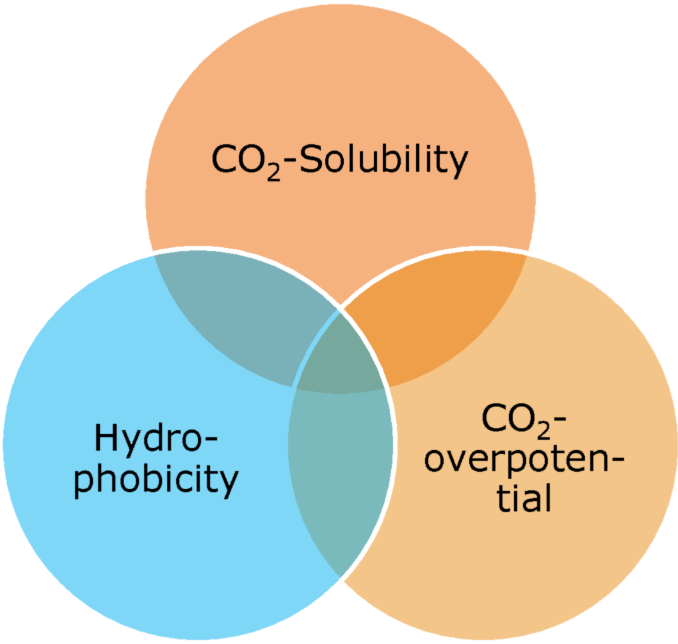

Figure 3: Motivation for using ionic liquids in CO_2RR.

The improved solubility of CO_2 in [BMIm][NTf$_2$] is explained by the formation of an IL-CO_2-adduct. This formation is drawn in scheme 7, according to the theoretical calculations of *Wang et al.* [52].

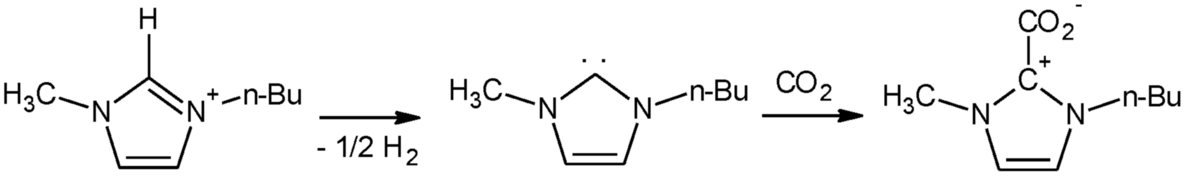

Scheme 7: Formation of IL-CO_2 adduct with [BMIm][NTf$_2$].

In case of imidazole based ionic liquids, the first step is supposed to be the deprotonation of the imidazole to a carbene species. This highly reactive species is now able to bind CO_2 and form the IL-CO_2 adduct. In this adduct. CO_2 has a formally negative charge. The formation of the intermediate “CO_2^-“ without use of ionic liquid has an overpotential of -1.9 V vs. NHE [52]. With the use of ionic liquid, this energy barrier can be overcome by an alternative pathway with a lower energy barrier [53]. This means that ionic liquids are directly participating as cocatalyst in the catalytic cycle. The energy profiles of CO_2 reduction to CO with and without ionic liquids are given in scheme 8. The previous explanation shows the second advantage of using ionic liquids in CO_2RR. Ionic liquids are able to lower the CO_2RR overpotential.

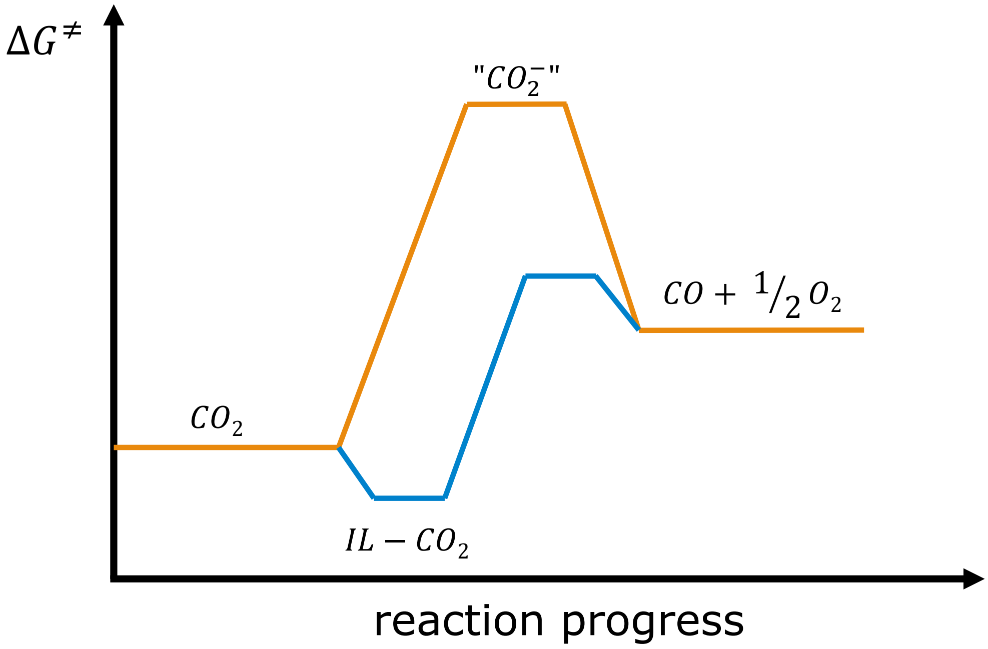

Scheme 8: Energy profiles for CO_2 reduction to CO with and without use of ionic liquids. $\Delta G^{\neq}$: free activation energy.

The third point of motivation is the hydrophobicity of ionic liquids. Especially for the SCILL concept, this will be of importance. Since ionic liquids are more hydrophobic than aqueous electrolytes, the HER is supposed to be suppressed.

2.2.2. SCILL

SCILL is the acronym for supported catalyst with ionic liquid layer. It describes solid heterogeneous catalysts, whose active centers are coated with a film of ionic liquid [54] (see figure 4).

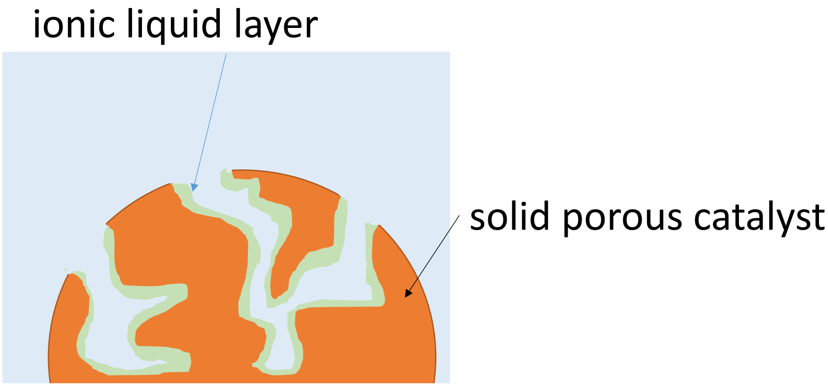

Figure 4: Illustration of the SCILL concept.

In 2007, *Kernchen et al.* introduced the SCILL concept for the thermally catalyzed hydrogenation of cyclooctadiene [55, 56]. With the IL modification, activity and selectivity of solid catalysts are influenced. The major two effects are described in the paper of Steinrück and Wasserscheid [57]. The first effect is the change of the effective concentration of chemical species at the catalytic active site. Here, the solubility of the chemical species in the IL and the related mass transfer processes are important. On the other hand, the IL can interact with the catalytic sites as promotor. This can change the adsorption behavior of chemical species and thus suppress unwanted side reactions. In terms of electrochemistry, *Erlebacher et al.* successfully applied the SCILL concept to the oxygen reduction reaction (ORR) [58]. Later, *Zhang et al.* were successful in increasing the mass activity by a factor of three by modifying the Pt catalyst with ionic liquid [59]. Also for Fe-N-C catalysts, ORR activity in alkaline media could be boosted [60].

2.2.3. Ionic liquids in CO_2RR

Due to the advantages of ionic liquids described in chapter 2.2.1, many groups studied the impact of ionic liquids in CO_2RR. A review of ionic liquids in CO_2RR is given by *Feng et al.* [61]. Typically used cations and anions of IL's are drawn in figure 5.

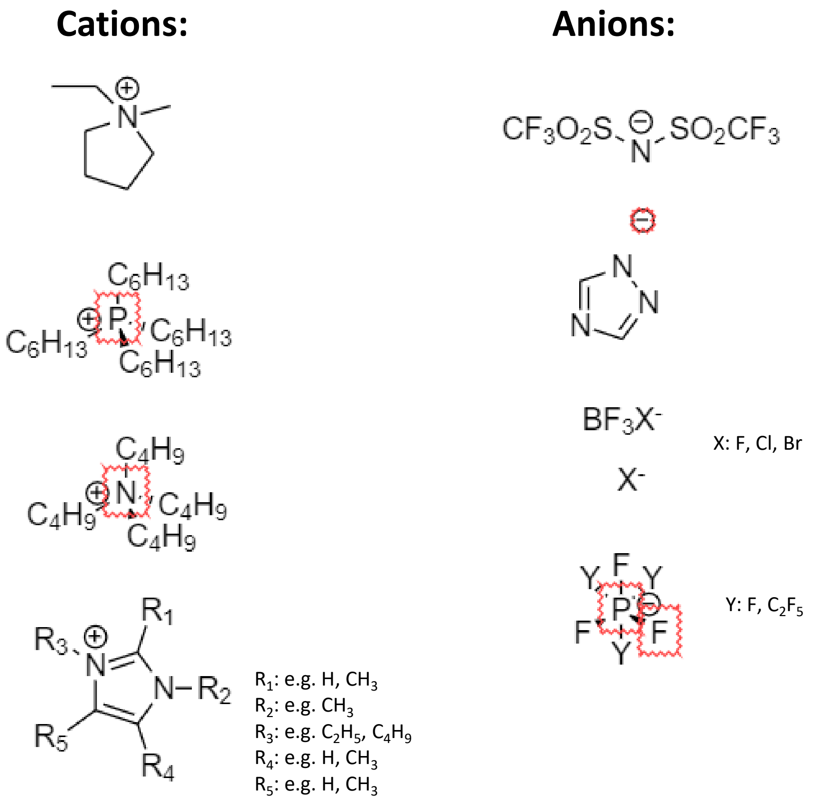

Figure 5: Typical cations and anions used for CO_2RR.

Rosen et al. have been the first in 2011 to lower the overpotential of CO formation by using a silver rod immersed in an aqueous solution of 1-ethyl-3-methylimidazolium tetrafluoroborate ([EMIm][BF_4]) [53]. They were successful in lowering the overpotential by 600 mV by reaching a faradaic efficiency of 96 %. *Martindale et al.* further investigated by cyclovoltammetry experiments, that the anion plays an important role in CO_2RR. They found, that the BF_4^- - anion leads to the lowest onset potential. This is explained by the lewis acid - lewis base adduct BF_4-CO_2^- [62]. *Tanner et al.* further investigated the effect of anion and cation in CO_2RR [63]. They found, that the highest current densities could be achieved with [BMIm][NTf_2] on a silver electrode, compared to other cations like [BMpyrr][NTf_2], [EMIm][NTf_2] or [PMIm][NTf_2]. The results with different cations used suggest, that the reductive mechanism possibly includes a chemical step (scheme 8).

$$M(ads) + CO_2 \longrightarrow M - CO_2(ads)$$

$$M - CO_2(ads) + e^- \xrightarrow[\text{rds}]{\text{slow}} M - CO_2^-(ads)$$

Scheme 8: Proposed mechanism with preceding chemical adsorption step of CO_2.

The importance of the anion could also be shown by cyclovoltammetry measurements. Here, $[BMIm]^+$ was used as cation and the anion was varied between $[NTf_2]^-$, $[BF4]^-$ and $[FAP]^-$. The current density drops in the row given before. This supports the hypothesis of the CE-type mechanism instead of the previously given E_{irr}C-type process. The advantage of imidazolium based ionic liquids compared to quarternary ammonium salts is shown by *Yang et al.* [64]. By replacing [Bu_4N][CF_3SO_3] against [BMIm][CF_3SO_3] as part of the electrolyte, the overpotential for the CO formation could be lowered by around 240 mV at a gold electrode. A highly efficient catalyst for CO_2RR to CO is bismuth. At -1.95 V vs. SCE, DiMeglio and Rosenthal were successful in reaching 95 % FE of CO with a partial current density of -5.51 mA/cm^2 for CO at a Bi-CMEC electrode by using [BMIm][BF_4] in acetonitrile [65]. By using different preparation methods, the partial current density could be raised to -31 mA/cm^2 [66]. These investigations were further deepened by measurements of the structural dynamics of the bismuth electrodes during CO_2RR in different imidazolium based ionic liquids [67]. By using MoS_2 as electrocatalyst in [EMIm][BF_4]/water mixture, the overpotential for CO could be lowered to 54 mV [68]. Other materials than silver or gold were also able to produce hydrocarbons in the presence of ionic liquids. Oh and Yu were able to get a FE of formate of around 60 % without detecting any hydrogen with MoO_2/Pb in a 0.3 M

[BMIm][PF$_6$] electrolyte [69]. *Han et al.* were successful in reaching a current density of -37 mA/cm^2 and a faradaic efficiency of over 91 % for formic acid [70]. Here, the electrocatalyst was Sn in a ternary mixture of [BMIm][PF$_6$], acetonitrile and water. Using [EMIm][N(CN)$_2$] as ionic liquid, nearly 82 % FE for formic acid could be reached using Sn as working electrode [71]. With the use of the superbase IL [P$_{66614}$][124Triz], *Hollingsworth et al.* were able to reduce the potential for formate production to -0.7 V vs. A/AgCl [72]. Although the achieved current density is quite low (-1 mA/cm^2), the overpotential for formate is as low as 170 mV. As mentioned before, bismuth is a good catalyst with a low overpotential towards CO in combination with [BMIm]$^+$ cation as part of the supporting electrolyte. By switching to the [DBU-H]$^+$ cation, the product formation can be switched from CO to formate [73]. Faradaic efficiencies of about 80 % and partial current densities between -25 to -40 mA/cm^2 could be achieved for formate. Since copper is an interesting material regarding CO$_2$RR products, it was also tested with ionic liquids. Copper as electrocatalyst is known in combination with the ionic liquid [BMIm][BF$_4$] for the synthesis of dimethyl carbonate (DMC) [74, 75]. But there are also a few examples with copper in CO$_2$RR. One is the use of [BMIm][OTf] for a Cu-Zn alloy electrocatalyst [76]. In this combination, syngas could be produced efficiently at 30 bar and 45 °C. Carbon monoxide with a faradaic efficiency of more than 98 % was achieved by the group of *Zhou et al.* [77]. They used an Ag-modified Cu electrode in [EMIm][BF$_4$] and [BMIm][NO$_3$] with CoCl$_2$ as additive. The reaction was stable over 150 h. Beside syngas, formic acid could be gained by using a copper electrode immersed in supercritical carbon dioxide [78]. The ionic liquid used in these studies was [BMIm][PF$_6$]. First attempts to immobilize ionic liquids on the electrode surface were done by *Ponnurangam et al.* [79] and *Han et al.* [80]. Both were modifiying copper plates with ionic liquids. *Ponnurangam et al.* coated the copper electrode with poly(4-vinyl pyridine) to reach 40 % FE for formate at an overpotential of -0.67 V. The catalytic activity was stable over 30 h of operation. Improved ethylene production (> 40 % FE) and ethanol formation (> 30 %) could be achieved by modifying a copper electrode with an electrochemically deposited film of N-substituted pyridinium additives [80]. This shows the potential of copper in CO$_2$RR with the use of ionic liquids. Since this work will be based on copper foam catalysts, also a literature survey for copper foam catalysts in combination with ionic liquids was done. The only publication in this field was given by *Huan et al.* [81]. As electrolyte, different mixtures of [EMIm][BF$_4$] in water were used. With increasing content of ionic liquid, hydrogen evolution could be suppressed by boosting formate production. The highest faradaic efficiencies obtained were over 83 % formate. Different deposition times of the copper foam catalysts did not influence the faradaic efficiencies of the products formate, hydrogen and carbon monoxide at all. To the best of our knowledge, the SCILL concept was not applied to CO$_2$RR before.

2.2.4. Mechanistic influence of ionic liquids in CO_2RR

As seen in the previous chapter, ionic liquids are able to directly influence the mechanism of CO_2RR. This can be seen by changed selectivities compared to the unmodified electrocatalysts or boosted activities. In literature, the IL interaction is discussed at two points. At one hand, ionic liquids are directly influencing the electrical double layer region and on the other hand, ionic liquids are chemically interacting with the electrode surface and intermediate species [61]. *Rosen et al.* [82] used sum frequency spectroscopy (SFG) to gain more detailed information about the dynamics at the electrode surface. Characteristic peaks for ring stretching (1570 cm^{-1}) and CH_3 bending (1430 cm^{-1}) depicted the coverage of the platinum surface with a monolayer of [EMIm]$^+$ cations. With higher overpotentials in the LSV, a peak at 2348 cm^{-1} becomes more and more dominant. This indicates the formation of a [EMIm]-CO_2-[BF4] complex at the electrode surface. Since the CO_2 peak is slightly redshifted compared to gas phase CO_2, the authors are indicating CO_2 to be bound to the [EMIm]$^+$ cation. Non-resonant (NR) SFG spectroscopy was done by *Rey et al.* [83] with the system silver and [EMIm][BF_4]. Independently from Ar or CO_2 purged electrolyte, the minimum NR intensity was observed at nearly the same potential. This indicates, that the intirinsic properties of the ionic liquid play a major role. The influence of ionic liquids to the electrical double layer properties was further proven by EIS measurements [84, 85]. For the investigation of the chemical interaction, many theoretical studies were performed on CO_2RR. For example, thermodynamic calculations of N-heterocycles as cocatalysts show the enhancement of CO_2 reduction [86]. *Wang et al.* revealed the most probable reaction pathway for the production of CO in [EMIm][BF_4] [52]. There the formation of an IL-COOH species was predicted as key intermediate. The decomposition of this intermediate then leads to the formation of carbon monoxide.

In order to evaluate the influence of the role of the C_2 position of the imidazole cation, different [BMIm] and [BMMIm] based ionic liquids were investigated by *Niu et al.* [87]. Experimental and theoretical results on silver electrodes underlined the dominant role of the choice of the cation. Here, the C_2 position was found to be very important for the chemical interaction of ionic liquid with CO_2. *Lau et al.* found, that the C_4 and C_5 position of the imidazole ring are even more important [88]. Therefore, different ionic liquids with different chemical groups at the C_2 position were investigated. No difference in CO_2RR activity compared to [BMIm]$^+$ cation was found by blocking the C_2 position with alkyl or aromatic groups. But the activity dropped when blocking the C_4 and C_5 position of imidazole. Hence, these two positions were declared as important for the stabilization of CO_2^- at the electrode surface.

The unimportance of the blocking of the C_2 position was further proven by the results of *Montiel et al.* [89]. Therefore, the IL-electrode surface interaction is really important for the CO_2RR. The dynamics of the structural transition at the electrode surface determines the onset potential of CO_2RR [83]. On the other hand, surface adsorbed ionic liquids are influencing the structural and electronic properties of the microenvironment at the electrode [90]. This is the reason for the shift of selectivity in CO_2RR with ionic liquids. Using a Pb electrode in acetonitrile for example, the use of ionic liquids can shift the product selectivity from oxalate to carbon monoxide [91].

2.3. Electrochemical cells in CO_2RR

2.3.1. Problem of CO_2 solubility

One big issue in CO_2RR is the solubility of CO_2 in the electrolyte. As mentioned before, the standard electrolyte consists of a potassium bicarbonate solution. The solubility of CO_2 in water is strongly dependent on the applied pressure [50] and the temperature applied [92]. At standard conditions (25 °C. p = 1013 mbar), solubility of CO_2 in water is as low as 0.14 g/100 g water.

Therefore, two possible ways to overcome poor CO_2 solubility in aqueous electrolytes are either increasing the system pressure or decreasing the temperature of the electrolyte system. *Saeki et al.* published in 1995 their results about CO_2 reduction in methanol at higher pressures [93]. At higher pressures, CO_2 could be effectively reduced to CO (< 40 % FE) by producing minor amounts of hydrogen (4 % FE) at current densities of -500 mA/cm^2. The improvement in current density by applying higher pressure could also be shown by *De Jesus-Cardona et al.* for aqueous electrolytes [94]. At the same time, *Mizuno et al.* were successful in reducing hydrogen evolution reduction (8 % FE) during CO_2RR by using reduced temperatures of -30 °C [95].

In methanol as solvent, CO_2 could be effectively reduced to methane (< 40 % FE). The same group investigated also the temperature dependence of CO_2RR in aqueous sodium carbonate solution [96]. As mentioned before, a third opportunity is the use of organic solvents as methanol in combination with soluble metal salts. Some works can be read in [97, 98, 99, 100].

2.3.2. Different types of electrochemical cells

The electrochemical cell is an important tool in the realization of electrochemical reactions. While for other processes there are well known reactor configurations on the industrial scale [20], there is no unique reactor used in CO_2RR. Different reactor types are presented in a review article of *Bevilacqua et al.* [101] and will be further discussed in this section. While for industrial applications electrochemical cells are used in a two electrode set-up, in laboratory investigations, the three-electrode set-up is preferred. Scheme 9 shows a typical principle of a three electrode set-up. This set-up consists of three different electrodes. The working electrode (WE), the reference electrode (RE) and the counter electrode (CE). In CO_2RR, the working electrode is one of the electrode materials discussed in the previous sections. Since the cathodic reaction (reductive reaction) is the interesting one in CO_2RR, it is of interest to measure parameters like product selectivities or current densities at defined potentials. Therefore, the reference electrode is needed. Typical reference electrodes in

CO_2RR are either Ag/AgCl or RHE. Every electrochemical reaction needs to have a second reaction in order to close the electrical loop. In case of CO_2RR, the Anode reaction (oxidative reaction) is usually the OER. As typical anodic material platinum is used. In order to prevent oxidation of products at the anode out of CO_2RR, it is crucial to separate the anode and the cathode by a membrane. Typical membranes used here are Nafion, a polymer membrane with sulfonic acid groups, or Selemion, a membrane with basic quarternary amine groups.

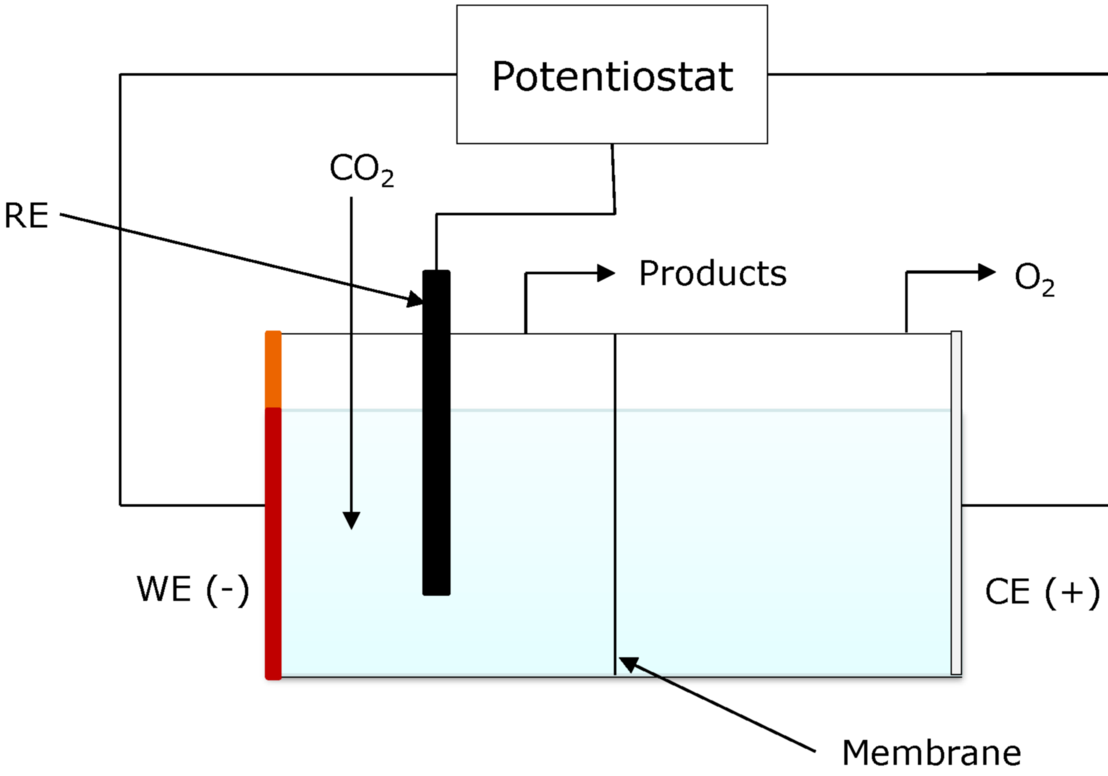

Scheme 9: Principle of an electrochemical cell for CO_2RR. WE: working electrode, CE: counter electrode, RE: reference electrode.

The most commonly used reactor type is the H-type cell, like the one used in [102]. A closer look into literature on electrochemical engineering shows, that a big disadvantage of the H-type cell is the inhomogeneous electrical field at the electrode, which influences the current distribution at the electrode surface [20]. The group of Jaramillo developed a parallel plate electrochemical reactor, which has a much more homogeneous current density distribution at the electrode surface [10, 20]. The H-type cell design principle is shown in scheme 10. The design principle of the parallel plate reactor can be seen in the paper from the group of Jaramillo [10].

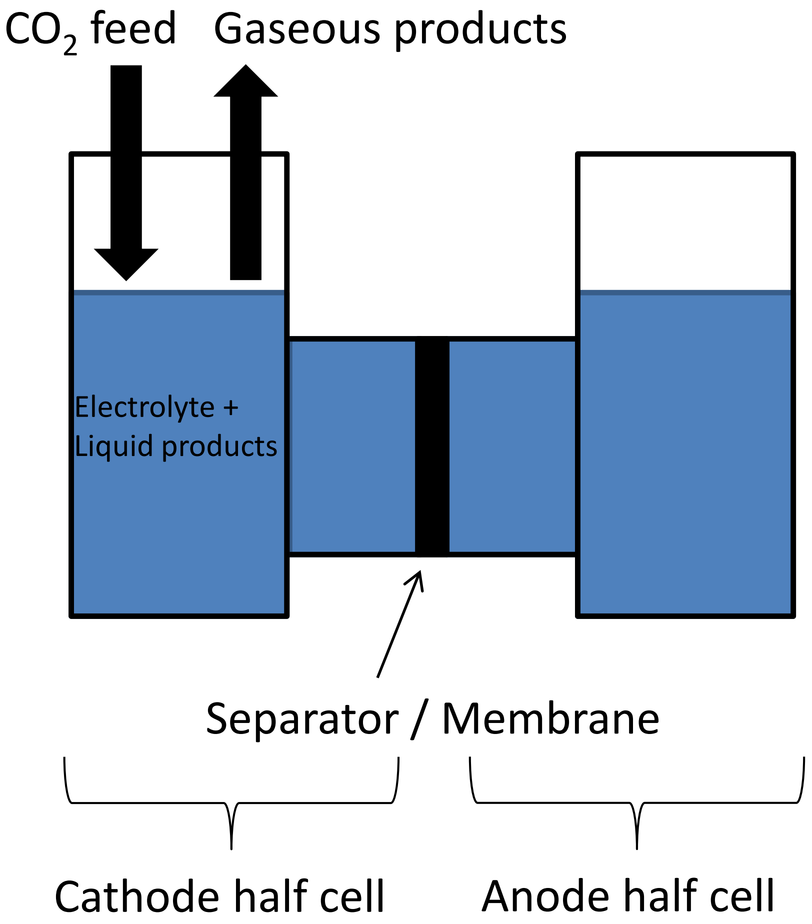

Scheme 10: Principle design of an H-type cell used for CO_2RR.

In 2003, *Köleli et al.* introduced a fixed bed reactor which was able to convert CO_2 into formic acid without the use of a membrane [103]. The advantage of a fixed bed reactor is a much expanded catalysts surface. The reactor is illustrated in the appropriate paper [104].

Recent research in CO_2RR also uses microfluidic flow cells [105] (scheme 11). Here, the two electrodes are separated by a flowing liquid electrolyte. The half-cell performance can be investigated by using an external reference electrode. This reactor type allows fast investigations under different reaction conditions. Different types of flow cells were established, as there is the parallel plate cell [106], the trickle-bed reactor [107] or the filter press electrochemical cell [108, 109].

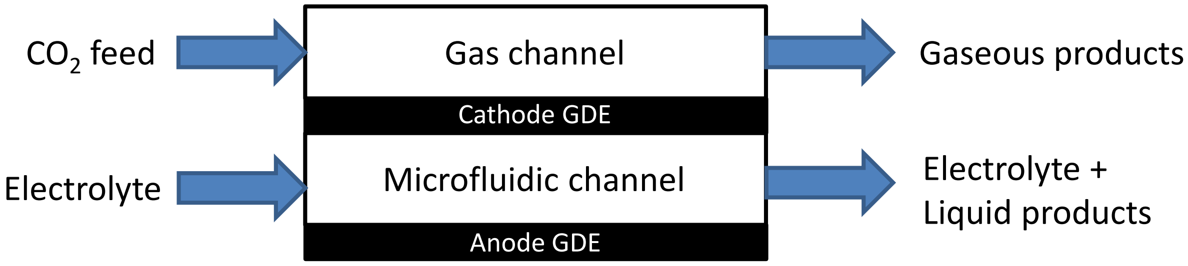

Scheme 11: Design principle of a microfluidic flow cell reactor used for CO_2RR.

Further improvement in terms of ohmic potential losses and therefore energy efficiencies could be achieved with membrane electrode assemblies (MEA's). This cell configuration is well known in fuel cell applications. *Wu et al.* [110] or *Bevilacqua et al.* [111] were using such MEA-based cell designs for the electrochemical reduction of CO_2. Schemes of the reactors can be seen in the appropriate papers of *Wu et al.* [110] or *Bevilacqua et al.* [111].

2.3.3. Influence of metal impurities on CO_2RR

As described prior, different metals show different selectivities towards different CO_2RR products. Since iron is known for favoring the HER, this metal can make some trouble in copper catalyzed CO_2RR, even in trace level concentrations. It is due to the fact, that the overpotential for HER is much lower than for CO_2RR, as described in prior chapters. There are no systematic studies, focusing on the purity influence of copper or the electrolyte in CO_2RR, but all research groups are using copper or electrolyte with a high purity quality.

Copper with low a low level of trace metal content at the surface can be achieved by different methods. The easiest is to use copper with a very high purity. *Dutta et al.* for example were using a copper substrate made with physical vapor deposition from BASF SE [15]. Here, copper was deposited on a silica based semiconductor material of high purity. The results show high faraday selectivities for CO_2RR products as for example ethylene and relatively low faraday selectivity for hydrogen. The group of Jaramillo used a very pure commercial available copper foil (99.999 % metal basis) and treated the surface by mechanical polishing and further by electrochemical polishing in phosphoric acid [10]. Also here, FE's of around 30 % for ethylene could be achieved and hydrogen evolution could be disfavored in comparison to CO_2RR. Anodization with concentrated phosphoric acid was also done by *Jiang et al.* [112], but the pre cleaning step was different to Jaramillo. Here, no mechanical polishing was used before anodization, but a surface treatment with diluted sulfuric acid was done. A study from 1992 including the same procedure also showed that the pretreatment of copper is really important [113]. Here, depending on the polishing procedure combination of the anodization steps, the catalytic activity of the catalyst could be improved in comparison to the untreated catalyst. In a first step, copper foil was washed with warm dichloromethane followed by treating the metal surface with concentrated hydrochloric acid before an anodization in concentrated phosphoric acid. A second procedure further treated the metallic surface with a potassium chloride anodization step, showing the absence of metal impurities after EDS analysis.

Also trace metals in the electrolyte are able to poison the catalyst and thus suppressing the CO_2RR product formation. A group from Massachusetts Institute of Technology described the improvement of group eleven CO_2RR catalysts performance by capturing trace metals from the electrolyte solution [114]. During the reduction process, also trace metal ions are reduced and deposited on the catalytic surface. This blocks active sites for CO2RR product formation. Since the trace metal impurities are boosting HER, the ratio of the consecutive reactions CO_2RR and HER is shifted towards HER. Metal ions can be simply captured by complexation. Therefore, ethylene diamine tetra acetate (EDTA) was used for the trace metal capturing. It could be proved, that the complexation hinders trace metal ions to deposit on the catalytic surface and thus favoring CO_2RR. By combining copper catalyst's surface peroxidation and trace metal capturing with EDTA in the electrolyte solution, the group of Strasser was successful at keeping the reaction rate for ethylene production after 20 h still at 91 % [115]. But also selectivities within CO_2RR products can change by trace amounts of other catalytic active metals for CO_2RR. For example, trace amounts of silver on the catalytic surface of copper catalysts can change the selectivity from hydrocarbons to carbon monoxide [116]. Using a Ag/AgCl reference electrode can contaminate the electrolyte with silver ions and lead to silver metal deposition on the copper catalyst. This problem can be solved by using a double-junction Ag/AgCl reference electrode instead of a single-junction Ag/AgCl reference electrode.

3. Goal and Content

As the state of the art shows, Cu-foams are attractive as catalysts for CO_2RR with high ethylene yields. Possibilities to modify these catalysts are rare up to now. New possibilities to modify the catalyst on a chemical and structural level can not only lead to different product distributions, they can also give more mechanistic insights.

While different pathways are proposed, the mechanistic pathway during CO_2 reduction on Cu is still under debate. A clear influence of mass transfer and CO_2 solubility seems to take place, but is also not fully quantitatively understood. Structural and chemical changes of the catalyst and studying the influence on the product distribution can also give mechanistic insights.

In this sense, this thesis has the aim to study possibilities to vary mechanistic and chemical properties of Cu foam catalyst. Furthermore, to allow correlations of these changes to CO_2RR activity and selectivity, an experimental setup and procedure working at high current densities and with high reproducibility needs to be developed.

Since there is no benchmark reactor or set-up in the CO_2RR community, both had to be developed prior. In these studies, an H-type cell and two parallel plate cells made of different polymer materials were investigated regarding their performance. As in literature cationic membranes as well as anionic membranes were used, the influence of the membrane polarity on the overall CO_2RR performance was investigated. Subsequently, the experimental protocol and the error evaluation of the measurement procedures needed to be done. Especially concerning the iR drop calculation and thus the correction of the applied potential, the error evaluation was very important. But also the error in the online GC gas phase analytics was evaluated. Here, the different product gases were analyzed according to their fluctuation over the whole electrolysis time.

Before the SCILL concept was finally applied to copper foam catalysts, investigations on the properties of copper foam catalysts were done at first. Therefore, forced convection through stirring was applied during the synthesis of the copper foam materials in order to better control the materials properties. A comparison of the activities and selectivities in CO_2RR between the copper foam catalysts synthesized by the literature protocol and the modified protocol was done subsequently.

In the end, the SCILL concept for the copper foam synthesized by the literature protocol was investigated for the two different ionic liquids [BMIm][NTf_2] and [BMMIm][NTf_2]. The results of [BMIm][NTf_2] were compared to the results obtained by using the same amount of ionic liquid as electrolyte additive. These results were the basis for first predictions on the mechanistic impact of ionic liquids as chemical trapping agents. Furthermore, the anion influence was investigated.

4. Experimental section

4.1. Synthesis of copper foam catalysts

4.1.1. Copper support pretreatment

Copper plates (99.99 %. Alfa Aesar) were pretreated by adopting a literature protocol [112]. At first, copper plates were pre-cleaned from impurities by ultrasonication in concentrated sulfuric acid (96 %, Suprapur, Merck) for 15 minutes in a 100 ml beaker. The pre-cleaned copper plates were anodized in ortho-phosphoric acid (85 %, EMSURE ACS, Merck) in a 100 ml beaker by applying a voltage of 3 V vs. Ag/AgCl (3 M NaCl) for 3 min. The experimental set-up is given in scheme 12.

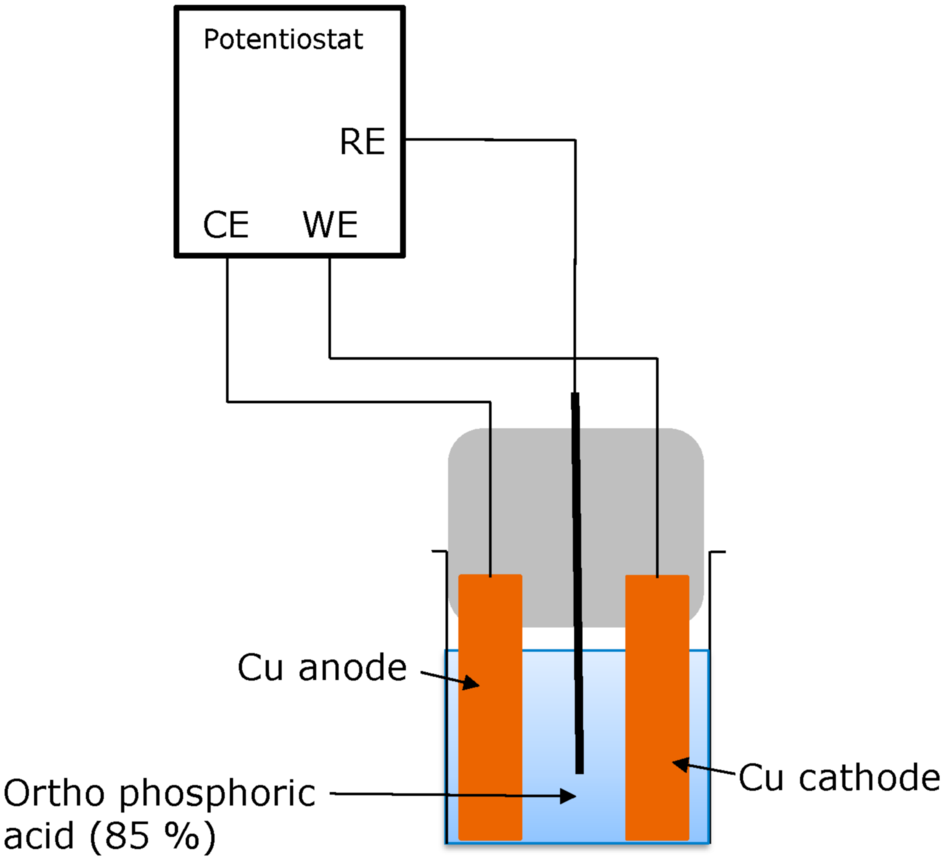

Scheme 12: Experimental set-up for Cu anodization.

4.1.2. Copper foam synthesis

4.1.2.1. Synthesis under free convection conditions

Copper foam was synthesized by a literature protocol [14, 15]. Two copper plates were fixed in a polypropylene holder in a distance of about 2 cm and immersed into a plating bath containing 1.5 M sulfuric acid (96 %, Suprapur, Merck) and a 0.2 M copper sulfate solution (99.999 %, Puratronic, Alfa

Aesar) in a 100 ml beaker (scheme 13). The exposed geometric surface area (A_{geo}) was 5.7 cm^2. For the electrodeposition, a HMP4040 potentiostat (Rhode and Schwarz) was used and a potential of 12 V and 10 A was applied between the copper cathode and the copper anode. The electrodeposition time was controlled by the coulombs registered in LabView. After the electrodeposition, the resulting copper foam was thoroughly rinsed with ultrapure water (VWR). Surface morphology of the copper catalysts was analyzed by scanning electron microscopy (SEM, Philips XL30 FEG) operated at an accelerating voltage of 30 kV.

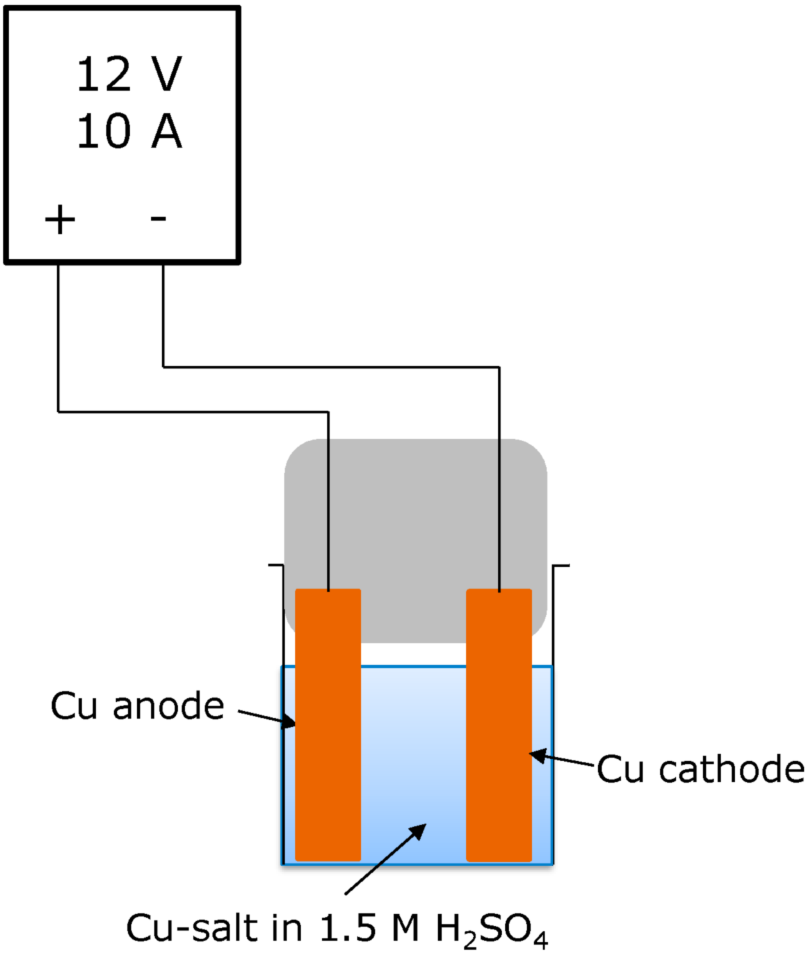

Scheme 13: Experimental set-up for copper foam synthesis under free convection conditions.

4.1.2.2. Synthesis under forced convection conditions

The experimental set-up for the electro synthesis of copper foam catalysts with applied forced convection is the same as for the synthesis under free convection conditions. Here, a magnetic stir bar is used to apply forced convection. The experimental set-up is shown in scheme 14.

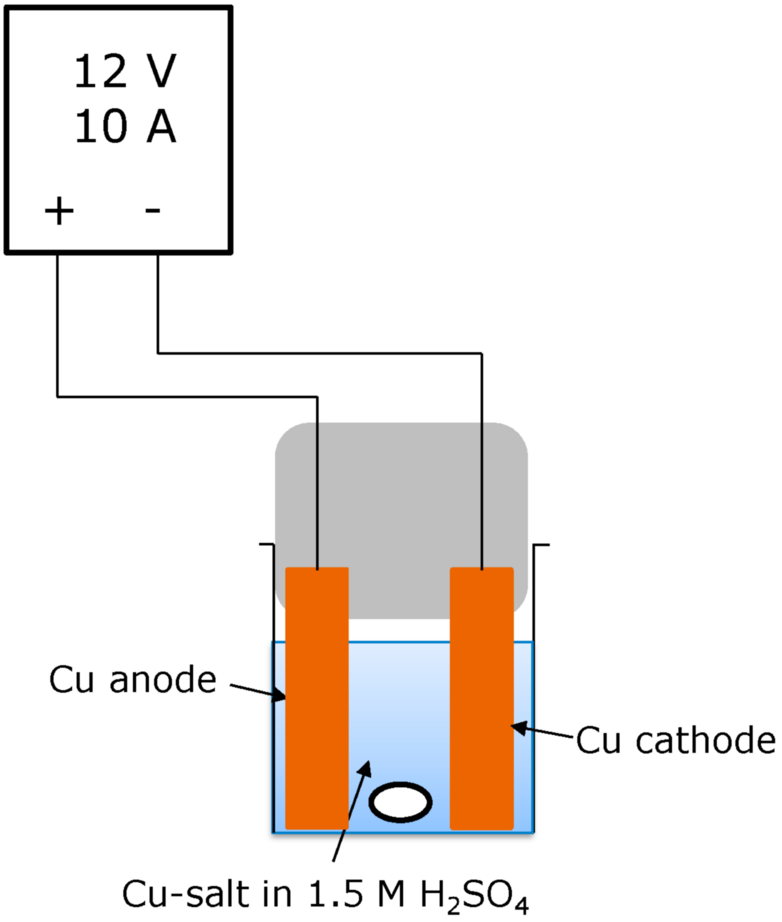

Scheme 14: Experimental set-up for copper foam synthesis under forced convection conditions.

4.2. Electrochemical active surface and roughness factor

Electrochemical active surface (ECAS) of copper foams were determined by the dimethyl viologen method [15]. Prior to the ECAS determination, the diffusion coefficient of dimethyl viologens chloride ($DMVCl_2$) was determined with the Randles-Sevcik equation

$$i_p = 2.69 \cdot 10^5 z^{3/2} A c D^{1/2} v^{1/2} \qquad \text{(IV)}$$

with the maximum peak current i_p, the number of transferred electrons z, the concentration of the redoxactive species c, the $DMVCl_2$ diffusion coefficient D and the potential sweep rate v. Therefore, cyclic voltammetry (CV) curves in 40 mL of an argon purged aqueous 1 M sodium sulfate (99 %, Arcos) solution containing 10 mM $DMVCl_2$ (98 %, Arcos) as probe molecule in a 100 ml beaker were conducted at different scan rates. The scan rates were 5, 10, 25, 50 and 100 mV/s. The copper foam catalyst was fixed in a polypropylene holder together with a copper counter electrode and immersed in a 100 ml beaker filled with 40 mL of an aqueous 1 M sodium sulfate solution containing 10 mM $DMVCl_2$ as probe molecule. After purging the electrolyte with argon for 30 min, cyclic voltammetry

(CV) curves were conducted at the same scan rates as mentioned above. The ECAS can be determined by plotting i_p vs. $v^{1/2}$.

The roughness factor (R_f) is calculated by

$$R_f = \frac{ECAS\ [cm^2]}{exposed\ geometric\ surface\ area\ [cm^2]} \quad \text{(V).}$$

4.3. Preparation of SCILL catalysts

Copper foam catalysts were used for the concept of solid catalysts with ionic liquid layer (SCILL). Therefore, copper foam catalysts exposed geometric surface area was reduced to 1 cm^2 for usage in CO_2RR set-up. Here, 10 µL of a mixture of isopropanol (99.9 %, Carl Roth) and ionic liquid in a defined volume ratio was dropped onto the copper foam catalyst. The impregnated foam was dried in air for 30 min to get rid of isopropanol.

The whole procedure is illustrated in scheme 15.

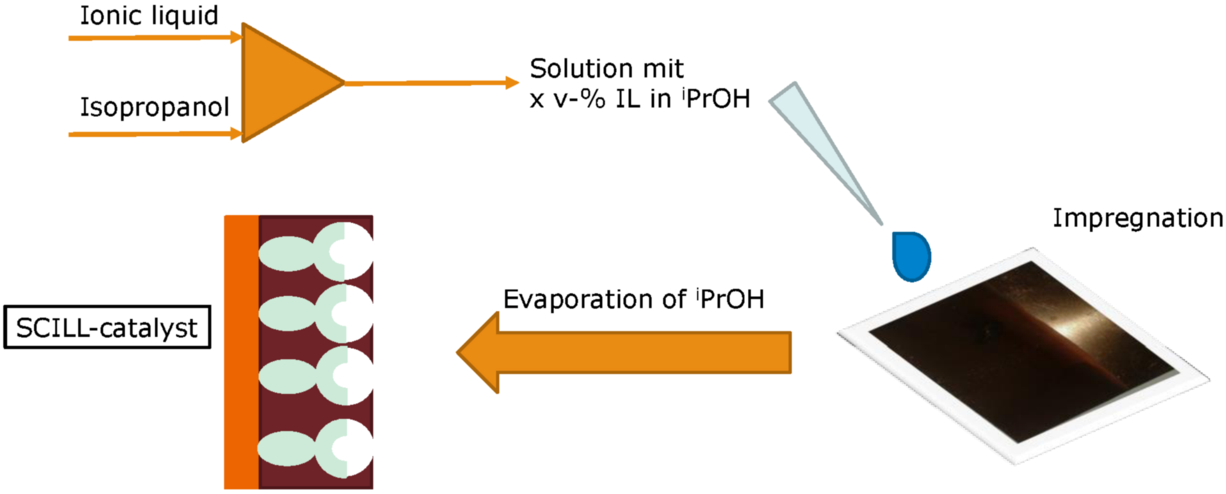

Scheme 15: Impregnation process for preparation of SCILL catalysts.

4.4. Membrane pretreatment

4.4.1. Nafion 117 membrane

Nafion 117 cation exchange membrane is pretreated (cleaned and activated) by a literature protocol [117]. The pretreatment contains four steps. In the first step, Nafion 117 membrane is heated for 1 h at 80 °C in 3 wt.-% H_2O_2. Afterwards, the same membrane is heated for 1 h at 80 °C in water. The last two steps are heating the membrane for 1 h at 80 °C in 1 M H_2SO_4 and the repetitions of the heating step in water. There results an activated Nafion 117 membrane which is stored in ultrapure water for 24 h prior to use in CO_2RR.

4.4.2. Fumapem FAA-3-50

Fumapem FAA-3-50 anion exchange membrane is activated by storing it 24 h in 1 M KOH.

4.4.3. Selemion AMV

Selemion AMV anion exchange membrane is activated by storing the membrane 24 h prior to the experiment in the appropriate electrolyte solution.

4.5. CO_2 electrolysis

4.5.1. Experimental set-up

The main part of the experimental set-up consists of two electrochemical cells R1 and R2. Three different reactors were used within these studies.

The first one is a typical H-type cell made of borosilicate glass (figure 6). Both compartments of the cell are fixed by an alumina flange with an inserted Viton sealing and stainless steel screws. The membrane is fixed by pressing it with the sealing to the glass. The cathodic compartment has space for the working electrode, fixed by a clamp, and the reference electrode. The volume of both anodic and cathodic compartment is 150 ml. Gas is fed to the cathodic compartment by an immersion tube with a double wall construction. Between the inner and outer wall, gas phase products can leave the reactor.

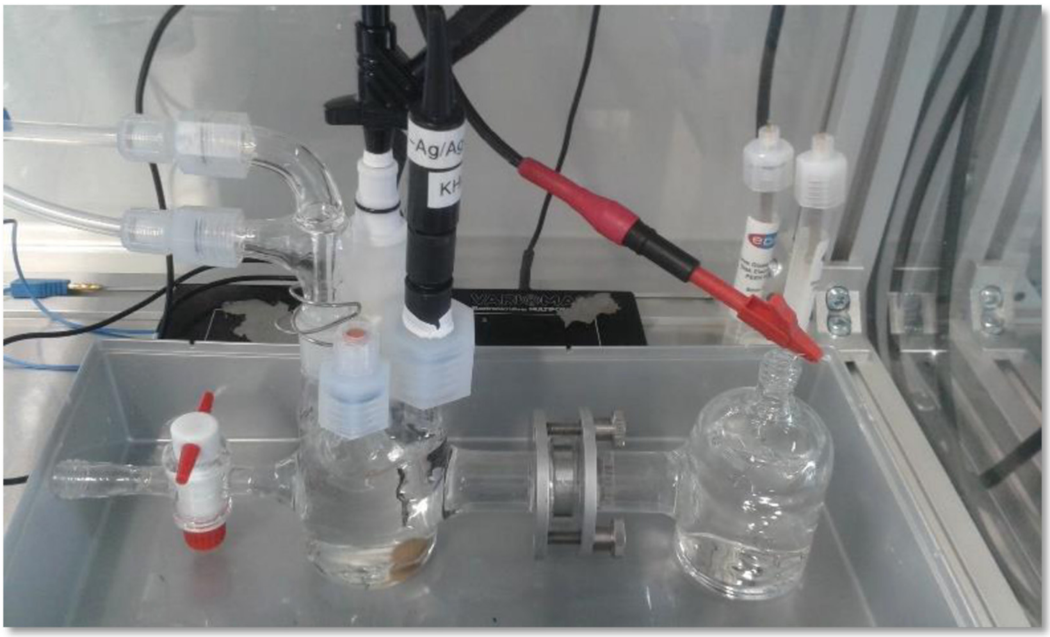

Figure 6: H-type glass cell for CO_2RR.

The second reactor was the PMMA electrolyzer, depicted in figure 7. This reactor follows a modular design. The volume of each anodic and cathodic compartment is reduced to 15 ml. The reactor is sealed by Viton O-rings. The working and the counter electrode are fixed by pressing them between the sealing of the appropriate half-cell by stainless steel screws. The membrane is fixed between the sealing dividing the anodic and the cathodic compartment. As current collectors, stainless steel screws were used. The reference electrode was immersed from top of the cathodic compartment. Gas feed for the anodic and the cathodic compartment were established from the side.

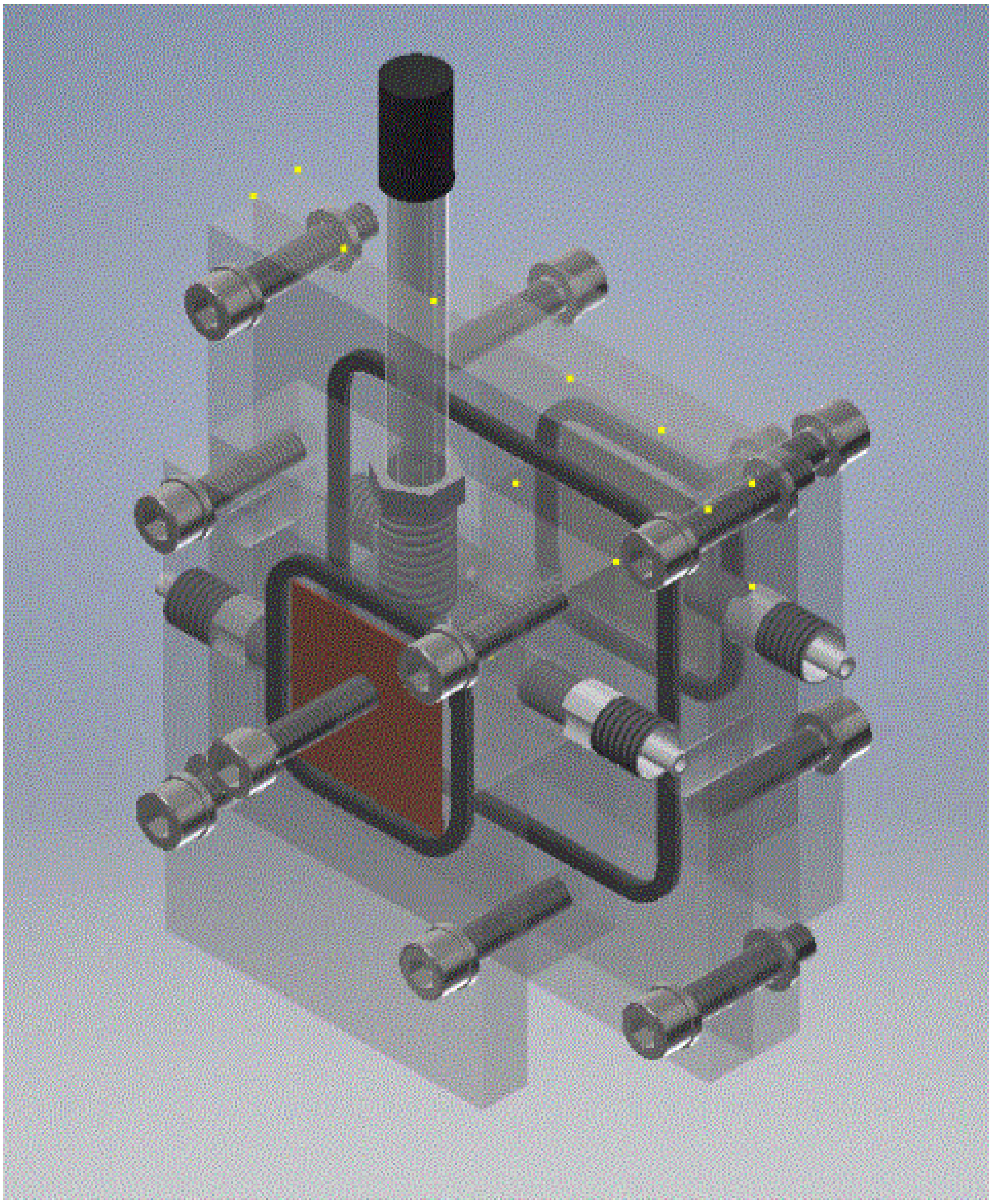

Figure 7: CO_2RR semi-batch reactor of the 2nd generation: PMMA electrolyzer.

The third type of reactor is made of PEEK. Here, also the modular design was used. The electrolyte volume was further reduced to 5 ml for the cathodic compartment and 8 ml to the anodic compartment. The sealing of the working and the counter electrode as well as the fixation of the membrane was done by pressing them to the appropriate sealing O-rings with stainless steel screws. The sealing material was again Viton. As current collectors, copper stripes were used as well for the cathodic compartment as for the anodic compartment. Here, the reference electrode was immersed from the side of the cathodic compartment. Within this reactor, two different feed positions for the cathodic compartment were developed. One from the side (figure 8) and one from the bottom (figure 9).

Figure 8: PEEK reactor for CO_2RR with feed inlet from the side.

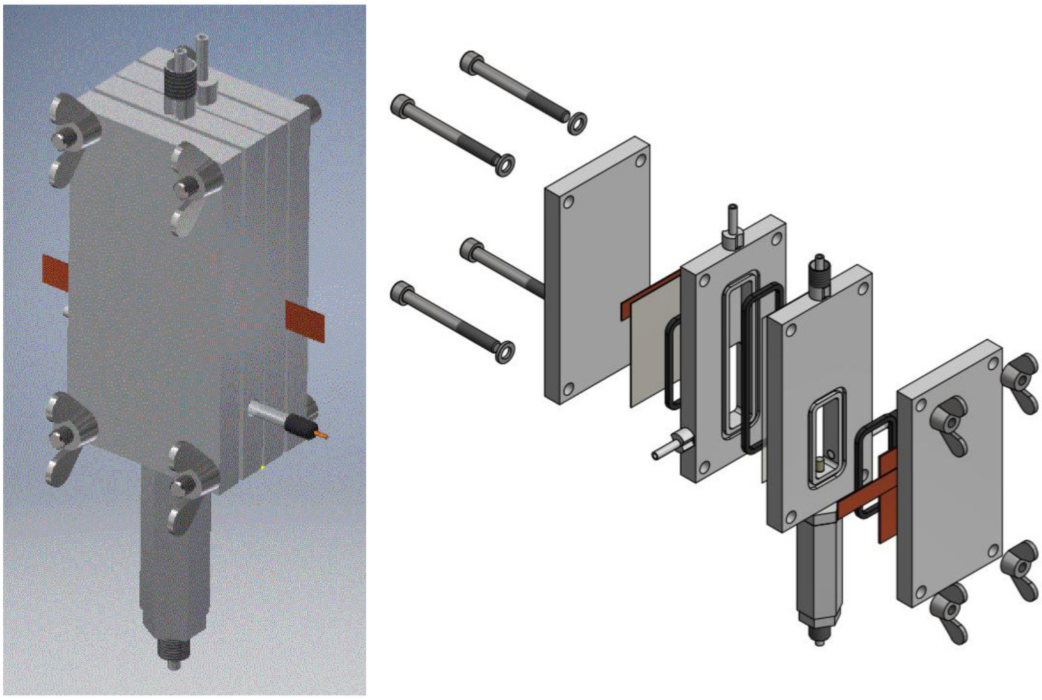

Figure 9: CO_2RR semi-batch reactor of the 3rd generation: PEEK electrolyzer.

The PEEK reactor could be cleaned by cooking in ultrapure boiling water for at least 1 h.

The cathodic compartment is fed with CO_2 by a mass flow controller (MFC, Cathode 1, Cathode 2) of the type FG-201CV-AGD-33-V-DA-000 from Wagner, which were bought calibrated in a range of 0 to 200 ml/min CO_2. The volume flux can be directly established by a digital controller which is installed outside of the experimental rig. For the anodic compartment, CO_2 can be fed by MFC (Anode 1, Anode 2). Anode 2 is the same type of MFC as for the cathode compartments. Anode 1 is a mass flow controller of the type F201C-FAC-33-V from Wagner which is calibrated by using a bubble counter in the range of 1.9 to 26.5 mL_N/min CO_2 (5 to 70 % of digital scale). Anode 1 is controlled by a control box from Wagner. Alternatively, inert gases argon or nitrogen can be fed by ball valves Inert 1 or Inert 2. CO_2 and inert gas lines are combined in front of the anodic compartments by a T-piece made of polypropylene with two check valves made of polypropylene.

The lines between each reactor and the MFC outlets are piped with PFA tubes with OD 6 mm. MFC's for CO_2 supply are fed by a stainless steel line with OD 6 mm. CO_2 supply can be interrupted by a ball valve and CO_2 is filtered from potential solid impurities by a filter to protect the MFC's. Between filter and MFC's there is a further stainless steel line with OD 6 mm which allows to feed every MFC with sample gas. Sample gas can be connected by a quick coupling.

Inert gas volume flow is controlled by a rotameter (Kirchner und Tochter). Before entering the rotameter, inert gases argon and nitrogen are combined in one single line. Each line can be separately interrupted by a ball valve. Four lines can be fed with inert gas from the rotameter. Each of them are closed or opened by ball valves. Inert 1 and Inert 2 are discussed before. Inert 3 and Inert 4 are installed as back-up.

The whole flow sheet of the electrochemical set-up can be seen in scheme 16.

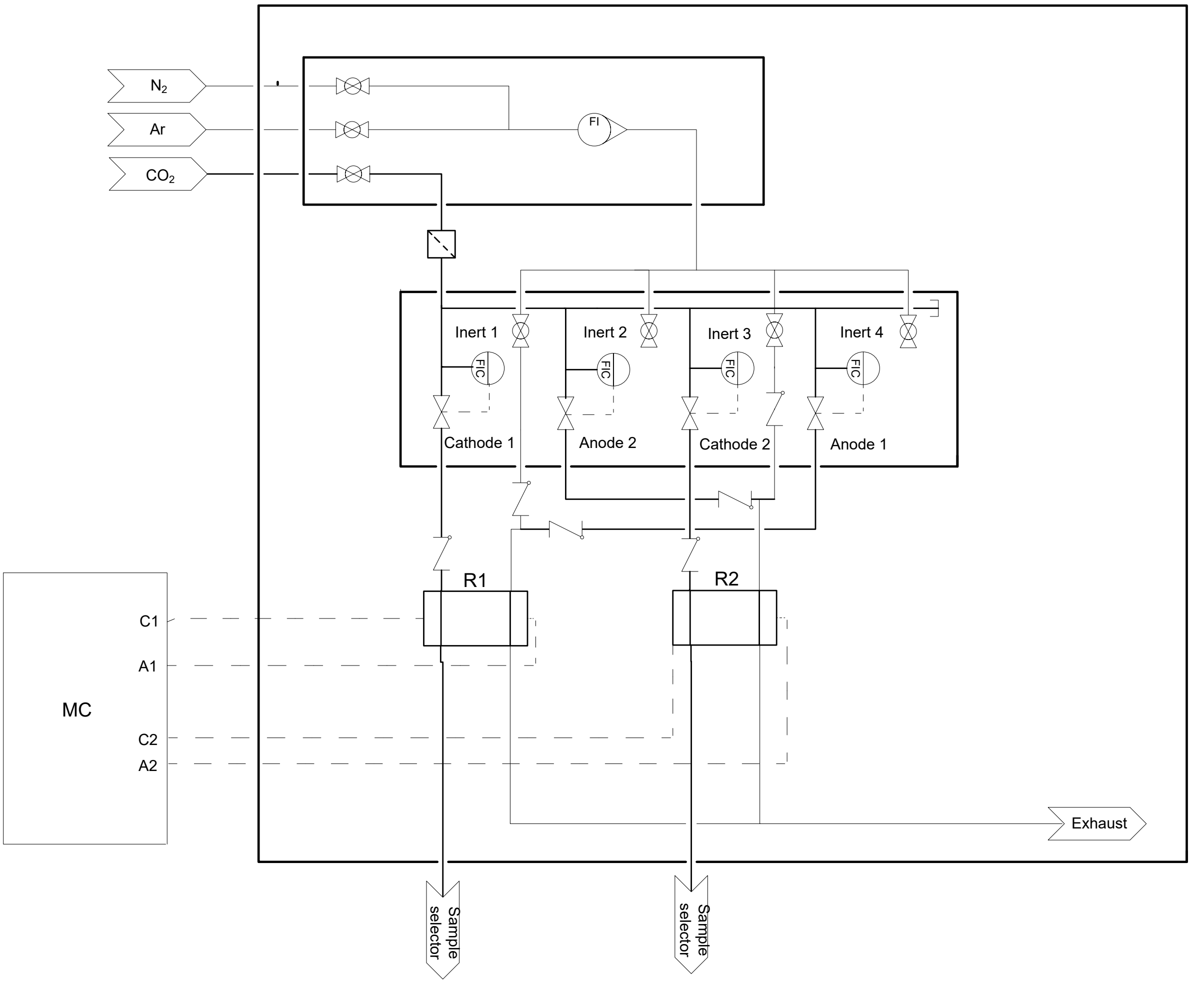

Scheme 16: Flow sheet of CO_2RR experimental set-up.

The product gas mixtures from the cathodes are separately leaving the reactor headspace to a sample selector valve. The reactor head space is connected to a PFA tube filled with silica gel (150 A. Arcos) as water adsorbent fixed with glass wool. To ensure, that no solid is taken with the gas outlet flow and thus blocking the 1/16" capillaries of the sample selector valve or the selector valve itself, a filter is installed after the adsorbing tube, schematically drawn in scheme 17.

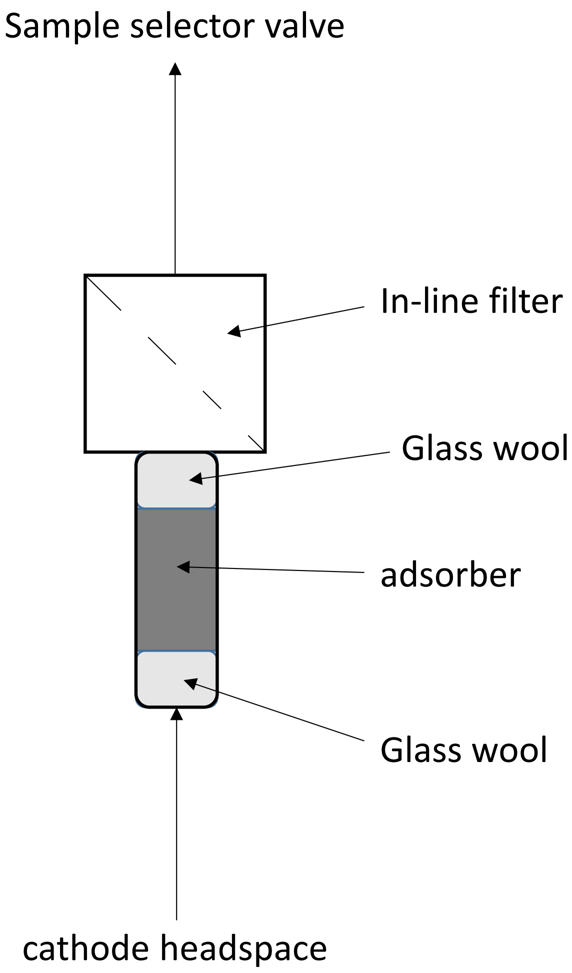

Scheme 17: Adsorber-filter unit.

Gases from the anodic compartments are combined and leave the experimental rig to the exhaust.

The electrochemical cells are connected to a PARSTAT multichannel potentiostat from Ametek equipped with five separate channels. Electrochemical measurements are monitored and controlled with the VersaStudio software.

Gases from the reactors for analysis can be chosen by the gas sample selector. The gas sample selector is an eight port valve from Vici Valco where either reactor 1 (R1/S1) or reactor 2 (R2/S2) can be selected (scheme 18). The selected reaction gas is connected to the GC sample loop while the unselected reaction gas is directly going to the exhaust. The selector is coupled to the GC and valve position switching is controlled by the GC method. The current valve position can be observed on a digital controller screen outside of the experimental rig. Valve positions that are not connected to one of the two reactors are blinded.

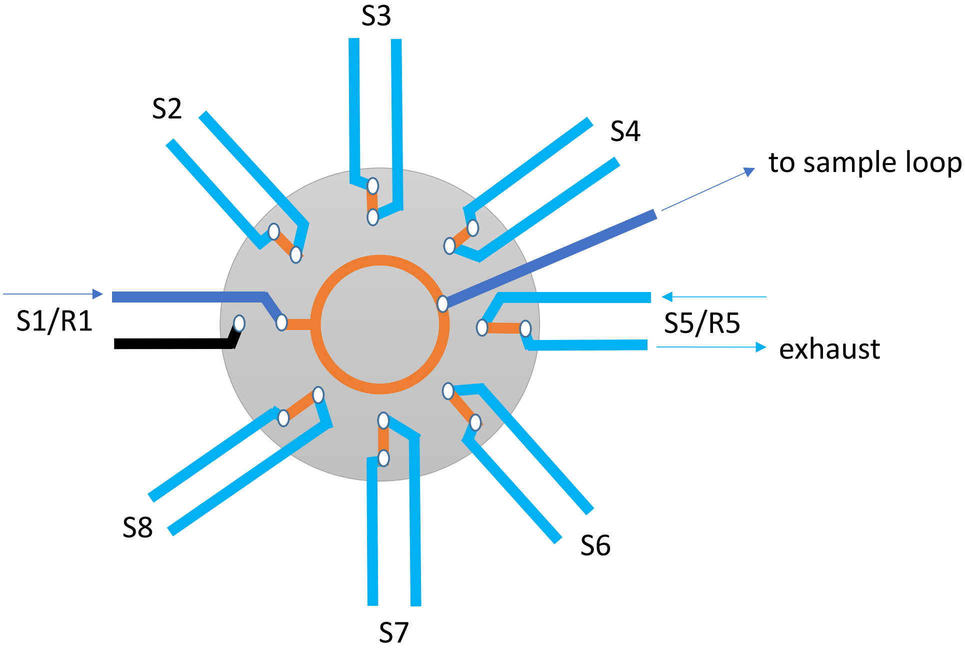

Scheme 18: Sample selector valve.

4.5.2. Experimental procedure

Electrochemical studies were carried out with a PARSTAT multichannel potentiostat (Ametek). At the beginning, the solution resistance (R_u) was determined by electrochemical impedance spectroscopy (EIS). The frequency range was from 100 Hz to 0.01 Hz. The R_u value was taken at the highest measured frequency. To pretreat the copper foam catalysts (reduction of CuO_x to Cu), CV's were running with five cycles in the range of -0.5 to -1.8 V vs. Ag/AgCl (3M NaCl) followed by a linear sweep voltammetry (LSV) in the range of 0 V to -1.8 V vs. Ag/AgCl (3M NaCl). Afterwards, a second EIS was conducted to be able to more precisely compensate the potential drop before applying a defined electrolysis potential for 1 h (chronoamperometry). Here, only 85 % of the resistance value from the second EIS was compensated by the potentiostat to avoid potential oscillations during the measurement. The left 15 % was post-corrected by

$$E_{Ag/AgCl.corrected} = E_{Ag/AgCl.applied} - R_u \bar{I}_{measured} \qquad \text{(VI)}$$

with the iR-corrected potential $E_{Ag/AgCl.corrected}$, the applied potential $E_{Ag/AgCl.applied}$, the solution resistance R_u and the mean measured current $\bar{I}_{measured}$.

The corrected potential was converted to RHE by

$$E_{RHE} = E_{Ag/AgCl.corrected} + 0.209 + 0.059pH \qquad \text{(VII)}$$

with the potential versus reversible hydrogen electrode (RHE) E_{RHE}, the iR-corrected potential $E_{Ag/AgCl.corrected}$, the potential of Ag/AgCl (3 M NaCl) electrode vs. standard hydrogen electrode (SHE) $E^0 = 0.209$ and the conversion factor between SHE and RHE 0.059pH.

Finally, a last EIS was measured, followed by an LSV.

4.5.3. Analytics

Gas phase products were analyzed by online gas chromatography (GC2030, Shimadzu). The GC configuration consists of a two way valve from VICI Valco with a 500 µL sample loop, a ShinCarbon ST Packed column (Restek, #19043), a splitter which separates the sample gas into two lines, a flame ionization detector (FID, Line 1) and a thermal conductivity detector (TCD, Line 2) (Scheme 19).

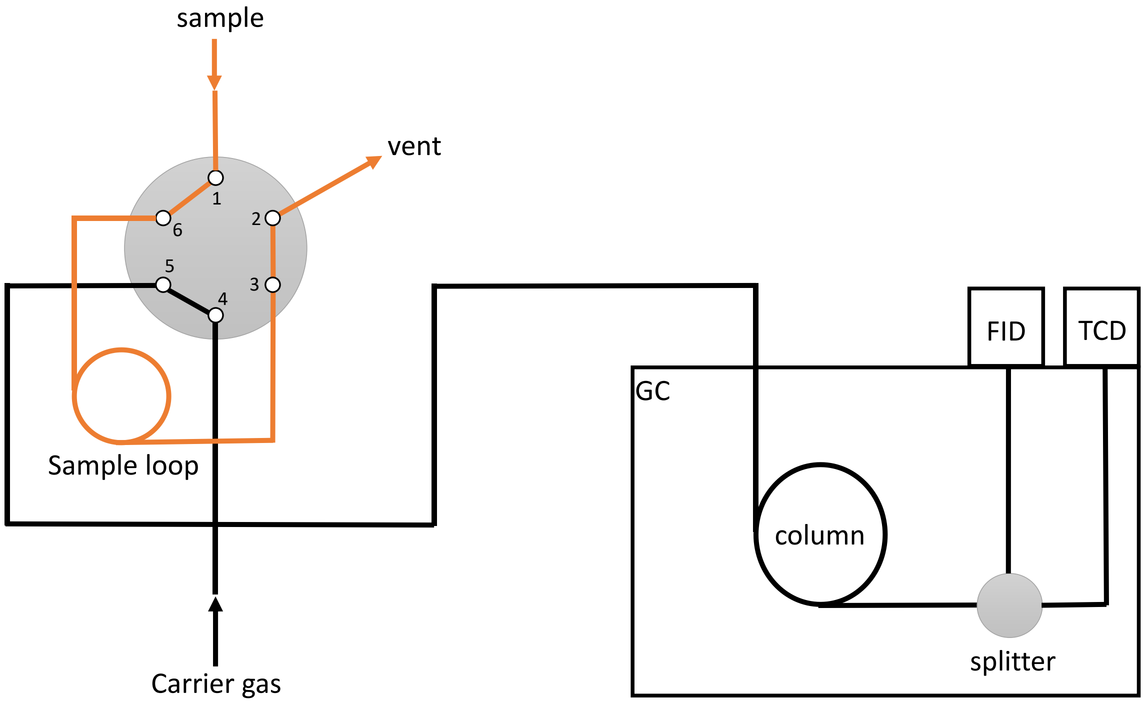

Scheme 19: Gas phase analysis with GC2030.

Samples were collected roughly every 13 min (GC method (CO2RR_Ar or CO2RR_Ar_multi), 11.33 min plus cool down to equilibrium state). Faradaic efficiencies were calculated out of the partial current of the product divided by the overall current at the moment of the injection

$$FE\,[\%] = \frac{I_i}{I_{tot}} = \frac{x_i[\%] \cdot z \cdot F \cdot \dot{n}_{CO_2}}{I_{tot}} \qquad \text{(VIII)}$$

with the partial current of product i I_i, the mole fraction of the product x_i, the number of transferred electrons z, the faraday constant F, the CO_2 molar flow $\dot{n}_{CO_2}$ and the overall current I_{tot}. The reported faraday efficiencies are the average of the injections.

The CO_2 molar flow is estimated by the ideal gas law

$$\dot{n}_{CO_2} = \frac{p\dot{V}_{CO_2}}{RT} \tag{IX}$$

with the operating pressure $p = 10^5$ Pa, the CO_2 volume flow $\dot{V}_{CO_2}$, the universal gas constant R and the absolute temperature T.

Product mole fractions are calculated by response factors determined by calibration of GC with sample gases of known concentrations. For each product, three different concentrations were used.

Liquid phase products were analyzed by NMR spectroscopy (500 MHz DRX 500, Bruker) by using the water suppression mode [118]. NMR sample was prepared by taking 500 mg of sample, adding 25 µL of 0.01 M maleic acid standard solution and adding deuterated water (99.9 %, Sigma Aldrich). Quantitative analysis is done by comparing the proton normalized area of maleic acid to the proton normalized area of a significant functional group of the product molecule.

5. Results and discussion

5.1. Copper foam synthesis

5.1.1. Repetitino of literature protocol

In order to adapt the experimental method for the copper foam synthesis, copper foam materials at different deposition times were synthesized according to the method described in the experimental section. The resulting copper foam materials were analyzed by SEM (figure 10).

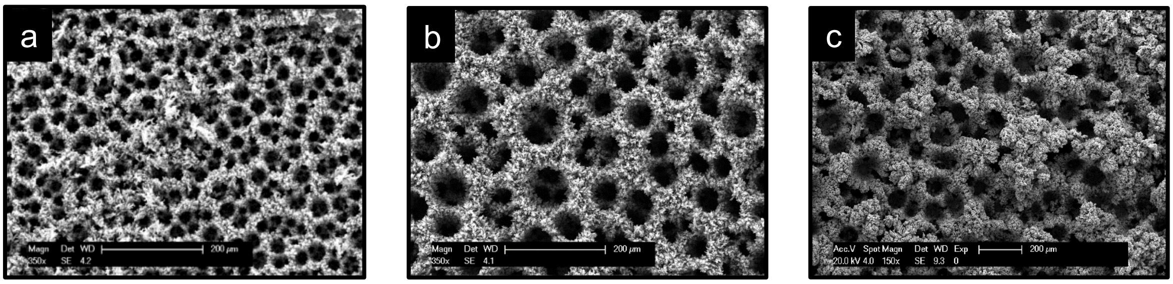

Figure 10: SEM images of Cu foam catalysts: CuF-SO4-15 (a), CuF-SO4-40 (b), CuF-SO4-60 (c). Synthesis at 12 V and 10 A.

In all cases, porous materials were obtained as expected. The structures are well defined pore systems. In order to characterize the material in more detail, the deposited mass was investigated at first, shown in figure 11. It needs to be mentioned, that there is a weighing error because of copper material oxidation after the electrodeposition. At this point, the mass is a rough estimation and copper oxide species are not considered.

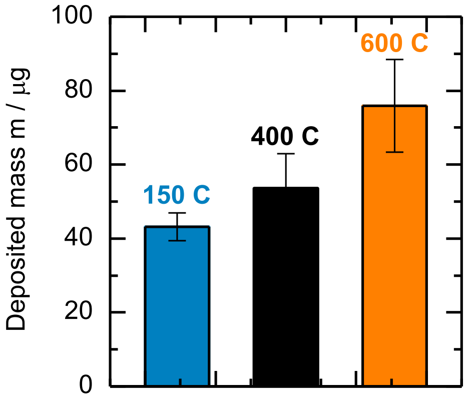

Figure 11: Deposited mass m for copper foam materials synthesized with different amounts of applied electric charge at 12 V and 10 A.

As expected, the more coulombs spent and thus the longer the time for the electrodeposition, the higher the mass of the deposited copper foam catalyst. The mass increases from about 40 µg at 150 C to about 80 µg at 600 C. But also the surface pore diameter is changing with increasing electric charge (figure 12).

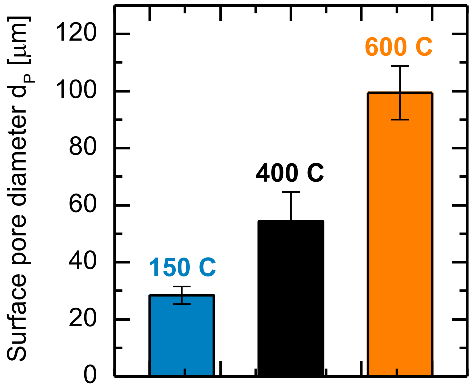

Figure 12: Surface pore diameter for copper foam materials synthesized with different amounts of applied electric charge at 12 V and 10 A.

The pore diameter is increasing with increasing electric charge. This could be due to the foam thickness, since the template bubbles have larger diameters with increasing foam thickness. From about 30 µm at 150 C, the increase goes from about 55 µm at 400 C to about 100 µm at 600 C. This result supports the hypothesis of a hierarchical pore structure development by increasing deposition time, as discussed in literature [14, 15]. This trend can be also seen regarding the foam thickness of the material, as depicted in figure 13.

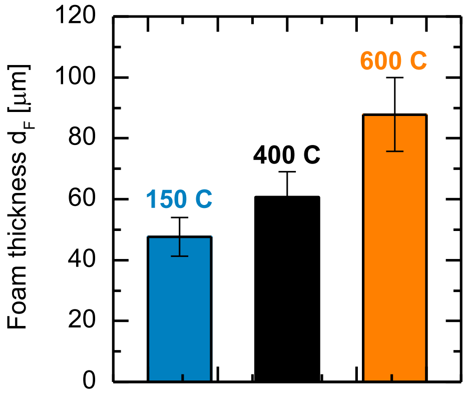

Figure 13: Foam thickness for copper foam materials synthesized with different amounts of applied electric charge at 12 V and 10 A.

The roughness factor of the three different materials (figure 14) was also changing by varying the amounts of applied electric charge for the electrodeposition. From 150 C to 400 C the roughness factor is increasing from about 4 to about 5. This can be explained by the higher mass of copper deposited and the bigger surface pore diameter. Increasing the coulombs to 600 led to a decrease of the roughness factor to 4. This can be explained by the material stability. At 600 C, the material is instable when measuring the roughness factor. This is stated by a visible material loss from the copper foam.

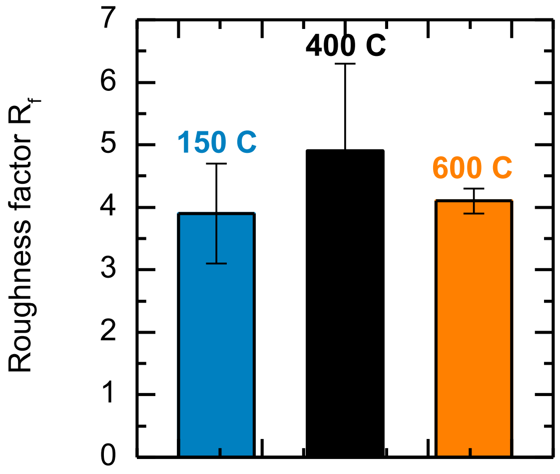

Figure 14: Roughness factors for copper foam materials synthesized with different coulombs at 12 V and 10 A

Comparing the parameters surface pore diameter and roughness factor to the literature shows a good agreement with published results [14, 15]. The results for the deposited mass, the surface pore diameter and the foam thickness for different copper foam materials show, that changing just the parameter deposition time by the applied coulombs, three material properties changed in parallel. This makes it hard to deduce the influence of a single parameter on the activity and selectivity.

5.1.2. Material properties achieved by new synthesis approach

In this section, the requirement to study the surface pore size influence to the electrochemical reduction of carbon dioxide is prepared. Therefore, a material is needed, where all parameters are kept constant apart from the surface pore size. The idea at this point is to introduce a new force component by stirring, which influences the copper ion mass transfer and also the hydrogen bubble removal from the copper foam surface, schematically drawn in scheme 20.

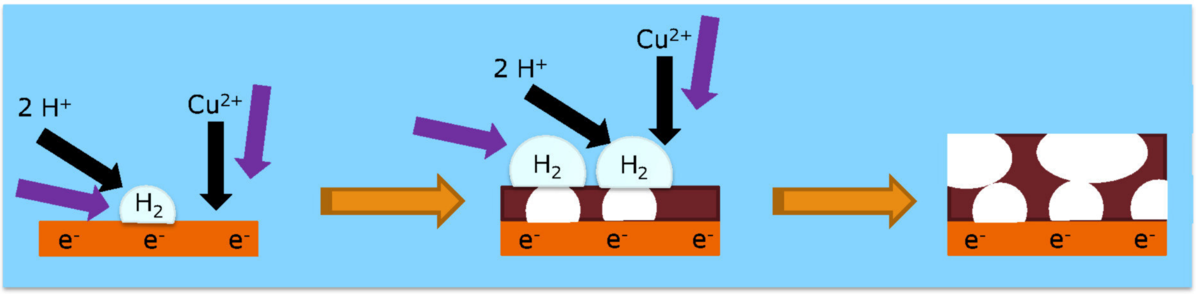

Scheme 20: Additional force components applied by stirring of the electrodeposition solution. Black arrow: material transport, purple arrow: forced convection, orange arrow: deposition progress.

The resulting copper foam materials are not changed in their porous structure as SEM images in figure 15 show. This is an important result in terms of maintaining the overall structure of the material.

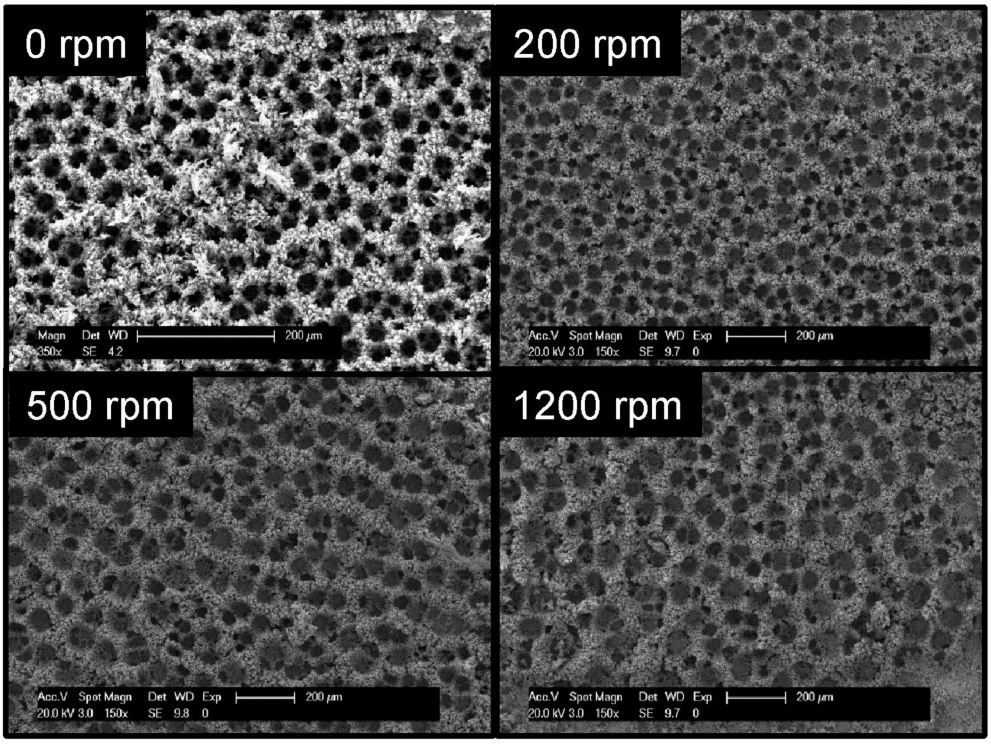

Figure 15: Copper foam morphologies for different applied stirring speeds. Deposition was always done at 150 C. Synthesis at 12 V and 10 A.

A closer look at the resulting surface pore diameter in figure 16 shows an increase of the surface pore diameter by applying stirring of the electrodeposition solution. By applying 200 rpm, it is possible to increase the surface pore diameter from 30 µm to 46 µm. Further increasing the stirring speed to 500 rpm increases the surface pore diameter to 62 µm. At 1200 rpm, a surface pore diameter of 76 µm can be achieved. This result confirms, that the application of forced convection is a suitable way to change the surface pore diameter.

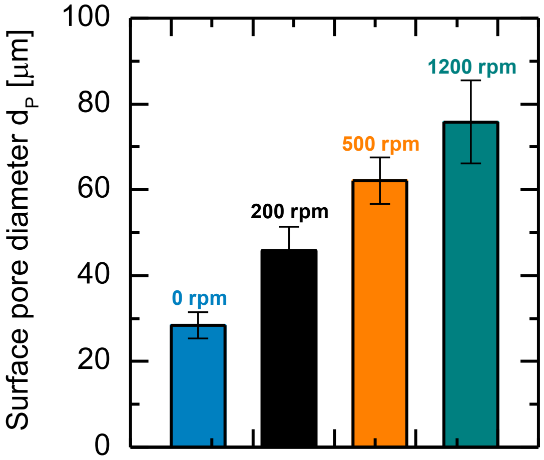

Figure 16: Dependency of surface pore diameter from different applied stirring speeds. All materials were synthesized at 150 C. Synthesis at 12 V and 10 A.

In order to see if the method was really successful in synthesizing a material where just the pore size is varied, it is necessary to investigate the deposited mass and the foam thickness. The deposited mass is independent from applying forced convection (figure 17). The value is always around 45 µg. This is a first success in applying a method which is able to vary one single material parameter.

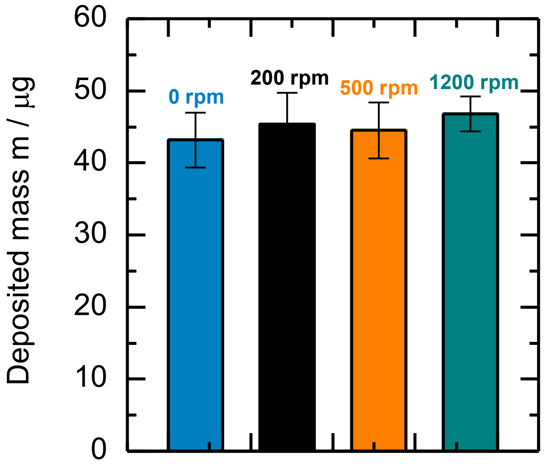

Figure 17: Dependency of deposited mass from different applied stirring speeds. All materials were synthesized at 150 C. Synthesis at 12 V and 10 A.

For the foam thickness, depicted in figure 18, stirring has an influence. By applying forced convection, the foam thickness is increased from 50 µm to about 70 µm. Varying the stirring speed does not further influence the foam thickness. Applying forced convection thus is an interesting method to selectively change properties of the material.

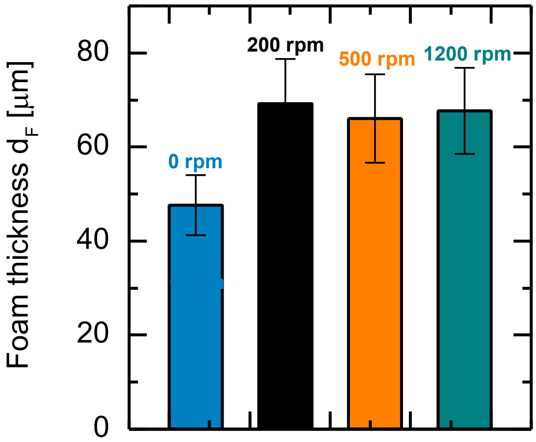

Figure 18: Dependency of foam thickness from different applied stirring speeds. All materials were synthesized at 150 C. Synthesis at 12 V and 10 A.

For the electrochemical characterization, the roughness factor was determined as described in the experimental section. The results are given in figure 19.

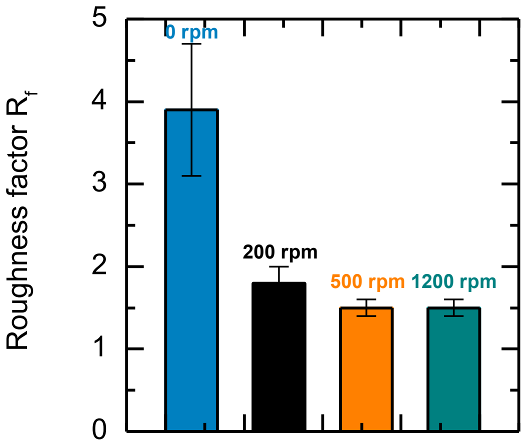

Figure 19: Roughness factors of copper foam catalysts synthesized at 150 C at different stirring speeds. Synthesis at 12 V and 10 A.

Stirring of the solution dramatically decreases the roughness factor from about 4 to below 2 for 200 rpm and to about 1.5 at 500 and 1200 rpm. The behavior is comparable to the results obtained for the foam thickness. Possibly the thicker foam has a bigger diffusion barrier for the redox mediator during the roughness factor determination. Furthermore, the increasing surface pore size provides decreasing electrochemical active material. But this influence is expected to be minor.

5.2. Electrochemical cell development and experimental protocol establishment

As explained in chapter 2, there is no unique reactor type used in CO_2RR. To be successful in establishing reproducible high current measurements, an experimental set-up was developed over 3 generations starting from the most simple to a more complex system. With this approach different aspects (e.g. analytics, cleaning, testing procedure) could be developed step by step and in parallel to designing the next generation setup.

5.2.1. H-type glass cell (1st generation)

The most common used reactor type is the H-type glass cell. Both cathode and anode half-cells were filled with 150 ml of electrolyte. The head space in the cathode half-cell was about one sixth of the whole volume (30 ml).

First experiments were carried out with an unpurified copper plate to investigate the performance of the electrochemical cell. Therefore, cyclic voltammetry (CV) curves were recorded in nitrogen purged electrolyte as well as in carbon dioxide purged electrolyte, depicted in figure 20 left. With the introduction of carbon dioxide to the reaction system, the current density at -1.0 V vs. RHE can be increased from -4 mA/cm^2 in nitrogen to -4.5 mA/cm^2. This indicates, that with the introduction of carbon dioxide the latter is converted by the catalyst. On the other hand, the increase in current density is just around 20 %. This means, that 80 % of the current is used for water splitting (hydrogen evolution reaction, HER). It must be stated here, that the issue of IR compensation was not payed attention yet. This will be a further point of discussion later on.

CV measurements were done with CuF-SO4-15 as shown in figure 20 right. In case of the copper foam catalyst, the introduction of carbon dioxide gives a completely other trend. The current density drops from -7.5 mA/cm^2 in nitrogen to -6.8 mA/cm^2 in carbon dioxide at -1.0 V vs. RHE. Two possible reasons could be postulated for this result. At first, the drop in current density could be due to the suppression of the HER. This must be verified by measurements of the gas phase composition via gas chromatography and the calculation of the faradaic efficiencies. Another reason could be different effective diffusion coefficients of carbon dioxide, the resulting reaction products and nitrogen in the porous system. This could be investigated by a variation of the pore diameter.

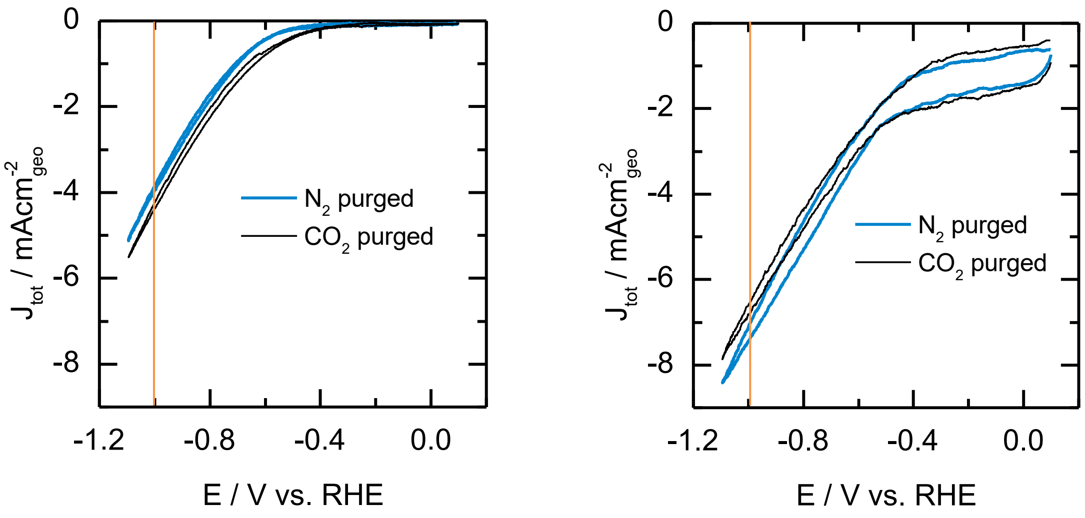

Figure 20: CV curves recorded in nitrogen (blue line) and carbon dioxide (black line) purged 0.1 M $KHCO_3$ electrolyte. Measurements for pristine copper plate (left) and CuF-SO4-15 (right). The orange line indicates the potential of -1.0 V vs. RHE used in the discussion.

The focus of investigation here will be the product analysis. Therefore, chronoamperometry measurements were done with CO_2 purged electrolyte for 1 h at -1.0 V vs. RHE. As mentioned before, the issue of iR compensation was completely neglected at this stage of the project. First of all, the current densities obtained by chronoamperometry are lower than the ones obtained by cyclic voltammetry (figure 21). While for the copper plate there is a difference between -4.5 mA/cm^2 in the CV compared to -1.8 mA/cm^2 in the chronoamperometrie, the copper foam catalyst differs from -6.8 mA/cm^2 in the CV to -6 mA/cm^2 in the chronoamperometrie. This means the current densities for the copper plate differs from 60 %, while for the copper foam catalyst the difference is about 12 %. Since the focus here is the application of the product analysis, this phenomenon will not be further discussed at this point. The current density difference will be discussed in a later discussion about the experimental protocol development.

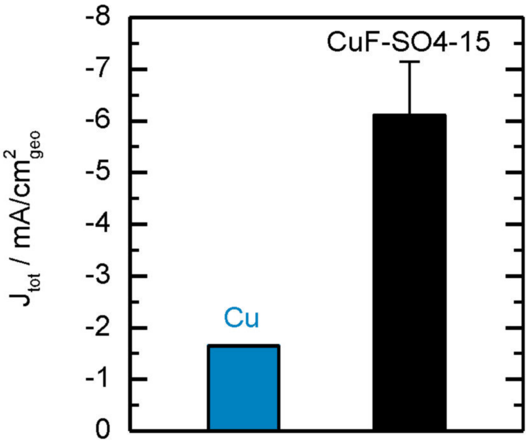

Figure 21: Mean current densities measured by chronoamperometry for Cu plate and CuF-SO4-15 at -1.0 V vs. RHE for 1h.

The gas phase was collected over the whole reaction time in a gas sampling bag and analyzed in the analytical group of Dr.-Ing. Alexander Schießer of the mass spectrometry team at the Technical University of Darmstadt via GC-MS. As seen in figure 22, no typical CO_2RR products could be detected. The only peaks observed are air (O_2. N_2) at 2.57 min and carbon dioxide at 7.95 min. Even the change to a 500 µl sample loop could not change the amount of detected components.

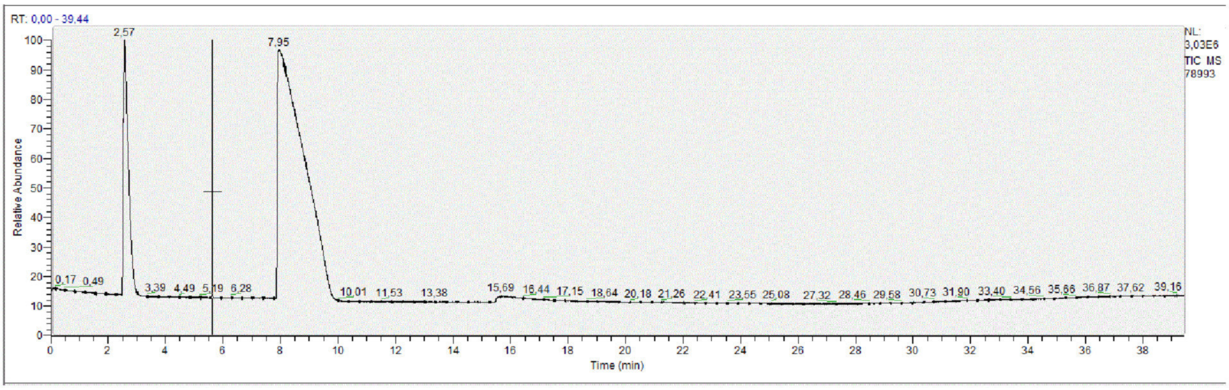

Figure 22: Offline gas chromatogram typically obtained for Cu and CuF-SO4-15 as catalyst at -1.0 V vs. RHE for 1h.

There are two problems concerning the gas phase analysis. The first one is the lack of detectable CO_2RR products or hydrogen and the second one is the strong peak for air. Both can be explained by sealing issues of the electrochemical cell. Leakage detection with argon by a leakage sensor showed, that it is difficult to seal the positions of the reference electrode and the clamp for the working electrode.

For the liquid phase analysis, dilution issues are a problem. As figure 23 shows, except of formate at 8.4 ppm, no other liquid product could be obtained. The explanation therefore is the high dilution of the liquid phase products due to the very large catholyte volume of 150 ml and the detection limit of the ^{1}H-NMR measurement.

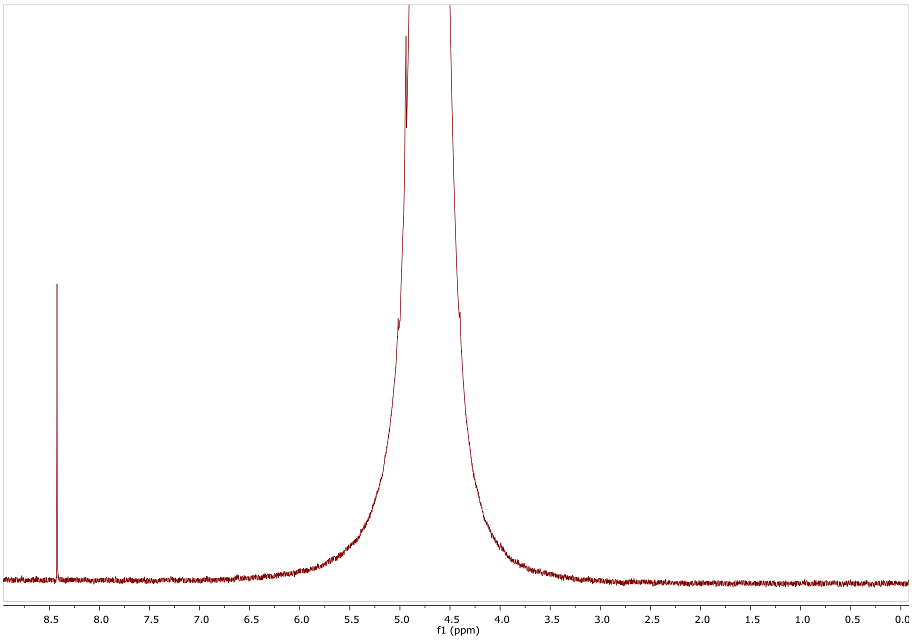

Figure 23: ^{1}H-NMR spectrum typically obtained for Cu and CuF-SO4-15 as catalyst at -1.0 V vs. RHE for 1h.

The analytical results show the main problem obtained with the H-type cell. It is only usable to measure current densities. As a conclusion here, a reactor design more efficiently to seal and with a lower electrolyte volume at the cathode is needed.

5.2.2. PMMA electrolyzer (2nd generation)

To overcome the problems that appeared with the H-type glass cell, an electrolyzer cell made from PMMA was developed. PMMA was chosen because of its transparency and the ability to see the gas evolution at the cathode. Sealing is much easier because of the modular system with screws. Leakage detection with argon by the leakage sensor verified a gas tight reactor system.

The first experiments done in the new reactor gave problems with the reduction current. The copper foam catalyst was tested for 2 h at -1.0 V vs. RHE. After about 6000 s. the measurement was interrupted by a current overload (figure 24). Restarting of the experiment with the same catalyst was not successful.

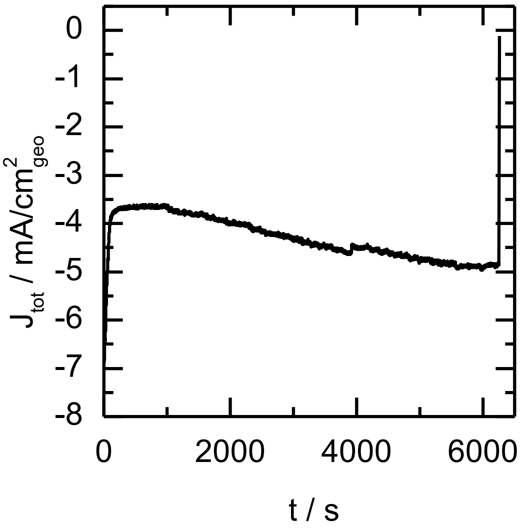

Figure 24: Chronoamperometry curve of CuF-SO4-15 with Nafion 117 membrane at -1.0 V vs. RHE.

The question here was about the reason for the interuption of the experiment. The hypothesis was a too high potential at the counter electrode, which exceeds the instrument limit. Therefore, the experiment was repeated at -0.7 V vs. RHE and with another potentiostat, the potential at the counter electrode was measured, depicted in figure 25. In case of Nafion 117 membrane, the counter electrode potential is dropping at the beginning from 5 V to about 3.7 V. Up to 800 s, the potential rises dramatically to about 4.9 V after 3600 s. An explanation therefore could be the problem of hydroxide ion exchange from the anolyte to the catholyte. During oxygen evolution reaction (OER) at the anode, hydroxide is formed. Since anionic species are not able to pass through Nafion 117 (cation exchange membrane), a capacitor like state will establish at the anodic half-cell. When the resulting potential is reaching the instrumental limit of the potentiostat, the experiment will be interrupted. To overcome this problem, the same measurement was done with an anion exchange membrane (Fumapem FAA-3-50). Instead of a potentiostat, a voltmeter was used to collect single points for the counterelectrode potential (figure 25). It can be seen, that the potential is constant over time when an anion exchange membrane is used.

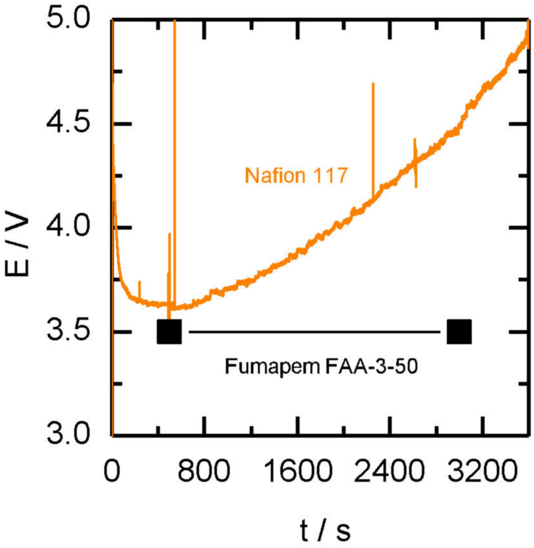

Figure 25: Counter electrode potential over time at -0.7 V vs. RHE.

The product analysis was also performed for the CuF-SO4-15 for 1 h of electrolysis time and using the Fumapem FAA-3-50 membrane. For the gas phase, still the detection of CO_2RR products is a big issue (figure 26). The chromatogram shows hydrogen at 0.17 min, carbon monoxide at 3.97 min and ethylene at 19.86 min, but also still a lot of air at 2.9 min (O_2) and 3 min (N_2). CO_2 is not visible anymore because it is bypassed to avoid blinding of the MS. The large amount of air must come from the sample preparation, since leakage test before verified a gas tight reactor set-up. The conclusion here is that the offline gas analytics does not fit the requirements of a proper CO_2RR experiment.

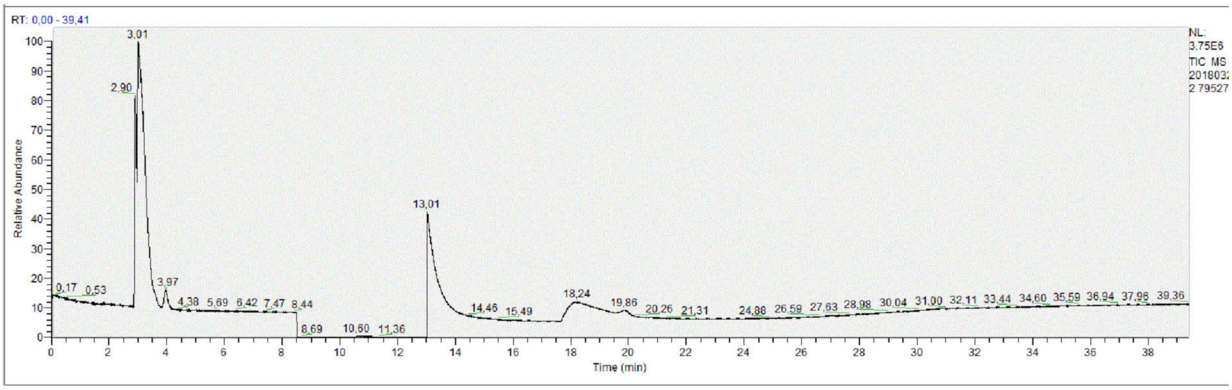

Figure 26: Offline gas chromatogram typically obtained for Cu and CuF-SO4-15 as catalyst at -0.7 V vs. RHE.

For the liquid phase products, formate, acetate and alcohols like ethanol and n-propanol could be detected, as seen in figure 27.

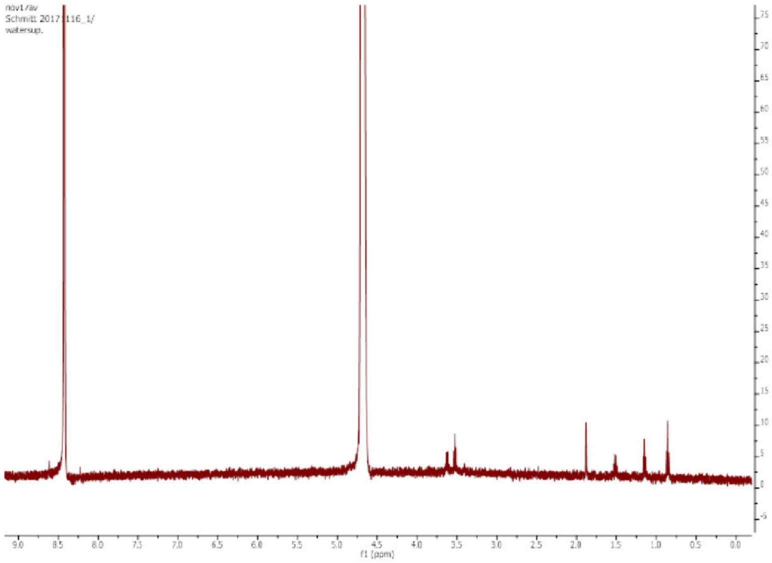

Figure 27: ^{1}H-NMR spectrum typically obtained for CuF-SO4-15 as catalyst at -0.7 V vs. RHE.

As a conclusion here, especially the gas phase analysis via offline GC-MS is difficult. The major problem here is the dominating concentration of air detected in all samples. The bottleneck is the injection procedure. Here, the sample loop cannot be evacuated or fully flushed with the sample. Therefore, the analytical system has to be switched to an online system, to overcome the air problem.

To rule out how the SCILL-catalysts influences the current density, the copper foam was modified by ionic liquid impregnation to have a pore filling degree of 10 %. The chronoamperometry curves are shown in figure 28.

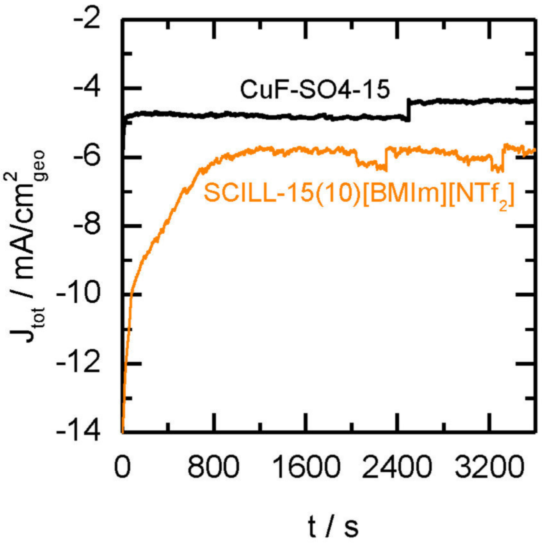

Figure 28: Chronoamperometry of unmodified and 10 % [BMIm][NTf$_2$] modified CuF-SO4-15 catalysts using Fumapem FAA-3-50 at -0.7 V vs. RHE.

The results show, that the current density could be increased from -4.5 mA/cm² for the unmodified copper foam catalyst to -6 mA/cm² for the SCILL-catalyst. This shows an impact of the SCILL catalyst on the current density. Since the analytical problem was not solved yet, the impact on product selectivity needs to be investigated later on. But a closer look to the chronoamperometry curve of the SCILL-catalyst shows an unexpected behavior. The curve shows two different slopes. The first sharp one during the first 100 s and the second less sharp one from 100 s to 800 s. After 800 s. steady state is reached. This indicates, that during the first 800 s. some faradaic processes occur. Since this phenomenon was further observed for the following measurements with fresh catalysts, independent of IL modification or not, the hypothesis here was poisoning of the catalyst by deposits on the reactor material. To get rid of impurities, the reactor was carefully cleaned with water and every metallic part avoidable was removed from the set-up. But the results did not change. The induction period was still seen. The conclusion out of this was, that the impurities penetrate the reactor material and therefore cannot be removed anymore. Cleaning the material with acid, organics or boiling could not be carried out since PMMA gets destroyed by these methods. Therefore, also the reactor material was an issue to be considered for the further development of the electrolysis set-up.

5.2.3. PEEK electrolyzer (3rd generation) and experimental protocol development

The new PEEK reactor was optimized regarding the issues observed in the reactors before. The reactor liquid phase volume was further reduced to 5 ml for cathodic half-cell and 8 ml for anodic half-cell in terms of increasing the concentration of products in the electrolyte. The anodic half-cell liquid volume was chosen higher to prevent potential capacitor effects like described in the section before. For the gas phase analysis, online GC was established to overcome the dilution problem by air. Furthermore, cleaning was much easier because PEEK can be boiled in water without any damage of the material to remove impurities. The counter electrode was also changed for two reasons. The first one is the OER activity. Ir-MMO is known to be very active in OER [119] and thus the anodic half-cell reaction will not limit the production rate at the cathodic half-cell. To avoid impurities in the electrolysis process, there was a switch from potassium bicarbonate to potassium carbonate as electrolyte. Potassium carbonate can be obtained in a much purer chemical grade (99.995 % for potassium carbonate against 99.95 % for potassium bicarbonate). By purging potassium carbonate with carbon dioxide, potassium bicarbonate was in-situ formed.

A further issue was still the membrane. The Fumapem FAA-3-50 is made for fuel cell applications and is described as non CO_2 stable, due to the formation of carbonates at the surface of the membrane. *Kuhl et al.* used Selemion AMV, another anion exchange membrane made for electrolysis applications in alkaline solutions [10]. To see the difference, CO_2RR experiments with analysis of the gas phase product composition were done using the Fumapem FAA-3-50 and Selemion AMV. In both cases, CuF-SO4-15 was used as working electrode in potassium carbonate as electrolyte for a reaction time over 1 h. The results are shown in figure 29. The hydrogen faradaic efficiency (FE) is in both cases around 90 %. An issue that has to be further dealt with. But by introducing the Selemion AMV instead of the Fumapem FAA-3-50, the FE of ethylene could be increased from below 0.5 % for the Fumapem FAA-3-50 to 3 % with the Selemion AMV. This result makes the Selemion AMV more interesting for further investigations and optimizations.

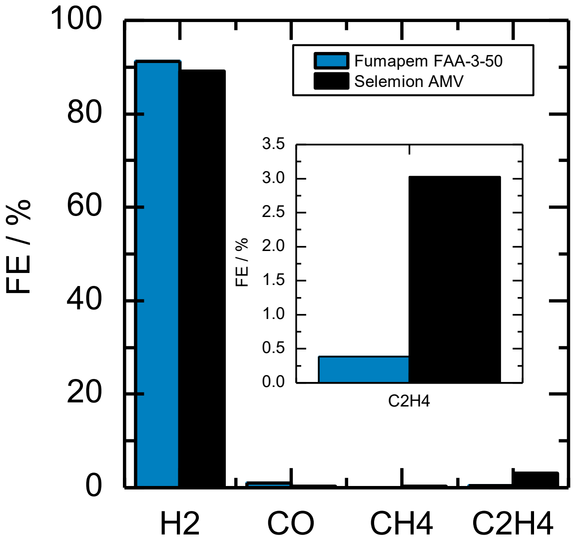

Figure 29: Faradaic efficiencies (FE) of gas phase products obtained during 1 h of electrolysis at -0.8 V vs. RHE for Fumapem FAA-3-50 (blue bars) and Selemion AMV (black bars).

The PEEK reactor used so far had the CO_2 inlet to the cathodic half-cell from the side. From an engineering point of view, the feed inlet position can influence the product selectivity. Reasons therefore are different fluid dynamic conditions and thus different residence times. Here, a complex mass transfer problem is given. At first, CO_2 from the gas phase needs to be dissolved in the aqueous electrolyte. Then, the dissolved CO_2 has to be transported to the catalyst and needs to pass the laminar boundary layer to the catalyst surface by diffusion. Since the turbulence of the electrolyte is induced by gas bubbles, all these effects are dependent from the gas dispersion.

Another possibility for the feed inlet is to set it to the bottom of the reactor, as shown in the experimental section.

In order to see the influence of the feed inlet to the reactor on the product selectivities, both reactors were used for the electrolysis of CO_2 for 1 h at -0.8 V vs. RHE (figure 30).

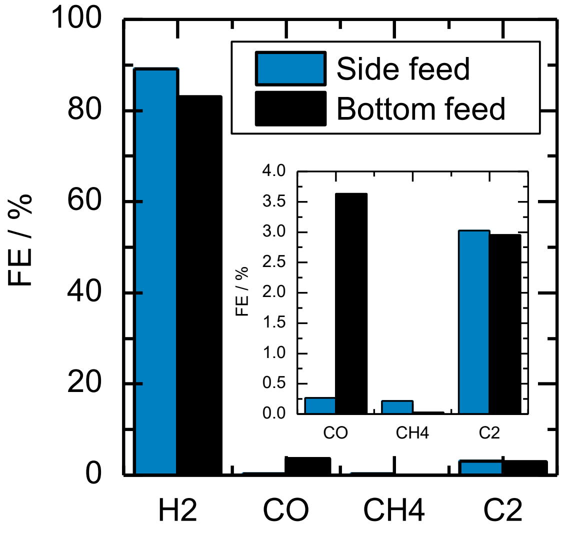

Figure 30: Faradaic efficiencies (FE) of gas phase products obtained during 1 h of electrolysis at -0.8 V vs. RHE for side inlet reactor (blue bars) and bottom inlet reactor (black bars).

Switching from the side feed to the bottom feed slightly decreases the FE of hydrogen from 90 % to 83 % FE. Although the feed inlet change shows the right direction of lowering the hydrogen amount, the high FE of hydrogen is still not satisfying. But the success had been the FE's of CO_2RR products. While for C_2 the FE's are not influenced, the FE of carbon monoxide could be dramatically increased from below 0.5 % to over 3.5 %. In figure 33, C_2 is compared instead of ethylene because the measurements for the side inlet reactor were made with another online-GC set-up than the ones for the bottom inlet reactor. For the side-inlet reactor, it is not clearly known if the ethylene peak is a composition of ethylene and ethane or not. Nonetheless, the results motivated to further use the bottom inlet reactor.

Since the high FE of hydrogen over 80 % is still an issue to be solved, the copper substrate purification was investigated. Therefore, the copper substrate was treated prior to the copper foam deposition process as described in the experimental section. This combined procedure of acidic cleaning steps removes metal impurities, which are well known to favor HER instead of CO_2RR. Gas phase FE's were calculated according to CO_2RR experiments with an untreated and a treated copper substrate, depicted in figure 31.

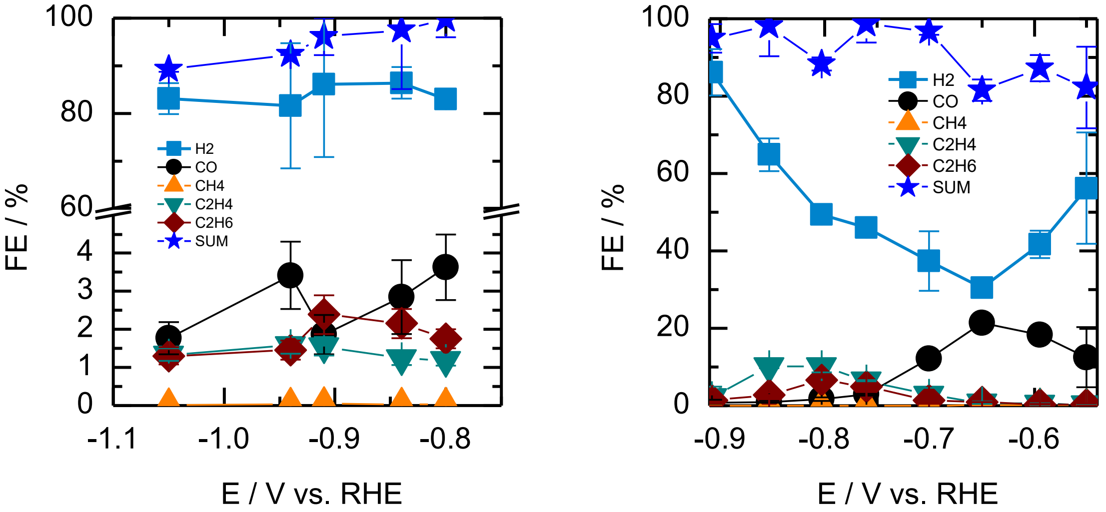

Figure 31: Gas phase faraday efficiencies for CuF-SO4-15 without (left) and with (right) pretreatment of copper substrate.

First of all, the sum of faradaic efficiencies is always between 80 and 100 %, which are typical values for CO_2RR. The deviation from 100 % can be due to measurement errors in current and especially in product FE because of the very low concentrations. The error in product analysis will be discussed later on. The tremendous improvement is the hydrogen FE dependence on the applied potential. While for the untreated copper substrate the FE is potential independent always over 80 %, pretreatment of the copper substrate leads to the typical U-shape profile known from literature. By pretreating the copper substrate, the FE of hydrogen could be lowered at -0.8 V vs. RHE from 83 % to about 50 %. The minimum FE could be reached at -0.65 V vs. RHE with about 30 %. But also the CO_2RR products could be significantly boosted. A closer look to ethylene and ethane shows, that pretreatment of the copper substrate could increase both FE's from about 1.5 to 2 % of maximum FE to about 7 to 10 % of maximum FE. Even more pronounced is the FE boosting of carbon monoxide, where the FE could be increased from about 3.5 % FE to a maximum of 20 % FE.

Among all the yet done optimization steps for the PEEK reactor, the copper substrate pretreatment has the biggest influence on product faradaic efficiencies.

All CO_2RR experiments were done at a CO_2 flow rate of 30 ml/min. This value was freely chosen without any hint to be the optimal flow rate. In the following section, the influence of the flow rate on CO_2RR gas phase product FE's will be further investigated. Therefore, the CO_2 flow rate was varied between 5 ml/min and 40 ml/min. The potential here was chosen as -0.85 V vs. RHE because the maximum of ethylene FE was reached at this potential in the section before. The influence of the CO_2 flow rate on the resulting total current density is depicted in figure 32.

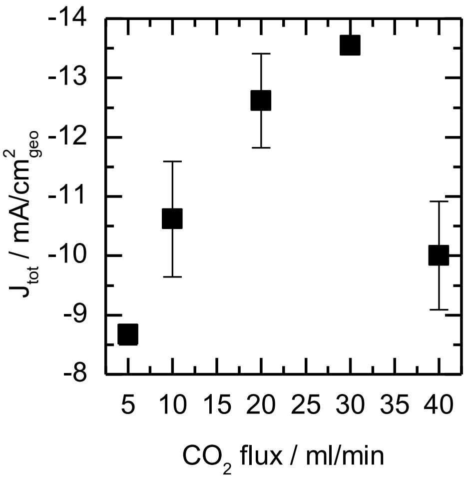

Figure 32: CO_2 flow rate dependent current densities at -0.85 V vs. RHE.

The current density is increasing from below -9 mA/cm² at 5 ml/min to -13.5 mA/cm² at 30 ml/min. The increase in the absolute of the current density from 5 ml/min to 30 ml/min can be explained by the increasing mixing of the electrolyte by forced convection. Here, the electrode boundary layer thickness is reduced and thus the CO_2 mass transport to the electrode surface is enhanced. The drop in current density from -13.5 mA/cm² at 30 ml/min to -10 mA/cm² at 40 ml/min is not as expected. One reason could be dry bubbles of hydrogen and CO_2RR products covering partially the catalyst surface. If mass transfer limitation is dominating, starting with 30 ml/min. at higher flow rates the maximum current density should be stable. To investigate the FE dependency from the CO_2 flow rate, the gas phase and liquid phase product analysis were done at different CO_2 flow rates (figure 33).

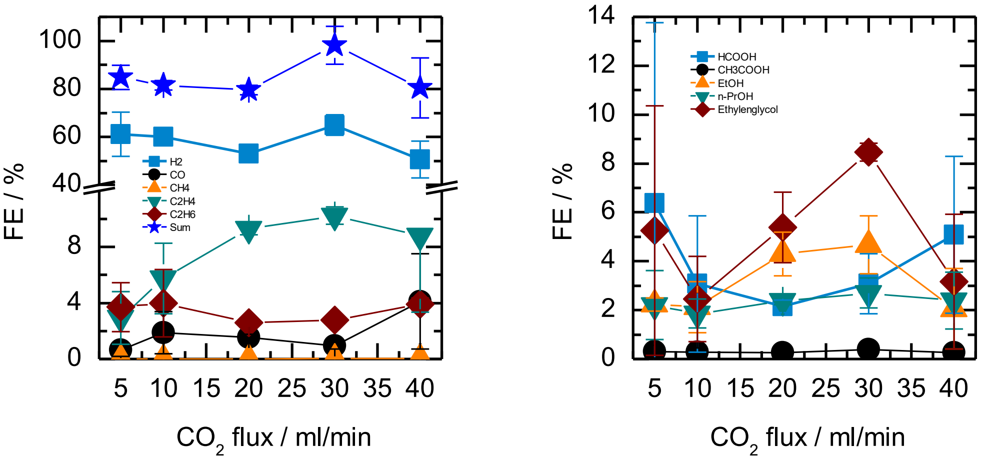

Figure 33: CO_2 flow rate dependent FE for gas phase (left) and liquid phase (right) at -0.85 V vs. RHE.

Obviously, the hydrogen faradaic efficiency is not strongly dependent on the CO_2 flow rate. The FE is always in the range between 60 and 50 %. Carbon monoxide and ethane are also not highly influenced by the CO_2 flow rate, whereas for ethylene, the FE is increasing from about 3 % at 5 ml/min to about 9 % at 20 ml/min. At higher flow rates of 30 and 40 ml/min, the ethylene FE is always in the range of 8 to 10 % FE. For the liquid phase products. acetic acid and n-propanol are not affected by the CO_2 flow rate. In case of formate the formate profile is u-shape like with its minimum of 2 % FE at 20 ml/min. Ethanol and ethylene glycol both have their maximum at 30 ml/min (4.5 % FE for ethanol and 9 % FE for ethylene glycol).

The results of the CO_2 flow rate variation show that 30 ml/min are suitable for the CO_2RR experiments with copper foam catalysts.

A closer look to the chronoamperometry curves shows an induction period for each measurement at the first seconds. If the current density at a defined potential obtained from the LSV is compared to the current density obtained by the chronoamperometry in steady state, the value is always lower for the chronoamperometry (figure 34). The difference here is between about -6 mA/cm^2 in the LSV and -1.3 mA/cm^2 in the chronoamperometry at -0.6 V vs. RHE. Two hypotheses can be stated as reason for this phenomenon. The first one is the formation of the electrochemical double layer in the chronoamperometry measurement. The second one is a really fast impoverishment of CO_2 in the solution. Therefore, with decreasing CO_2 amount at the electrode. the reduction current would drop.

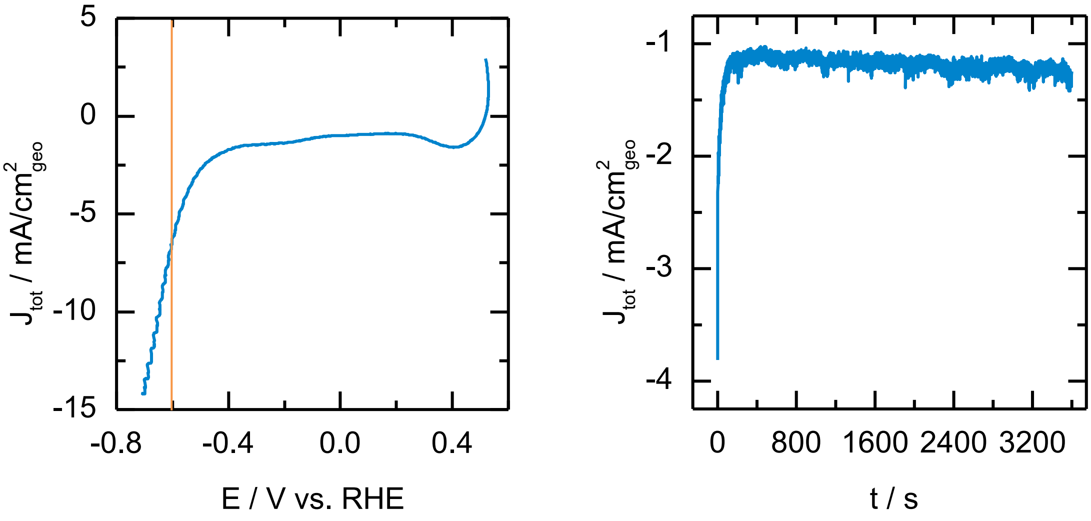

Figure 34: LSV curve (left) and chronoamperometry curve at -0.6 V vs. RHE (right) for CuF-SO4-15.

Since the LSV technique is a quite fast method, the potential was screend with staircase voltammetry (SCV). The experimental procedure was the following. Two experiments were done. the first with a sequence of an LSV directly followed by an chronoamperometry and the second one by an SCV followed by an chronoamperometry. The results and the potential screening procedure are shown in figure 35.

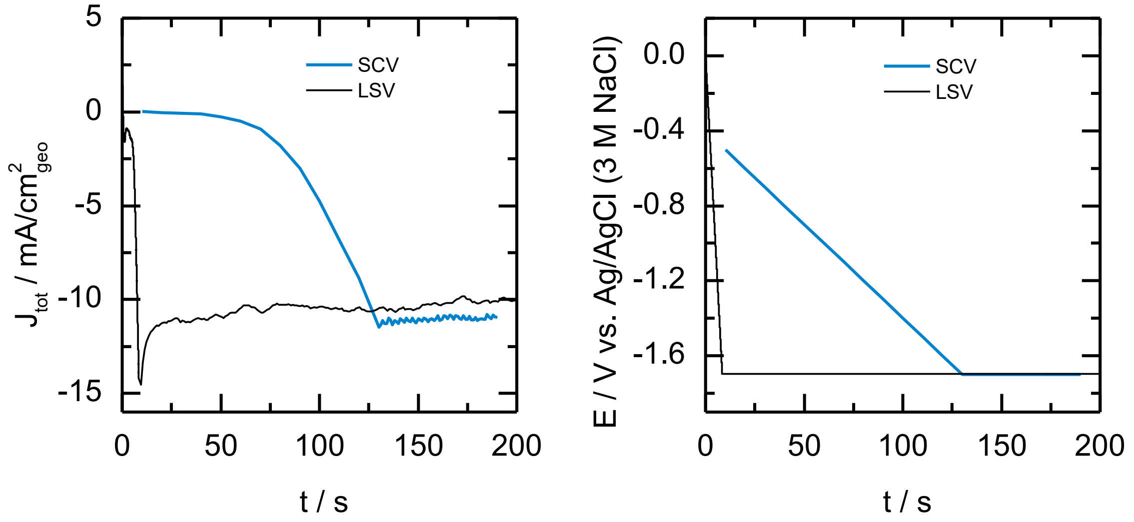

Figure 35: Combined experiments with LSV-chronoamperometry (black lines) and SCV-chronoamperometry (blue lines). Current densities over time (left) and potential program (right).

When the LSV technique is used prior to the chronoamperometry, the current denisty drop in the first seconds of the chronoamperometry is clearly seen. This could not be observed by using the SCV technique instead of the LSV technique. There, the current density of the chronoamperometry is directly in a stable state. This indicates, that the system needs some time for equilibration. Since the electrolyte is always purged with CO_2 for half an hour prior to the reduction experiments. It is highly likely that the development of the electrochemical double layer is the important factor. If the CO_2RR current densities in the steady state are compared to the SCV and LSV measurements, obviously the SCV current densities fit the CO_2RR experiments very well (figure 36).

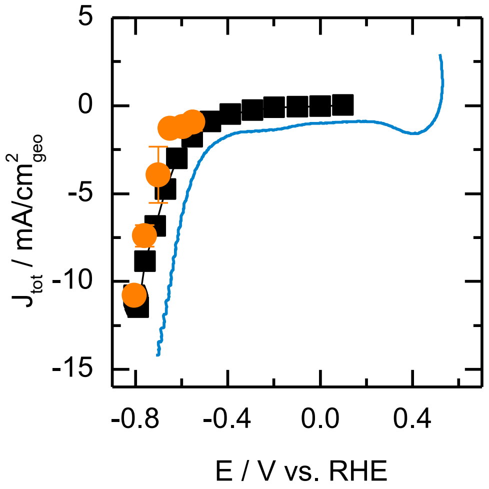

Figure 36: Comparison of total current densities by LSV (blue line). SCV (black line with squares) and chronoamperometry over 1h (orange dots).

A big issue in electrochemical CO_2 reduction is the establishment of the desired potential. It is crucial at this point to consider all the potential losses due to solution resistance or electrical resistances in the periphery. A major contribution is given by the solution resistance. Therefore, the desired potential must be iR corrected. This can be supported by an instrument function, as described in the experimental section. The experimental method to determine the solution resistance is the potentiostatic electrochemical impedance spectroscopy (PEIS). The problem for the copper foam catalyst was a very high scattering in the nyquist plot (figure 37).

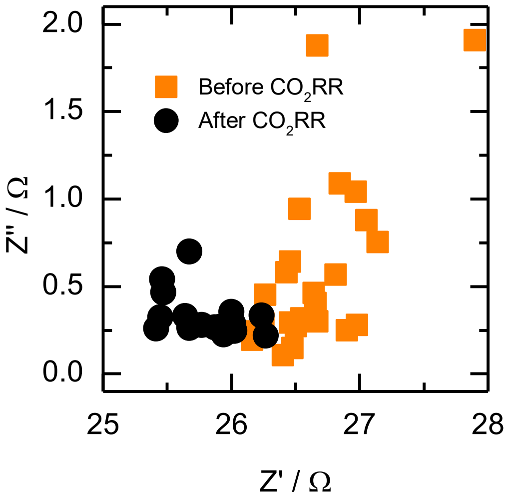

Figure 37: Nyquist plot for CuF-SO4-15.

The strong scattering depicted in figure 40 for the solution resistance is not usable for a proper iR correction of the applied potential. Since the strong scattering was observed at high starting frequencies (10000 Hz), the strating frequency was reduced to 100 Hz. Also the applied potential during the PEIS measurement was reduced from -1.7 V vs. Ag/AgCl to -1 V vs. Ag/AgCl. The intention there was to reduce the potential and therefore interference of gas evolution to the measurement. Since the potential was reduced, also the current range could be reduced from 200 mA to 20 mA and the electrometer mode was thus changed from differential to single ended. All these changes in the measurement procedure were successful to measure typical Nyquist-plots, as depicted in figure 38.

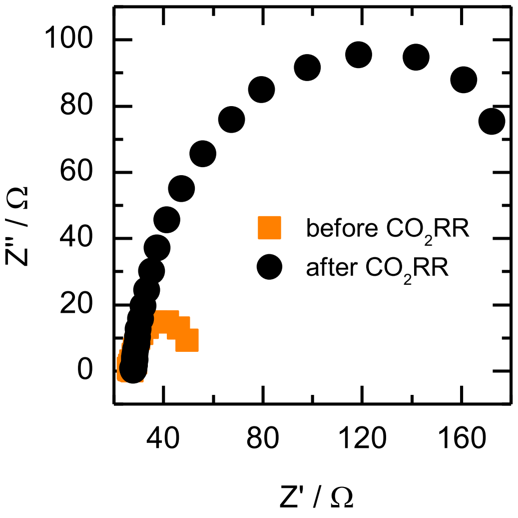

Figure 38: Optimized Nyquist plot for CuF-SO4-15.

The optimized nyquist plots can now be analyzed to determine the solution resistance. Therefore, the zero-crossing of the semi-circle with the Z' axis has to be determined. This can be done by fitting model nyquist plots from electrical equivalent circuits to the experimental data. Figure 39 shows the determined solution resistance values for three independent measurements with three CuF-SO4-15 catalysts before and after the CO_2RR experiments.

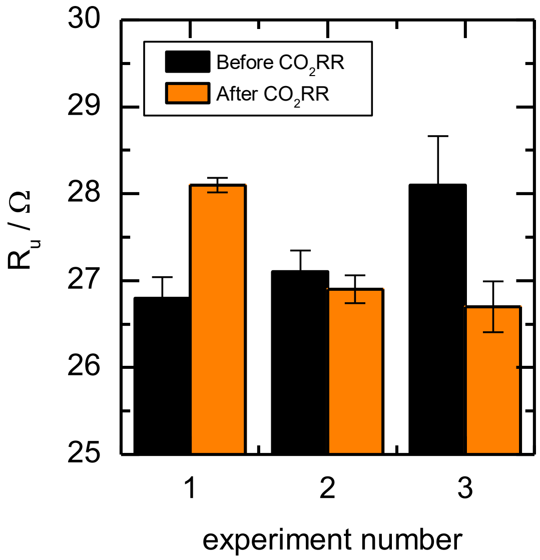

Figure 39: Determined solution resistance values R_u by PEIS before and after CO_2RR for CuF-SO4-15.

The results show that the resistance values before and after the CO_2RR experiment are different from experiment to experiment. While the resistance value before CO_2RR is in a range of about 26.8 Ω to 28 Ω, the resistance value after CO_2RR is in a range of 28 Ω to 26.5 Ω. Concerning the change in solution resistance during CO_2RR, no trend can be seen. While for experiment number one the value is rising, for the second experiment it is constant and for the third experiment it is dropping. As a conclusion, it is crucial to properly measure the solution resistance before each CO_2RR experiment.

With this information the deviation of the measured potential according to the applied potential can be determined, as depicted in figure 40. Therefore, the standard deviation of the iR corrected potential is shown in dependency of the current density. As expected, at high current densities, the standard deviation is the biggest. At -20 mA/cm², the error is about 5 %. Below -15 mA/cm², the error is below 1 %. Comparing this result to the solution resistance analysis, it gets clear that the measurement error in current density is more significant than the error coming from the solution resistance determination.

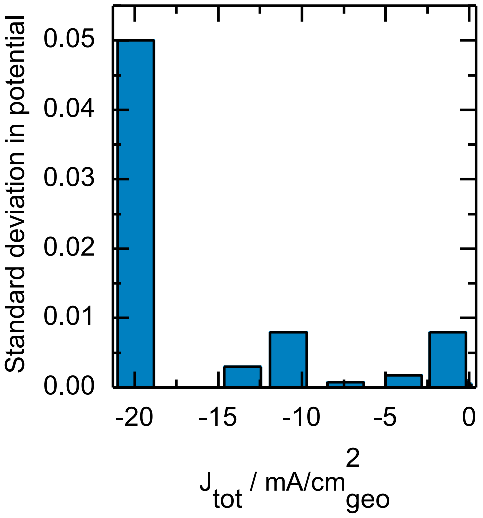

Figure 40: Standard deviation of the potential in dependency of the total current density for CuF-SO4-15.

5.2.4. Uncertainty of gas phase product analysis

Since the concentration range in CO_2RR is in the ppm area, it is crucial to investigate the deviation of the faradaic efficiency over time. Therefore, CO_2RR on CuF-SO4-15 was done for 1 h at -0.85 V vs. RHE by taking gas phase sample every 13 minutes via online GC. As figure 41 shows for the most significant gas phase products hydrogen and ethylene, the faradaic efficiency over time is quite stable. The deviation for hydrogen is bigger than for ethylene. In order to get better statistical mean values of the current density, the FE will be calculated by taking the single point FE's over time of three reproduced experiments and calculate the mean value out of the whole data set.

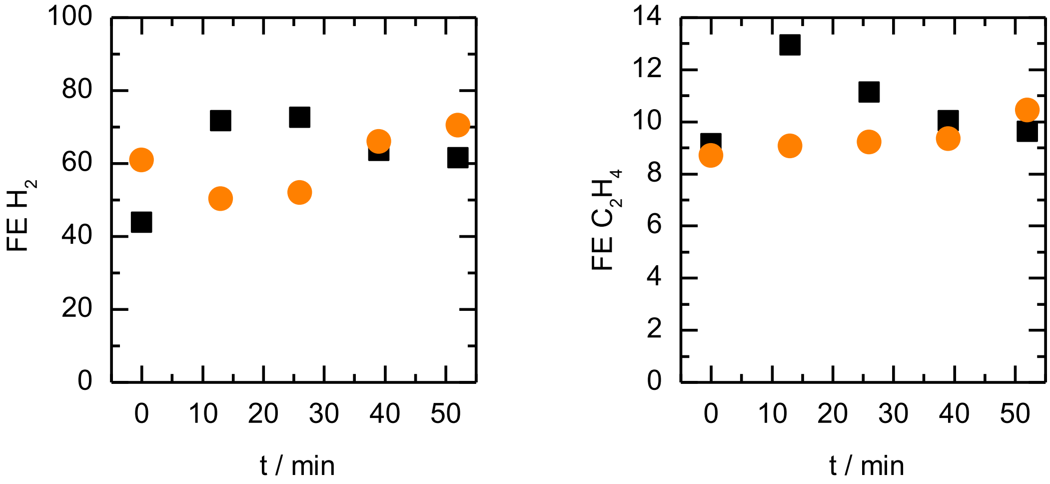

Figure 41: Faradaic efficiency over time measured by online GC with CuF-SO4-15 for 1 h at -0.85 V vs. RHE. Black squares and orange dots show reproduced experiments.

5.3. Copper foam catalyst activities in CO_2RR

For the following measurments, the final experimental protocol and the reactor from generation three were used.

5.3.1. Coulombs controlled deposition time synthesis

In order to investigate the influence of different deposition times on CO_2RR activity, chronoamperometry measurements were done over 1 h of reaction time. The first variable to be compared is the current density at different potentials, depicted in figure 42.

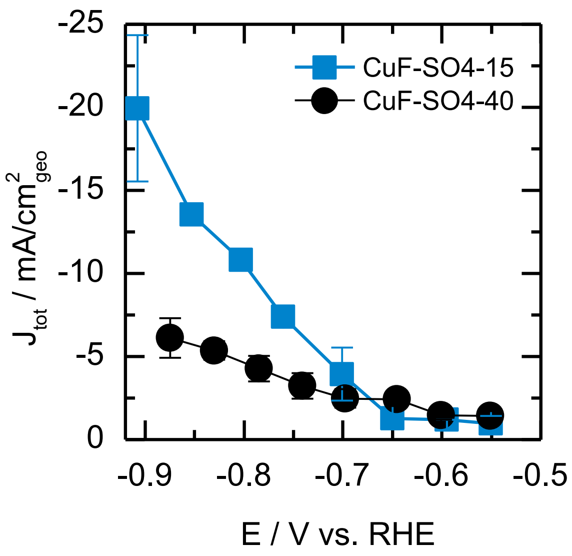

Figure 42: Current density at different potentials for CuF-SO4-15 (blue squares) and CuF-SO4-40 (black dots).

Obviously, the current density did not differ for both samples below -0.7 V vs. RHE. At more negative potentials, the current density has a much higher slope for the CuF-SO4-15 catalyst compared to the CuF-SO4-40 catalyst. At around -0.9 V vs. RHE, CuF-SO4-15 reached a current density of -20 mA/cm^2, while CuF-SO4-40 reached -6 mA/cm^2. Since CuF-SO4-40 had a higher roughness factor than CuF-SO4-15 (see chapter 5.1.1), the CuF-SO4-40 catalyst led to a stronger diffusion limited reaction. A closer look to the gas phase products (figure 43) shows, that hydrogen faradaic efficiency was boosted by increasing the deposition time. This increase goes from 30 % FE at -0.65 V vs. RHE for CuF-SO4-15 to 50 % FE at -0.75 V vs. RHE for CuF-SO4-40. This boosting in HER can be explained by the less sluggish kinetics of HER compared to CO_2RR and the roughness factor of CuF-SO4-40. In case of CuF-SO4-40, all CO_2RR products are suppressed in their faradaic efficiency compared to CuF-SO4-15. The maximum of carbon monoxide was shifted to higher overpotentials from -0.65 V vs. RHE for CuF-SO4-15 to -0.7 V vs. RHE for CuF-SO4-40. Here, the faradaic efficiency dropped from 20 % for CuF-SO4-15 to 10 % FE for CuF-SO4-40. This trend is also seen for ethylene and ethane. For ethylene, the faradaic efficiency dropped from 10 % at CuF-SO4-15 to 4 % at CuF-SO4-40.

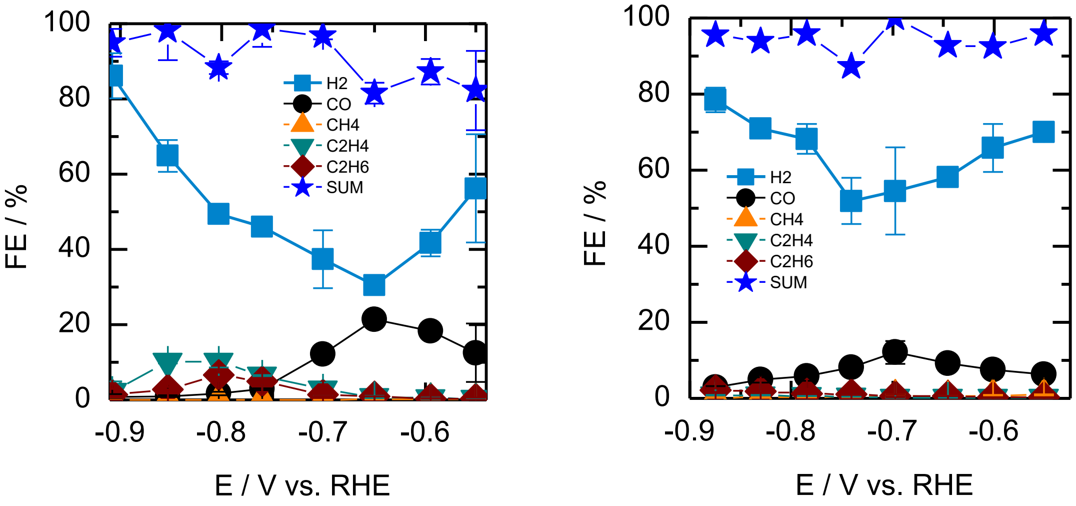

Figure 43: Gas phase products faradaic efficiencies for CuF-SO4-15 (left) and CuF-SO4-40 (right).

Figure 44 depicts the situation for the liquid phase. The faradaic efficiency of ethylene glycol was not affected by increasing deposition time. The maximum FE of 25 % is achieved with both catalysts at -0.7 V vs. RHE. In case of formate, the faradaic efficiency was decreased by increasing deposition time from about 15 % FE to about 7 % FE at -0.7 V vs. RHE. If the alcoholic species ethanol and n-propanol are compared, it seems like the formation of the latter ones were nearly suppressed.

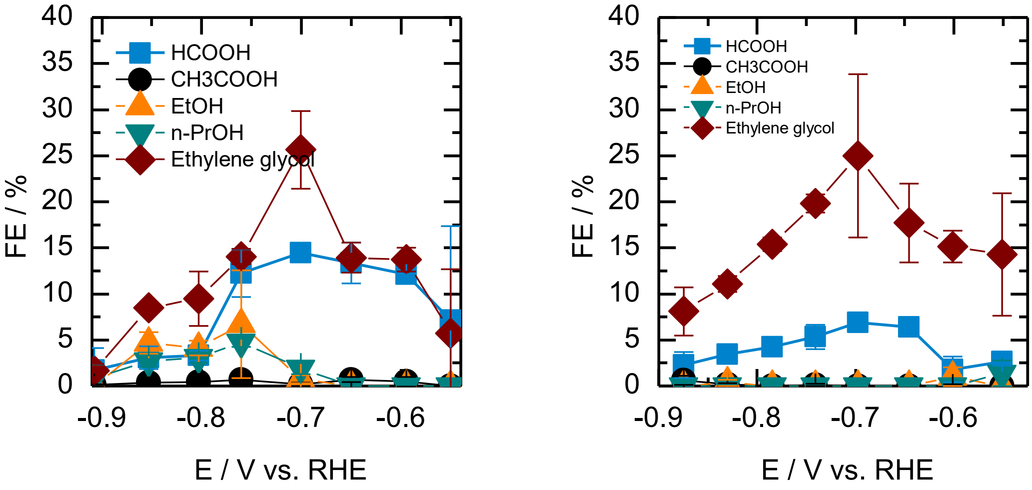

Figure 44: Liquid phase products faradaic efficiencies for CuF-SO4-15 (left) and CuF-SO4-40 (right).

For the CuF-SO4-60 catalyst, no stable currents could be achieved over time, independently from the applied potential (figure 45). Therefore, also no product analysis was done. The instability of current could be due to the instability of the CuF-SO4-60 catalyst. When opening the reactor after the electrolysis, copper foam deposits could be seen at the bottom of the reactor and at the membrane.

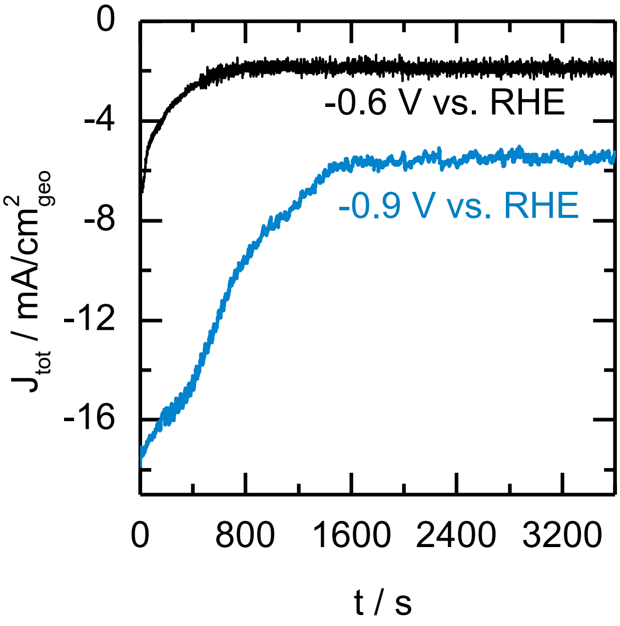

Figure 45: Chronoamperometry curves for copper foam catalyst CuF-SO4-60 at two different potentials.

To conclude the deposition time variation, increasing the deposition time at first led to lower faradaic efficiencies of CO_2RR products in almost all cases besides a boosting of HER. The reason for this could be stronger diffusion limitation as discussed before. Since increasing the deposition time changed more than one catalyst parameter (see chapter 5.1.1.), it is hard to determine the most dominant parameter. Due to instability issues at even higher deposition times, the deposition time variation is limited for practical uses.

5.3.2. Synthesis controlled by forced convection

In order to investigate the influence of one single catalyst parameter, the copper foam materials discussed in chapter 5.1.2 were used as catalysts. Here, the influence of the surface pore size to CO_2RR selectivity was investigated. In the following discussion, the samples are labeled by the mean surface pore diameter according to the investigations in chapter 5.1.2 instead of the applied stirring speed. The results for the current densities are given in figure 46.

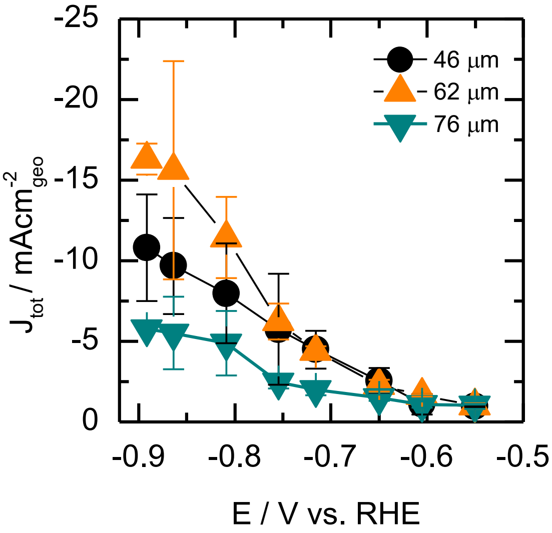

Figure 46: Current densities at different potentials for different surface pore diameters. 46 µm (black dots), 62 µm (orange triangles) and 76 µm (green triangles).

By increasing the surface pore diameter from 46 µm to 62 µm, the current density was comparable till -0.75 V vs. RHE. At more negative potentials, the slope for the current density curve was higher for 62 µm compared to 46 µm. Further increasing the surface pore diameter to 76 µm decreased the total current density in the range of -0.65 V vs. RHE to -0.9 V vs. RHE. At more positive values than -0.65 V vs. RHE, the current densities were comparable for all surface pore diameters. Thus, especially at more negative potentials, the surface pore diameter influences the total current density.

Regarding the liquid phase products, especially the alcohol formation was influenced by the surface pore diameter (figure 47). Ethanol formation was favored in case of 46 µm. There, the maximum FE was reached with 14 % at -0.75 V vs. RHE. Increasing the surface pore diameter to 62 µm decreased the ethanol FE to a maximum of 1.5 %. At 76 µm, the maximum amount of ethanol was reached at -0.55 V vs. RHE (8 % FE). Higher overpotentials decreased the FE dramatically to less than 2 % FE. Ethanol formation can eighter proceeds via a dimerization step of adsorbed CO (pathway I) or the dimerization of two adsorbed carbene species (pathway II). The adsorbed carbene species are formed out of adsorbed CO according to the mechanism described in chapter 2 [47]. Increasing the surface pore diameter could increase the distance of two adsorbed CO intermediates. This favors pathway II, which is also the pathway for the formation of n-propanol. This is in agreement with the fact, that n-propanol was boosted by 62 µm surface pore diameter compared to 46 µm surface pore diameter. At -0.7 V vs. RHE, 62 µm catalyst was able to reach nearly 20 % FE of n-propanol. For 46 µm, 11 % FE could be reached at -0.75 V vs. RHE and for 76 µm. 10 % FE were reached at -0.85 V vs. RHE.

As a conclusion, increasing the surface pore diameter from 46 µm to 62 µm could lead to a change in the favored pathway for ethanol formation from pathway I to pathway II. The latter one leads to a competition between ethanol and n-propanol formation, which explains the decrease of ethanol FE while increasing the n-propanol FE at the same time. The fact, that further increasing the surface pore diameter to 76 µm increases the ethanol FE and decreases the n-propanol FE cannot be explained with the given results. Here, deeper investigations have to be done to fully understand the surface pore diameter influence on the different reaction pathways.

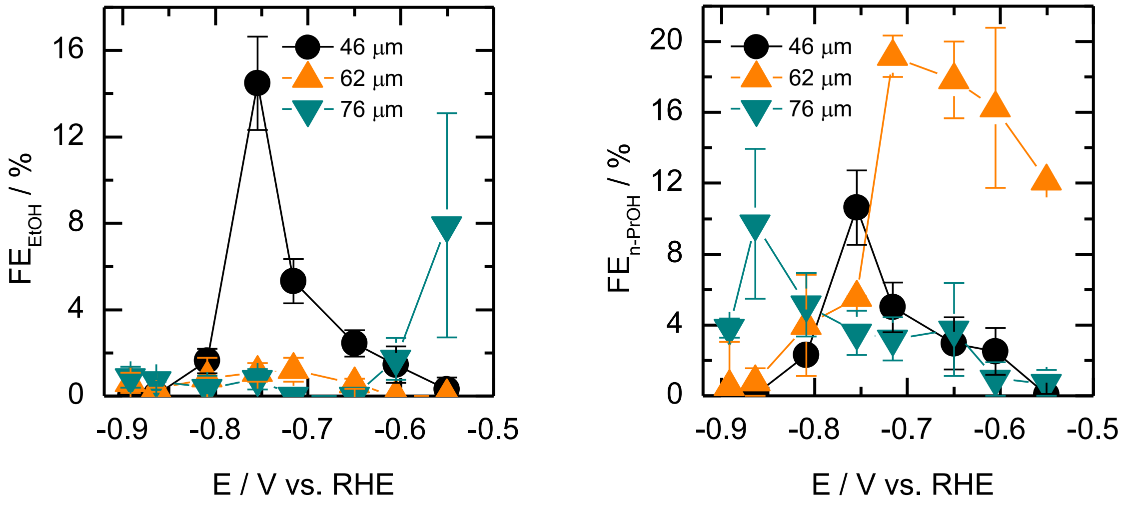

Figure 47: Faradaic efficiencies for ethanol (left) and n-propanol (right) at different potentials for different surface pore diameters. 46 µm (black dots), 62 µm (orange triangles) and 76 µm (green triangles).

For ethylene glycol (figure 48), increasing the surface pore diameter suppressed the formation of the latter one. This is the same behavior that could be observed for the formation of ethanol. From 46 µm to 62 µm, the faradaic efficiency was dropping from a maximum of 16 % at -0.65 V vs. RHE to a maximum of 10 % FE at -0.6 V vs. RHE. Further increasing the surface pore diameter to 76 µm decreased the FE to a maximum of 3 % at -0.85 V vs. RHE. As *Kuhl et al.* [10] suggested, the formation of ethylene glycol could be coupled to the formation of ethylene glycol. There, the formation of ethanol out of adsorbed ethylene glycol intermediate is discussed as one possibility. As a conclusion out of the results, the formation of ethylene glycol could at least be preceded via pathway I or a similar pathway.

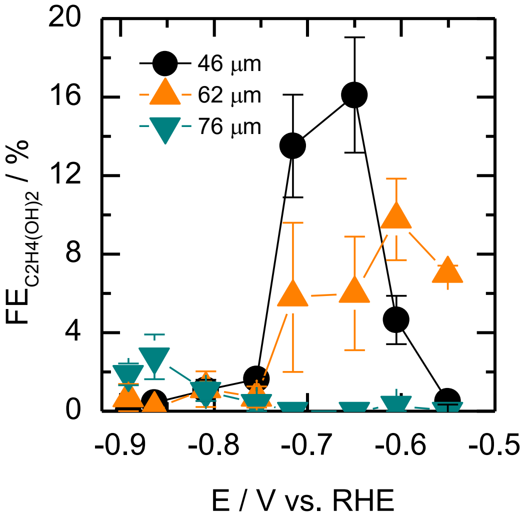

Figure 48: Faradaic efficiency for ethylene glycol at different potentials for different surface pore diameters. 46 µm (black dots), 62 µm (orange triangles) and 76 µm (green triangles).

The results for the liquid phase show, that the surface pore diameter influences the liquid phase product formation, especially the formation of alcohols. Figure 49 shows the influence on the gas phase products.

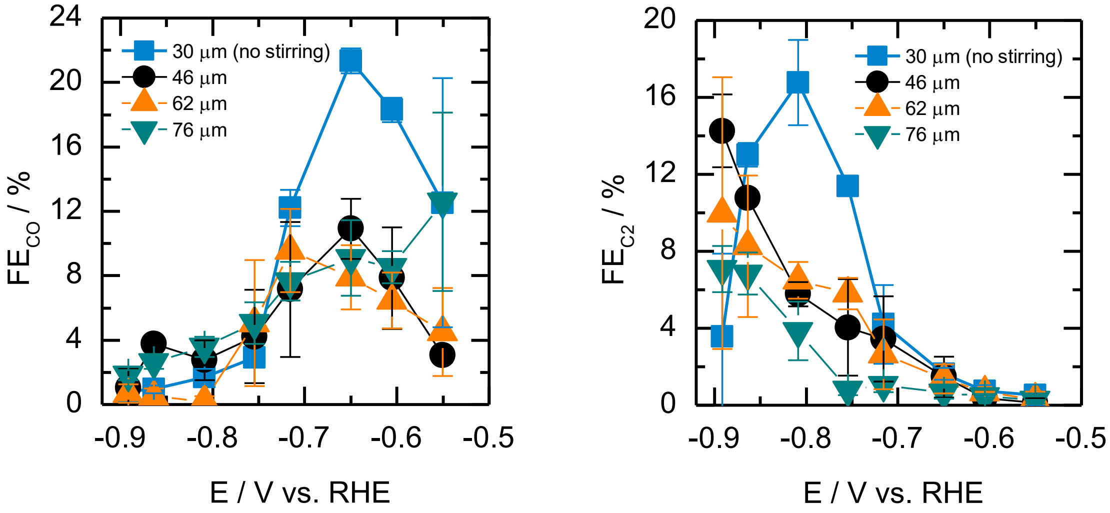

Figure 49: Faradaic efficiencies for CO (left) and the sum of ethylene and ethane, combined to C_2 (right), at different potentials for different surface pore diameters. 46 µm (black dots), 62 µm (orange triangles) and 76 µm (green triangles).

Increasing the surface pore diameter from 46 µm to 62 µm and further to 76 µm did not influence the gas phase faradaic efficiencies. At all potentials, the values were in a comparable range. Comparing the FE's for the catalysts synthesized by forced convection with the catalysts synthesized without forced convection, strong differences were observed. In the following, the CuF-SO4-15 catalysts described in chapter 5.1.1 will be labeled by its surface pore diameter. At 30 µm, the maximum FE of carbon monoxide was 21 %, while applying forced convection led to suppression to 11 %. Here, the residence time of the adsorbed CO intermediate seemed to be increased by increasing surface pore diameter of the copper foam catalyst. Taking into account the results for the liquid phase products, adsorbed CO intermediate is a key intermediate for the alcohol formation, which is increased by applying the catalysts synthesized by the forced convection approach. If the increased residence time is due to structural or electronic effects cannot be cleared out by the given results and needs further investigations.

In case of the total C_2 FE, the maximum for 30 µm was achieved with 17 % at -0.8 V vs. RHE. In the range of -0.5 V vs. RHE to -0.9 V vs. RHE, the maximum was still not reached. According to the trend, the forced convection approach shifted the C_2 maximum to potentials more negative than -0.9 V vs. RHE. Also here it cannot clearly be deduced out, if the overpotential increasing for C_2 gas phase product formation is of structural or electronic nature. Deeper investigations on the understanding of the influence of the forced convection approach catalyst synthesis on the reaction pathways for C_2 gas phase products have to be done. Furthermore, the formation of C_2 gas phase products has to be deeper investigated by screening higher overpotentials, to deduce out the maximum FE's of ethylene and ethane. Nontheless, the results underline the strong influence of the forced convection approach to the gas phase faradaic efficiencies.

All in all, at the screened potential range, the use of copper foam catalysts synthesized by the forced convection approach pronounces a preferred synthesis of liquid phase products in comparison to gas phase products. This underlines the possibility of influencing reaction pathways and thus selectivities by controlling the design of copper foam catalysts.

5.4. Chemical modification of catalyst with ionic liquid

5.4.1. IL impregnation of copper foam catalysts

To apply the SCILL concept to copper foam catalysts, the method described in the experimental section was used. Here, the catalyst was modified by impregnation with an ionic liquid/organic solvent mixture. SEM investigations should clarify the IL distribution in the materials pores, depicted in figure 50. IL impregnated catalysts were labeled according to the description in the experimental section.

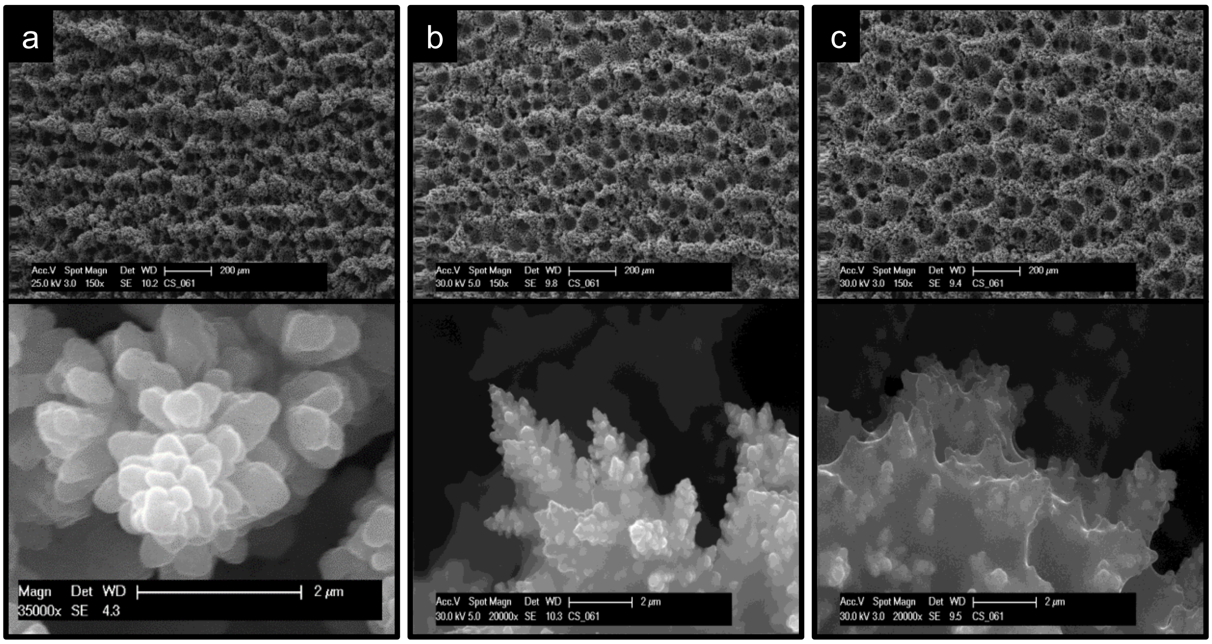

Figure 50: SEM images of CuF-SO4-15 (a), SCILL-15(5)[BMIm][NTf$_2$] (b) and SCILL-15(10)[BMIm][NTf$_2$] (c). Synthesis at 12 V and 10 A.

According to the SEM investigations, IL impregnation does not affect the overall morphology of the porous material. The IL is covering the crystallites of the copper foam, which validates the used impregnation method.

With energy dispersive X-ray spectroscopic (EDS), the spatial distribution of IL phase on the Cu-form materials were investigated., Therefore, elemental mappings analyses on the IL-modified Cu-Foam materials was performed, as illustrated in figure 51. The analysis of fluorine and sulfur showed no local aggregation in the macropores of the material. This proofs, that [BMIM][NTF$_2$] is homogenously distributed on the copper foam material.

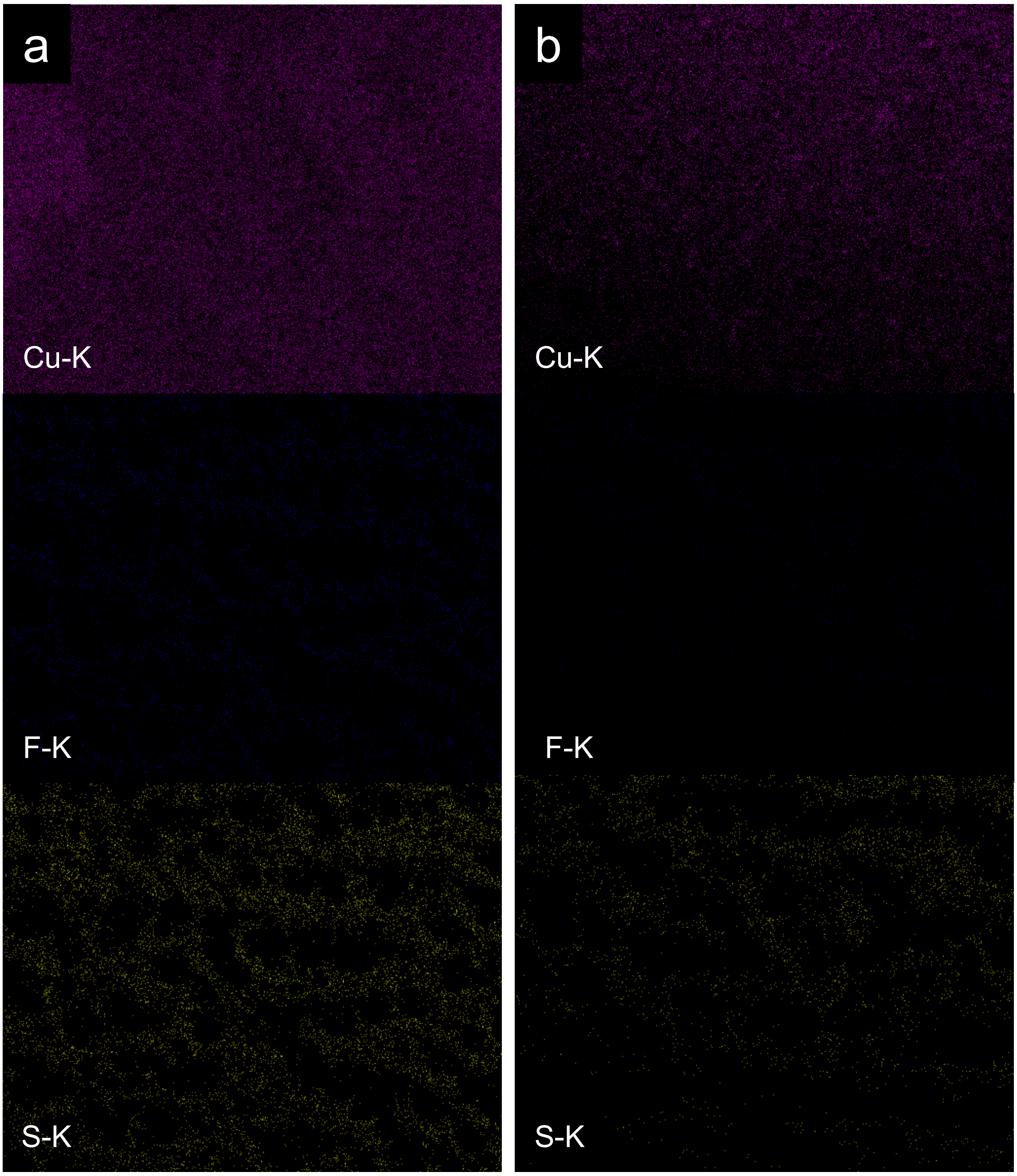

Figure 51: EDS elemental mapping images of SCILL-15(5)[BMIm][NTf2] (a) and SCILL-15(10)[BMIm][NTf2] (b) showing the EDS signals of Cu, F and S.

Furthermore, X-ray photoelectron spectroscopy (XPS) was used to analyse a possible impact of the IL modification on the electronic structure of the copper foam surface. As indicated in figure 52, no shift in the $Cu_{2p1/2}$ or $Cu_{2p3/2}$ could be observed. Therefore, the IL modification did not influence the electronic structure of the copper surface. As a conclusion, the IL must act as a ligand on the copper foam material.

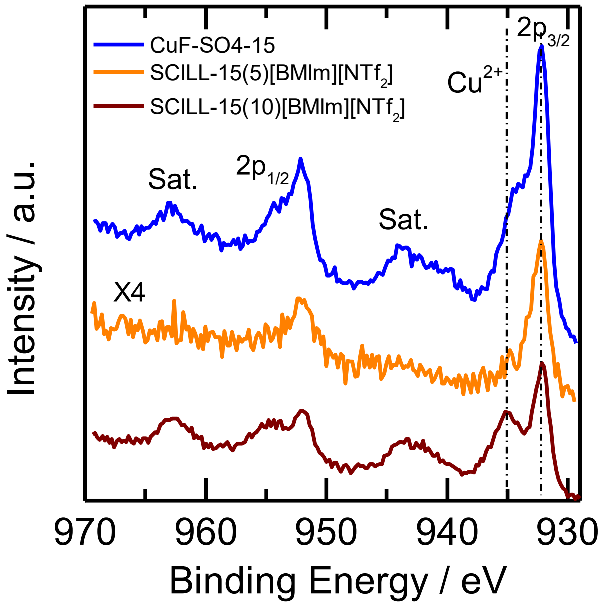

Figure 52: XPS of pristine and IL impregnated copper foam catalysts for CuF-SO4-15 (blue line), SCILL-15(5)[BMIm][NTf$_2$] (orange line) and SCILL-15(10)[BMIm][NTf$_2$] (brown line).

The roughness factors of the IL impregnated copper foams were determined by measuring the ECAS with the methyl viologen method (figure 53).

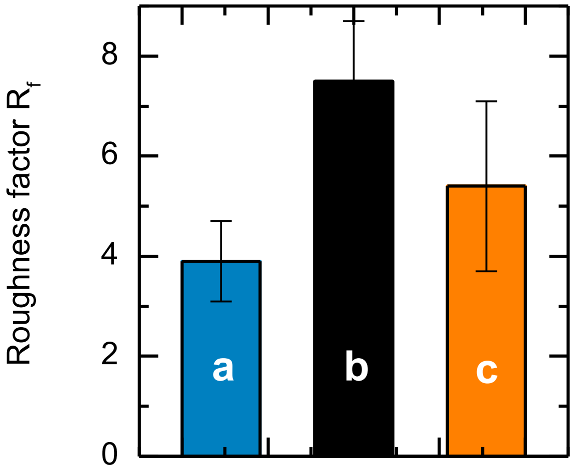

Figure 53: Roughness factors for CuF-SO4-15 (a), SCILL-15(5)[BMIm][NTf$_2$] (b) and SCILL-15(10)[BMIm][NTf$_2$] (c).

The roughness factor nearly doubled by applying a pore filling degree of 5 v-% with [BMIm][NTf$_2$] from 4 to 7.5. This could be an indicator of increased mass transfer for the probe molecule DMVCl$_2$ to the electrode surface. By further increasing the loading to 10 v-%, the roughness factor decreased to about 5.7. Here, the viscosity of the ionic liquid could cause mass transfer problems for the probe molecule.

5.4.2. Influence of ionic liquid modification on electrochemical reduction of CO$_2$

Figure 54 compares the overall current densities of the pristine copper foam CuF-SO4-15 to the IL impregnated one with 5 v-% IL loading obtained from the chronoamperometry measurements at different potentials. It can be seen, that the current densities were not differing with IL modification. This indicates that the mass transport resistance is not increased by the IL.

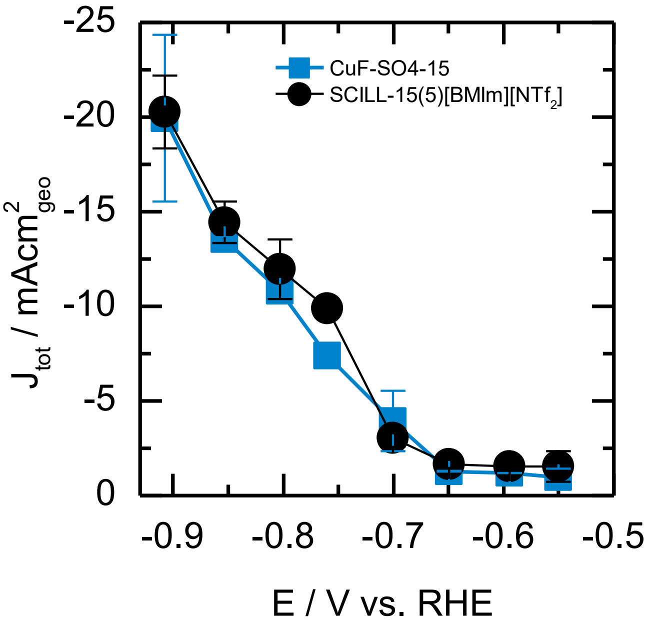

Figure 54: Current densities at various potentials for CuF-SO4-15 (blue squares) and SCILL-15(5)[BMIm][NTf$_2$] (black dots).

The FE's of the gas phase products on the pristine and the IL-modified copper foam catalysts were investigated at first. Obviously, the competing hydrogen evolution reaction is still dominating the product spectra. The FE's are ranging from 30 % to 86 % for the pristine copper foam and from 36 % to 85 % for the IL impregnated copper foam catalyst (figure 55). The comparison of the minimum FE values of the pristine and the IL impregnated copper foam catalysts figured out a slightly boosting of the hydrogen evolution reaction by IL modification. This differs from the expectations, that the IL could suppress the HER due to its hydrophobicity. Here, the [BMim]-cation must act as proton source due to the acidity of its C2-position, as reported by *Min et al.* [120]. *Zhang et al.* could observe a good proton conductivity for Pt catalysts on hydrogen evolution reaction with [BMIm][NTf_2] [59]. In this studies, the HER was not suppressed by IL modification of the catalyst. Therefore, modification of the C2 position of the imidazole cation is needed to suppress the HER during CO_2RR.

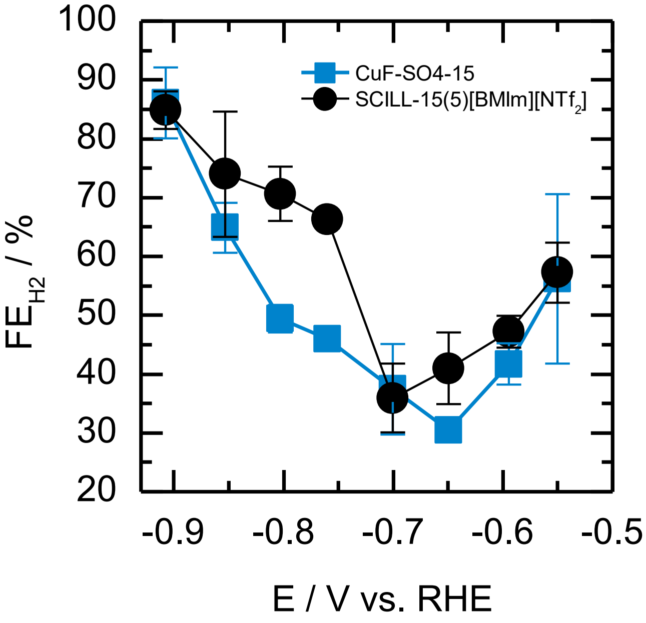

Figure 55: Hydrogen FE at different potentials for CuF-SO4-15 (blue squares) and SCILL-15(5)[BMIm][NTf_2] (black dots).

As figure 56 shows, the FE results for the major gas phase products CO, methane and ethylene were not influenced by IL modification. In the high overpotential region (< -0.7 V vs. RHE) the maximum FE of ethylene was suppressed from 10.2 % to 5.2 % after the IL modification, while at the same time, no difference for ethylene FE's could be ruled out in the low overpotential region (> -0.7 V vs. RHE)

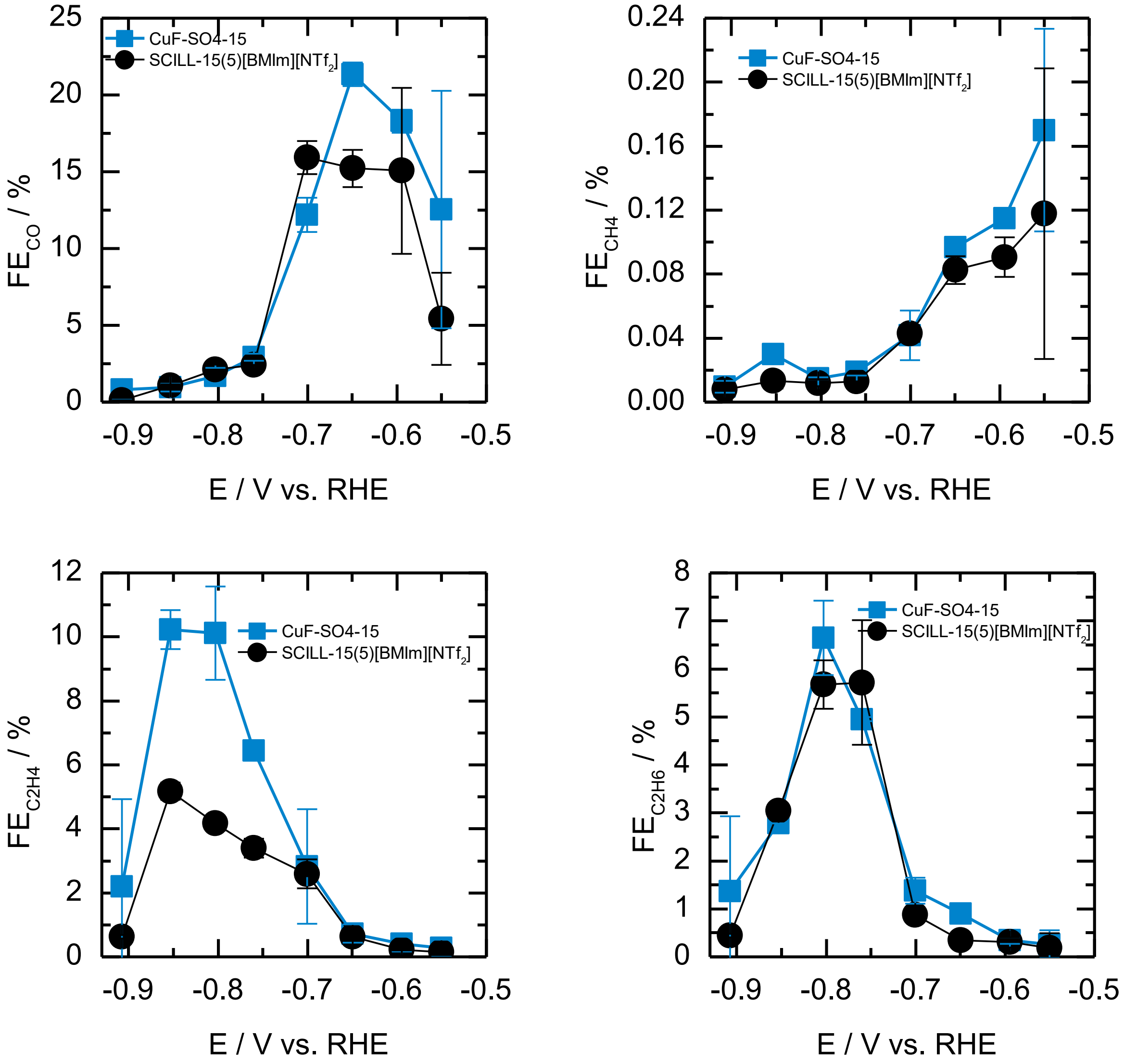

Figure 56: FE's for gas phase products CO, CH_4, C_2H_4 and C_2H_6 at different potentials for CuF-SO4-15 (blue squares) and SCILL-15(5)[BMIm][NTf$_2$] (black dots).

In contrast, minor differences in the FE's for the liquid phase products ethylene glycol and formate could be observed at around -0.7 V vs. RHE, illustrated in figure 57. At this potential, no strongly absorbed CO intermediate at the copper surface was supposed. The most dominant effect of IL modification is the suppression of ethanol and n-propanol in the liquid phase, while the pristine copper foam catalyst obtains maxima of 7 % for ethanol and 5 % for n-propanol.

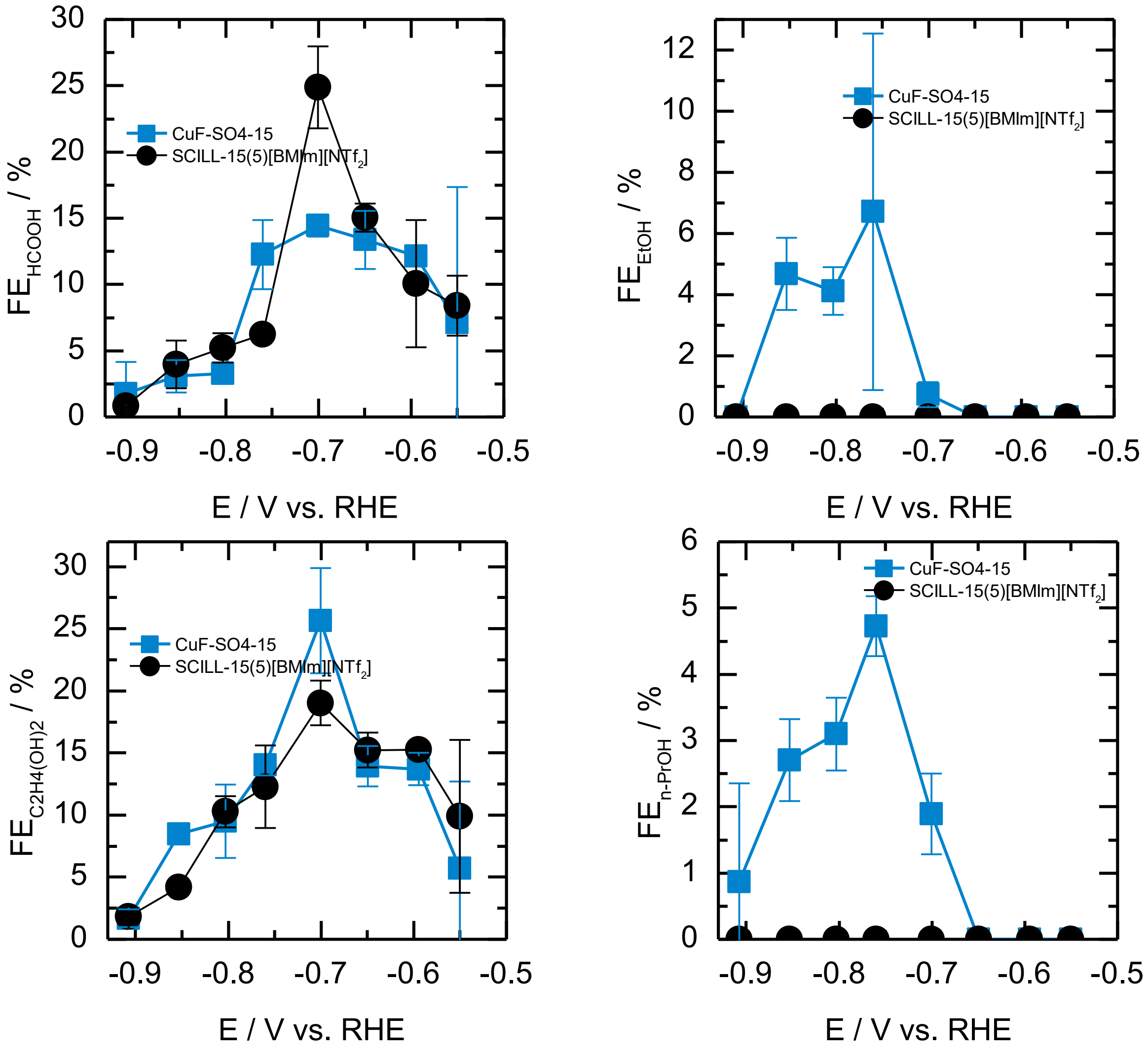

Figure 57: FE's for liquid phase products formate, ethanol, ethylene glycol and n-propanol at different potentials for CuF-SO4-15 (blue squares) and SCILL-15(5)[BMIm][NTf$_2$] (black dots).

The IL modification results demonstrate the role of the IL as a possible trapping agent. Analysis of the FE and current density experiments prior might allow deducing the CO_2 reduction pathways. This will be discussed in the following section.

Despite some controversies in understanding CO_2RR reaction pathways, some elementary steps found some consensus. The formation of the CO_2^- radical anion as the very first step by electron transfer to CO_2 is supposed to be the rate determining step. Furthermore, surface bound CO is identified as key intermediate for the formation of hydrocarbon formation, since the substitution of CO_2 by CO in Cu catalyzed reduction reaction gives a comparable product spectrum [121, 122, 123].

Nevertheless, it remains difficult about how the CO_2RR products are formed out of the adsorbed CO intermediate. By combination of the previously reported results of CO_2RR with the IL modified copper foam catalysts and the reported mechanism in literature, some of the reaction pathways are intended to be explained (scheme 21) [129].

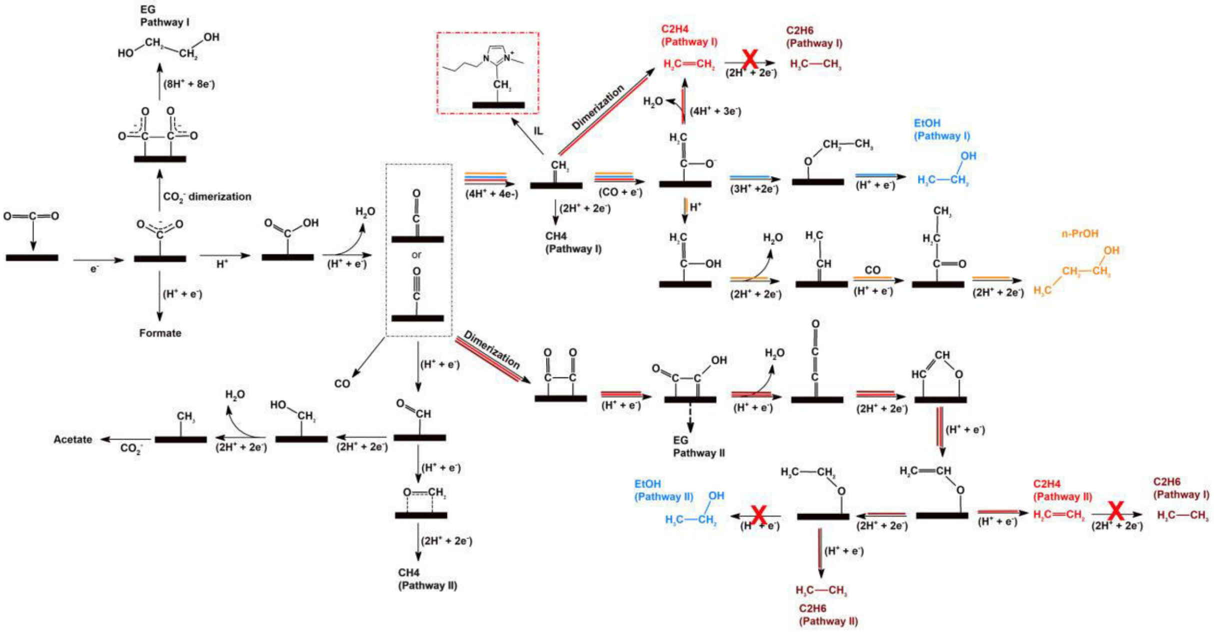

Scheme 21: Possible reaction pathways of the CO_2RR on Cu catalysts. The colored lines indicate the suggested reaction pathway for each product [129].

The influence on ethylene by IL modification of the catalyst is the most interesting among the CO_2 reduction products. At relatively high overpotentials, the formation of ethylene is suppressed while at low overpotentials, no impact of the IL modification on ethylene could be observed. This indicates two different pathways for ethylene formation at low and high overpotentials. This dual pathway mechanism was already proposed by *Koper et al.* [124] as a result of his CO reduction studies on Cu electrodes. Pathway II in scheme 21 shows the formation of ethylene at low overpotentials. Here, two adsorbed CO-intermediates are dimerizing prior to further reduction and protonation to form ethylene. At high overpotentials (pathway I), adsorbed CO-intermediate is protonated to CHO-intermediate, as suggested by *Peterson et al.*[125]. Pathway I was later modified by DFT calculations and experiments from *Asthagiri et al.* [46], who described the reduction of the adsorbed CO-intermediate to adsorbed COH. This intermediate could then be further reduced to carbene-like CH_2-intermediates, followed by C-C coupling of two CH_2-intermediates or by CO insertion, similar to Fischer-Tropsch process. The effect of IL modification is mainly given in pathway I. Here, The IL selectively suppresses the formation of crucial intermediates for the formation of ethylene, resulting in a suppressed ethylene formation at high overpotentials. At the same time, The CO dimerization in pathway II is not affected by the IL and thus the ethylene formation is not influenced at low overpotentials.

Also ethane was found as product, resulting from two more protonation steps. As a conclusion, the porous structure of the copper foam catalyst increases the residence time of adsorbed intermediate species. Since ethane and ethylene are not strongly differing in their chemical structure, the same formation pathways could be suggested. One suggestion could be the protonation of adsorbed or re-adsorbed ethylene. Nonetheless, as shown in figure 56, the FE of ethane was not affected by IL modification over the whole screened overpotential range, other than for ethylene. This implies a different Pathway for the formation of ethane. *Ma et al.* suggested the formation of ethane via CO dimerization [126], which is in agreement with prior results on ethylene formation, where the CO dimerization step is observed as unaffected by IL modification of the catalyst. As a conclusion, the main formation pathway for ethane must be pathway II, shown in scheme 21.

Also the ethanol formation is considered to pass via the ethylene formation pathway I or pathway II, depicted in scheme 21. However, figure 57 shows, that the formation of ethanol is completely suppressed by IL modification of the copper foam catalyst. Here, the IL could explicitly trap the intermediates needed for the formation of ethanol. Moreover, the formation of C_3 products as n-propanol is not observed at all on IL impregnated copper foam catalysts. As scheme 21 shows, the formation of n-propanol starts with an intramolecular C-C coupling of CO and hydrogenated carbon and protonation to form adsorbed propionaldehyde, which is reduced to n-propanol. For ethanol and n-propanol formation, carbene species as intermediates are crucial. As known from the experimental results on ethylene formation, pathways including carbene species or other hydrogenated carbon intermediates are suppressed by the IL. This could be verified with the results obtained for ethanol or n-propanol formation. It seems that the C2 position of the imidazole ring of the IL reacts with these intermediate species by deprotonation and alkylation. This underlines the influence of the C2 position of the IL as described in the literature [87]. Nevertheless, further spectroscopic and theoretical studies are needed to fully understand the interaction between the IL and the adsorbed key intermediates.

Ethylene glycol was detected as a further CO_2RR product with copper foam catalysts with FE's of up to 25 % on the pristine catalyst and up to 19 % on IL impregnated catalyst, shown in figure 57. These are significant values in comparison to the literature, where ethylene glycol is detected as a minor product [10]. In the same paper, ethylene glycol formation was suggested to pass via CO dimerization [10]. Furthermore, the results show, that the potential-dependend behavior of ethylene glycol formation is similar to formate formation. This indicates, that both products are sharing the adsorbed CO_2^- radical anion intermediate, as experimentally confirmed for formate [127]. Comparable to the formation of oxalate by CO dimerization [91], ethylene glycol formation might also be induced by dimerization of adsorbed CO_2^- radical anions. At -0.7 V vs. RHE, IL modification of the catalyst switches the major product from ethylene glycol to formate. This supports *Brennecke et al.*, suggesting that the IL is hindering the close approach of two adsorbed CO_2^- radical anions and therefore suppressing the dimerization of the latter [91]. Since the differences between the FE's are within the measurement error, no clear determination of the reaction pathways can be done.

Last of all, methane is produced with low FE independently from IL impregnation. As described in literature, the presence of Cu_2O species on the catalyst material could suppress the formation of methane [128]. As shown in figure 56, IL impregnation does not significantly affect methane formation, indicating that methane is preferably formed via adsorbed CHO intermediate (pathway II, scheme 21).

Since there exists a great structural flexibility in IL's, reaction pathway analyses can be done by engineering of specific IL's. This selective design of IL-intermediate interactions could be still feasible and could be used as method for further investigating CO_2 reduction pathways. One variation of the C2 position of the ionic liquid will be described in the next section.

According to the work of *Niu et al.* [87], the C2 position is influencing the catalytic performance, but the C4 and C5 position are suggested to be more important for the chemical interaction of the IL in CO_2RR [88]. Therefore, [BMIm][NTf_2] is exchanged by [BMMIm][NTf_2], where the C2 position is blocked by a methyl group. The results clearly indicated that the current density was not affected by the C2 position blocking over the current density range from -0.5 to -0.9 V vs. RHE (figure 58). This is an indicator, that the C2 position blocking of the IL is not affecting the overall effective kinetics of the CO_2 conversion.

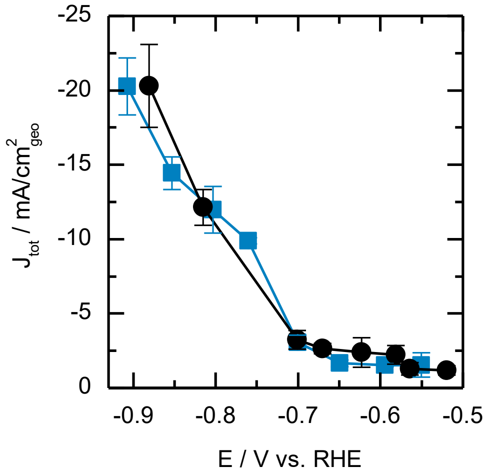

Figure 58: Total current density at different potentials for SCILL-15(5)[BMIm][NTf_2] (blue squares) and SCILL-15(5)[BMMIm][NTf_2] (black dots).

Since the HER is still the predominating reaction under CO_2RR reaction conditions, the hydrogen faraday efficiency showed no tremendous difference over the whole potential range when blocking the C2 position of the ionic liquid, illustrated in figure 59. The minimum of hydrogen FE is around 40 % for both SCILL systems with a difference of 100 mV in the applied potential. The SCILL-

15(5)[BMIm][NTf$_2$] system showed the minimum at -0.7 V vs. RHE while the SCILL-15(5)[BMMIm][NTf$_2$] system showed it at -0.6 V vs. RHE.

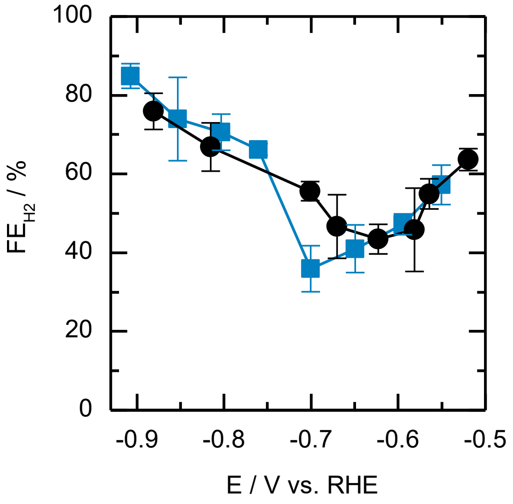

Figure 59: Hydrogen FE at different potentials for SCILL-15(5)[BMIm][NTf$_2$] (blue squares) and SCILL-15(5)[BMMIm][NTf$_2$] (black dots).

If the C2 position would be not important for the CO$_2$RR intermediate stabilization, also the CO$_2$RR product and FE distribution should not be different. Therefore, the CO$_2$RR products FE were calculated and compared for both SCILL systems. The comparison of the gas phase products is depicted in figure 60.

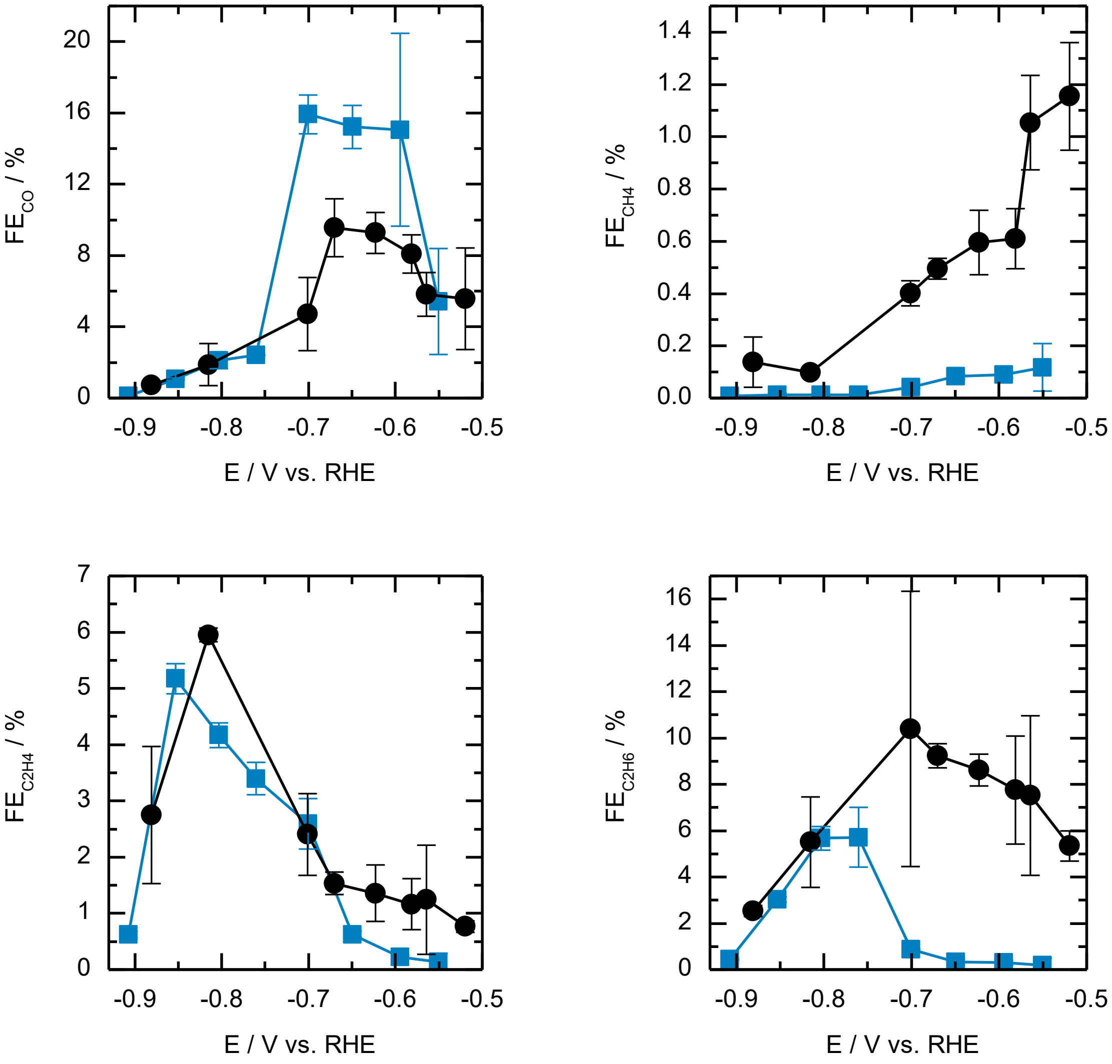

Figure 60: FE's for CO, CH_4, C_2H_4 and C_2H_6 at different potentials for SCILL-15(5)[BMIm][NTf_2] (blue squares) and SCILL-15(5)[BMMIm][NTf_2] (black dots).

Depending on the chemical species, either there is a difference or not between the two SCILL systems. Carbon monoxide is the very first product built up in the CO_2RR directly by an adsorbed CO intermediate at the electrode surface. Therefore, it is not surprising, that the general trend of the FE over the whole potential range was not different for both SCILL systems. At higher overpotentials than -0.75 V vs. RHE and at lower overpotentials than -0.55 V vs. RHE, there was no difference in CO faradaic efficiencies. In between this potential range, there is a visible difference. While for the SCILL system with [BMIm][NTf_2] a maximum FE of CO of 16 % at around -0.7 V vs. RHE was achieved, methylation of the C2 position of the IL dropped the faradaic efficiency to around 10 % FE. This could be a stabilization effect of the CO intermediate at the electrode surface. The increased stabilization of the CO intermediate also explains the increased FE for ethane. Here, nearly 10 % FE at -0.7 V vs. RHE could be achieved by blocking the C2 position. Without C2 methylation, the maximum FE for ethane is around 6 % at -0.8 V vs. RHE. The boosting of ethane is dominating at lower overpotentials than -0.7 V vs. RHE. Regarding the mechanism proposed in scheme 21, the decrease in the FE of CO and the increase in the FE of ethane is supporting the reaction pathway II for the ethane production via CO dimerization. This is supported by the fact, that the faradaic efficiencies of ethylene are not affected by the C2 methylation over the whole potential range, indicating that reaction pathway I is not feasible for ethane formation. On the other hand, this result also indicates no preference in reaction pathways I or II for ethylene formation. The same is valid for the formation of methane, although FE's of around 1 % could be achieved by blocking the C2 position of the imidazole ring.

Except from acetate, the liquid phase products are suppressed by C2 position blocking (figure 61). The SCILL system with [BMIm][NTf_2] was successful in producing formate and ethylene glycol with faradaic efficiencies upto 20 %. Both chemical components are dramatically reduced by blocking the C2 position of the IL. With increasing overpotential, the FE of formate is dropping. The maximum FE reached in this study was around 8 % FE at around -0.5 V vs. RHE. This is a tremendous drop to the non-methylated IL, where 25 % FE for formate could be achieved at -0.7 V vs. RHE. From the mechanistic point of view, the explanation could be some sterical effect of the methyl group. The formation of formate is done by directly protonating the adsorbed CO_2^- intermediate species. Due to space issues at the partially IL covered electrode surface, the dehydratisation of the adsorbed CO(OH) intermediate is favored to the desorption of formate from the electrode surface. For ethylene glycol, the maximum FE could be reached with around 20 % at -0.7 V vs. RHE by using [BMIm][NTf_2] for the SCILL catalyst. Blocking of the C2 position of the imidazole ring decreased the FE to below 4 % at the same overpotential. Also here, sterical issues could explain the phenomenon. The formation of ethylene glycol goes via the CO_2^- -dimerization. This dimer needs more space at the electrode surface than the protonation of the CO_2^- intermediate to the adsorbed CO(OH) surface species, thus favoring pathways going via adsorbed CO surface species. The increase in acetate faradaic efficiencies supports this hypothesis. With the C2 methylated IL, it was possible to reach FE of 5 % for acetate at -0.55 V vs. RHE, while for the non-methylated IL the FE is always below 1 % over the whole potential range.

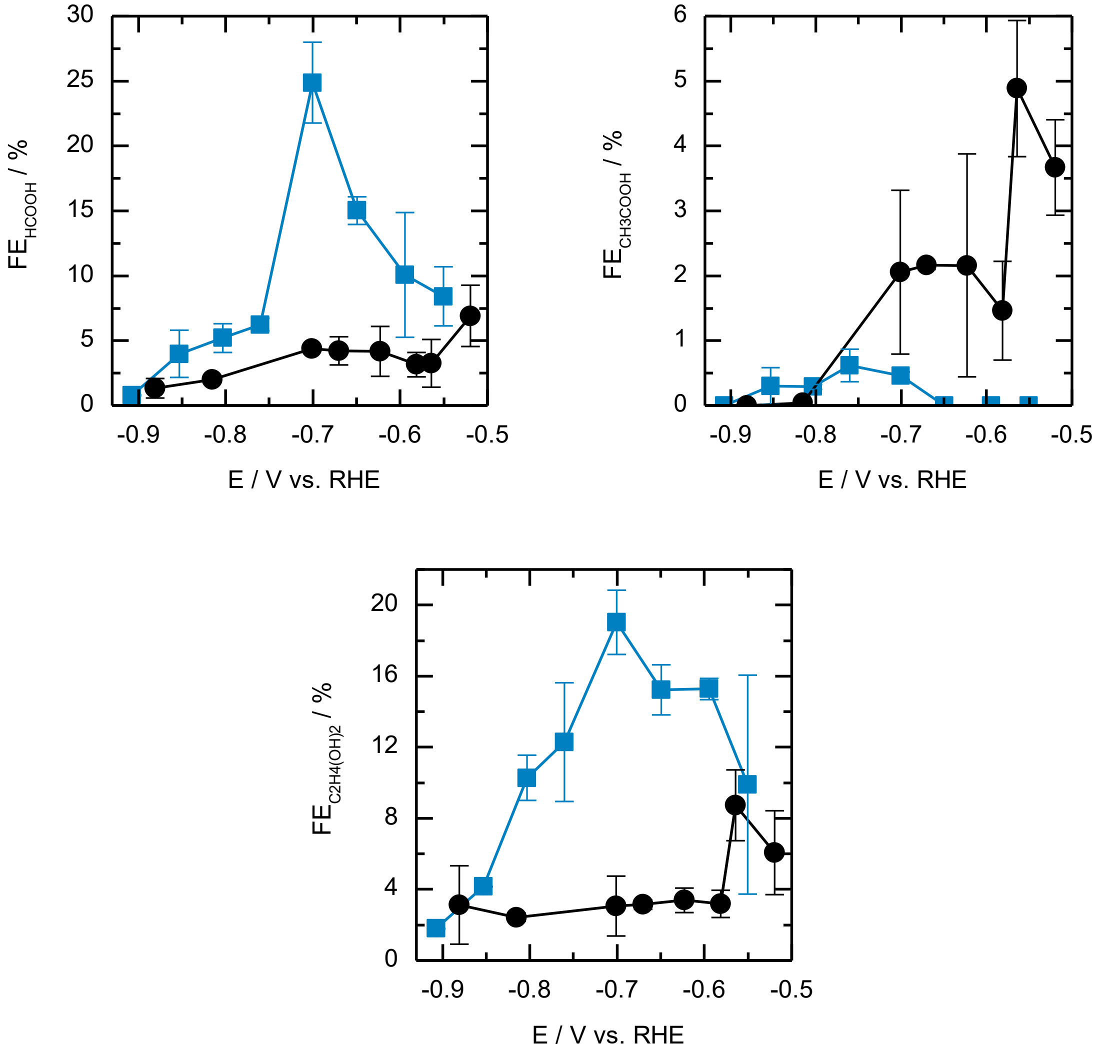

Figure 61: FE's for formate, acetate and ethylene glycol at different potentials for SCILL-15(5)[BMIm][NTf$_2$] (blue squares) and SCILL-15(5)[BMMIm][NTf$_2$] (black dots).

Furthermore, it is important that the suppression of alcohols like ethanol or n-propanol was independent from the methylation of the C2 position.

The methylation of the C2 position of the imidazole ring supports the mechanistic hypothesis drawn in scheme 21. Especially the importance of the adsorbed CO surface intermediate and the IL coverage is of importance.

To be successful, the performance of the SCILL catalyst must be at least as good as for the reaction system with IL. Therefore, the same amount of IL used for the impregnation of the copper foam catalyst was directly added to the electrolyte. Here, only [BMIm]$^+$ cations were used. Since the solubility of [BMIm][NTf$_2$] is limited due to the hydrophobicity of the [NTf$_2$]$^-$ anion, the anion was also changed to [OTf]⁻. Figure 62 compares the overall current densities of the SCILL system with the IL as supporting electrolyte.

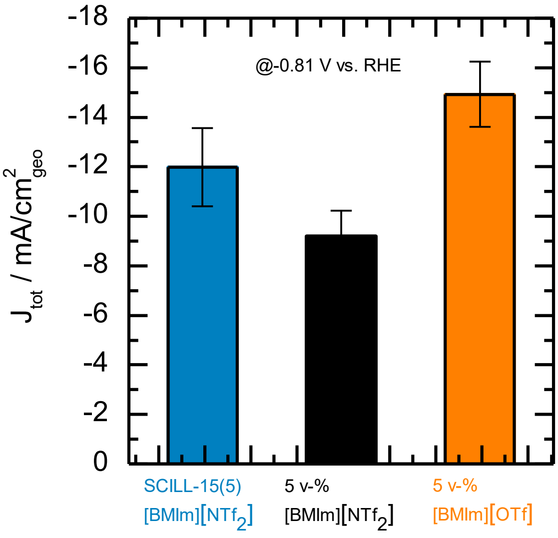

Figure 62: Total current densities for SCILL-15(5)[BMIm][NTf$_2$] (blue), [BMIm][NTf$_2$] as supporting electrolyte (black) and [BMIm][OTf] as supporting electrolyte (orange). All values at -0.81 V vs. RHE.

Directly comparing the [BMIm][NTf$_2$] as SCILL and as supporting electrolyte shows, that the current density was increased with introducing the SCILL concept. The current density for the SCILL catalyst is as high as -12 mA/cm² at -0.81 V vs. RHE whereas for the IL as supporting electrolyte it is as high as -9 mA/cm² at the same potential. Since the current density is an indicator for the productivity and directly proportional to the CO_2 conversion rate, the introduction of SCILL is emphasized by these results. The change of the anion to [OTf]⁻ was further increasing the overall current density to -15 mA/cm². The influence of the anion described in the literature is therefore verified [63].

The overall product spectrum itself did not change for [BMIm][NTf$_2$] by introducing the SCILL concept, as shown in figure 63. All values are shown for a potential of -0.81 V vs. RHE. No difference between the SCILL and the IL as supporting electrolyte regarding the hydrogen FE could be observed. In both cases it is between 70 and 65 % FE. While the FE's of carbon monoxide (2 %) and ethane (5 %) are comparable for both IL concepts, the FE for ethylene is dropped from around 7 % FE to 4 % by introducing the SCILL concept. On the other hand, the faradaic efficiency of formate could be increased from 3 % to 5 % by SCILL. The increase in ethylene glycol FE is even more pronounced. SCILL increased the FE from 2 % to 10 %. Methane and acetate are nearly not formed in both cases.

The results led to the conclusion that not only the current density but also product selectivities could be influenced by the introduction of the SCILL concept. Here, the surface coverage of the ionic liquid and the surface-IL interactions seem to be crucial.

Switching now the anion in the supporting electrolyte to $[OTf]^-$ increased the hydrogen FE to 85 %. Furthermore, changing the anion also changes the product spectrum. Chemical species as gas phase hydrocarbons or hydrocarbons other than formate in the liquid phase were completely suppressed. This illustrates the product spectrum achieved by literature results [81]. Here, the carbon monoxide FE is suppressed to below 1 % and the FE of formate is increased to above 9 %. These results clarified that the anion plays a role in the intermediate stabilization at the electrode surface.

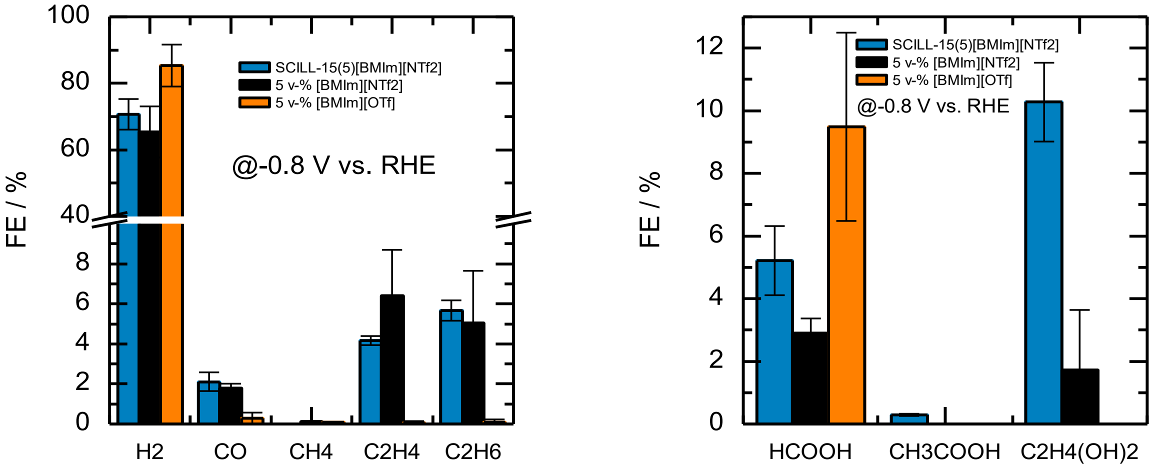

Figure 63: FE's for gas phase products (left) and liquid phase products (right) for SCILL-15(5)[BMIm][NTf$_2$] (blue), [BMIm][NTf$_2$] as supporting electrolyte (black) and [BMIm][OTf] as supporting electrolyte (orange). All values at -0.81 V vs. RHE.

6. Summary

First of all, a known literature protocol was established for the synthesis of copper foam materials. Under harsh conditions for the deposition potential and deposition current, copper foam materials were synthesized at different amounts of electric charges. Material properties like the deposited mass, the surface pore diameter, the foam thickness and the roughness factor were investigated by SEM and the methyl viologen method. All numbered properties are increasing when increasing the number of coulombs during the deposition process. The results show, that changing one parameter during the electrodeposition process affects several material properties of the copper foams at the same time.

To better control the resulting material properties, the forced convection approach by stirring the deposition solution was applied. This method was identified as suitable way to change the surface pore diameter by different stirring speeds and keep the parameters like deposited mass, foam thickness or roughness factor constant.

In the following part of the studies, two different reactor types developed in two generations were tested. The H-type cell and two modular electrolyzers.

The investigations with the H-type cell were focused on the current densities achieved for the pristine copper plate and the copper foam synthesized with 150 C. Potential corrections and iR-compensation were not paid attention in this part of the studies. While for the pristine copper plate the CV current density was increasing in CO_2 purged electrolyte in comparison to N_2 purged electrolyte, the opposite was observed for the copper foam catalyst. This could have two reasons. On one hand, the HER could be suppressed, on the other hand, pore diffusion limitations could play a role. Nontheless, copper foam catalyst achieved a higher total current density than the copper plate. Due to dilution problems, offline analytics were not able for the liquid and the gas phase.

To face the analytical problem, a modular PMMA electrolyzer was developed. It had a much more reduced electrolyte volume und thus dilution problems should be overcome. But the analytics were still difficult, especially for the gas phase. This led to the establishment of an online GC. Moreover, the PMMA electrolyzer suffered some more problems. At higher overpotentials, the measurements were interrupted by the instrument due to current overload problems. Measuring the counter electrode cell voltage over time showed for the cation exchange membrane an increase to the limit of the instrument. This problem could be overcome by using an anion exchange membrane. First results with the SCILL system showed a promising boosting in the current density, but the systems suffered an induction period in the current density progress over time. Here, contamination and cleaning problems were supposed to be the reasons.

In order to have a better cleanable material, PEEK was used for a new electrolyzer. Beside further reducing the electrolyte volume, using a better performing anion exchange membrane and the application of the online GC system, the reactor feed inlet was optimized from the side to the bottom.

Here, higher CO and lower H_2 faradaic efficiencies could be achieved. Faradaic efficiencies in favor to CO_2RR products could be reached by pretreating the copper substrate and further improved by optimizing the CO_2 flow rate. Here, also the potential error in combination with the solution resistance determination was investigated, as well as the uncertainty quantification of the gas phase products.

For different applied coulombs during the copper foam synthesis, the total current density difference in CO_2RR between two different applied coulombs decreased with increasing overpotential and increasing applied coulombs. Moreover, increasing the deposition coulombs increased the FE of hydrogen and decreased those of the other gas phase products. Also the liquid phase products FE's were decreased, except of ethylene glycol, which was not affected. Product analysis for the 600 C deposited copper foam could not be measured due to instabilities of the current density over time even at low overpotentials.

The catalysts prepared with the forced convection approach showed strong differences to the unstirred prepared copper foams. The pore diameter variation by forced convection had no influence on the gas phase products, but affected especially the alcohol formation in the liquid phase.

The IL impregnation by drop coating showed a clear film of IL covering copper dentrides, visualized by SEM. The homogeneous distribution of ionic liquid in the copper foam material could be proven by EDS. XPS also showed, that the IL loading amount influenced the copper electronic state. The roughness factor for IL impregnated copper foams is higher than for the pristine ones. The SCILL system with [BMIm][NTf_2] did not affect the current densities over the whole potential range compared to the pristine copper foam. Beside a slightly increase in hydrogen FE, the gas phase is mainly affected by suppression of ethylene formation when applying the SCILL concept. In the liquid phase, a complete suppression of alcohols could be observed. This led to the hypothesis, that ionic liquids could interact as chemical trapping agents for intermediates and thus controlling reaction pathways. This could be proven by using [BMMIm][NTf_2] for the SCILL, where further reaction pathways for CO, ethane, methane, formate, ethylene glycol and acetate could be influenced. The advantage of using [BMIm][NTf_2] as SCILL and not as electrolyte additive was an increasing total current density, formate FE and ethylene glycol FE but a decreasing ethylene FE. Using [NTf_2]$^-$ as anion instead of [OTf]$^-$ decreased the hydrogen FE as well as the formate FE, but widens the overall product spectrum, like the formation of ethylene glycol.

7. Literature

[1] https://www.icos-cp.eu/GCP/2017, last proofed: 15.01.2021, 06:23.

[2] C. Le Quéré et. al., *Earth Syst. Sci. Data*, **2018**, 10, 405 – 448.

[3] N. L. Panwar, S. C. Kaushik, S. Kothari, *Renewable and Sustainable Energy Reviews*, **2011**, 15, 1513 – 1524.

[4] P. Bains, P. Psarras, J. Wilcox, *Progress in Energy and Combustion Science*, **2017**, 63, 146 – 172.

[5] D. J. Barker, S. A. Turner, P. A. Napier-Moore, M. Clark, J. E. Davison, *Energy Procedia*, **2009**, 87 – 94.

[6] D. Gielen, *Energy Conversion and Management*, **2003**, 44, 1027 – 1037.

[7] G. A. Olah, G. K. S. Prakash, A. Goeppert, *J. Am. Chem. Soc.*, **2011**, 133, 12881 – 12898.

[8] W. Vielstich, H. A. Gasteiger, A. Lamm, *Handbook of Fuel Cells Volume 2*, John Wiley, **2003**.

[9] E. V. Kondratenko, G. Mul, J. Baltrusaitis, G. O. Larrazábalc, J. Pérez-Ramírez, *Energy Environ. Sci.*, **2013**, 6, 3112 – 3135.

[10] K. P. Kuhl, E. R. Cave, D. N. Abram, T. F. Jaramillo, *Energy Environ. Sci.*, **2012**, 5, 7050 – 7059.

[11] Y. Hori, A. Murata, R. Takahashi, *J. Chem. Soc., Faraday Trans. 1*, **1989**, 85, 2309 – 2326.

[12] Y. Hori, I. Takahashi, O. Koga, N. Hoshi, *Journal of Molecular Catalysis A: Chemical*, **2003**, 199, 39 – 47.

[13] R. Reske, H. Mistry, F. Behafarid, B. Roldan Cuenya, P. Strasser, *J. Am. Chem. Soc.*, **2014**, 136, 6978 – 6986.

[14] S. Sen, D. Liu, G. T. R. Palmore, *ACS Catal.*, **2014**, 4, 3091 – 3095.

[15] A. Dutta, M. Rahaman, N. C. Luedi, M. Mohos, P. Broekmann, *ACS Catal.*, **2016**, 6, 3804 – 3814.

[16] E. E. Benson, C. P. Kubiak, A. J. Sathrum, J. M. Smieja, *Chem.Soc.Rev.*, **2009**, 38, 89 – 99.

[17] R. J. Lim, M. Xie, M. A. Sk, J.-M. Lee, A. Fisher, X. Wang, K. H. Lim, *Catalysis Today*, **2014**, 233, 169 – 180.

[18] X. Lu, D. Y. C. Leung, H. Wang, M. K. H. Leung, J. Xuan, *ChemElectroChem*, **2014**, 1, 836 – 849.

[19] J. Qiao, Y. Liu, F. Hong, J. Zhang, *Chem. Soc. Rev.*, **2014**, 43, 631 – 675.

[20] V. M. Schmidt, *Elektrochemische Verfahrenstechnik*, Wiley-VCH, Weinheim, **2003**.

[21] I. Takahashi, O. Koga, N. Hoshi, Y. Hori, *Journal of Electroanalytical Chemistry*, **2002**, 533, 135 – 143.

[22] C. Hahna, T. Hatsukadea, Y.-G. Kimc, A. Vailionisd, J. H. Baricuatroc, D. C. Higginsa, S. A. Nitopia, M. P. Soriagac, T. F. Jaramillo, *PNAS*, **2017**, 114, 5918 – 5923.

[23] X. Nie, W. Luo, M. J. Janik, A. Asthagiri, *Journal of Catalysis*, **2014**, 312, 108 – 122.

[24] W. Luo, X. Nie, M. J. Janik, A. Asthagiri, *ACS Catal.*, **2016**, 6, 219 – 229.

[25] X. Sun, X. Cao, P. Hu, *Sci. China Chem.*, **2015**, 58, 553 – 564.

[26] S. P. Liu, M. Zhao, W. Gao, Q. Jiang, *ChemSusChem*, **2016**, 9, 1 – 8.

[27] H. Mistry, F. Behafarid, R. Reske, A. S. Varela, P. Strasser, B. R. Cuenya, *ACS Catal.*, **2016**, 6, 1075 – 1080.

[28] Y. Kwon, Y. Lum, E. L. Clark, J. W. Ager, A. T. Bell, *ChemElectroChem*, **2016**, 3,1012 – 1019.

[29] A. Eilert, F. S. Roberts, D. Friebel, A. Nilsson, *J. Phys. Chem. Lett.*, **2016**, 7, 1466 – 1470.

[30] K. Zhao, Y. Liu, X. Quan, S. Chen, H. Yu, *ACS Appl. Mater. Interfaces*, **2017**, 9, 5302 – 5311.

[31] C. S. Chen, J. H. Wan, B. S. Yeo, *J. Phys. Chem. C*, **2015**, 119, 26875 – 26882.

[32] O. A. Baturina, Q. Lu, M. A. Padilla, L. Xin, W. Li, A. Serov, K. Artyushkova, P. Atanassov, F. Xu, A. Epshteyn, T. Brintlinger, M. Schuette, G. E. Collins, *ACS Catal.*, **2014**, 4, 3682 – 3695.

[33] O. Baturina, Q. Lu, F. Xu, A. Purdy, B. Dyatkin, X. Sang, R. Unocic, T. Brintlinger, Y. Gogotsi, *Catalysis Today*, **2017**, 288, 2 – 10.

[34] M. Ma, K. Djanashvili, W. A. Smith, *Phys. Chem. Chem. Phys.*, **2015**, 17, 20861 – 20867.

[35] M. Ma, K. Djanashvili, W. A. Smith, *Angew .Chem.*, **2016**, 128, 6792 – 6796.

[36] R. Kas, K. K. Hummadi, R. Kortlever, P. de Wit, A. Milbrat, M. W. J. Luiten-Olieman, N. E. Benes, M. T. M. Koper, G. Mul, *Nature Communications*, **2016**, 7, 10748 – 10754.

[37] P. De Luna, R. Quintero-Bermudez, C.-T. Dinh, M. B. Ross, O. S. Bushuyev, P. Todorović, T. Regier, S. O. Kelley, P. Yang, E. H. Sargent, *Nature Catalysis*, **2018**, 1, 103 – 110.

[38] Y. Peng, T. Wu, L. Sun, J. M. V. Nsanzimana, A. C. Fisher, X. Wang, *ACS Appl. Mater. Interfaces*, **2017**, 9, 32782 – 32789.

[39] T. T. H. Hoang, S. Ma, J. I. Gold, P. J. A. Kenis, A. A. Gewirth, *ACS Catal.*, **2017**, 7, 3313 – 3321.

[40] H.-C. Shin, M. Liu, *Chem. Mater.*, **2004**, 16, 5460 – 5464.

[41] M. Rahaman, A. Dutta, A. Zanetti, P. Broekmann, *ACS Catal.*, **2017**, 7, 7946 – 7956.

[42] A. Dutta, M. Rahaman, M. Mohos, A. Zanetti, P. Broekmann, *ACS Catal.*, **2017**, 7, 5431 – 5437.

[43] Y.-J. Zhang, V. Sethuraman, R. Michalsky, A. A. Peterson, *ACS Catal.*, **2014**, 4, 3742 – 3748.

[44] J. H. Montoya, C. Shi, K. Chan, J. K. Nørskov, *J. Phys. Chem. Lett.*, **2015**, 6, 2032 – 2037.

[45] J. D. Goodpaster, A. T. Bell, M. Head-Gordon, *J. Phys. Chem. Lett.*, **2016**, 7, 1471 – 1477.

[46] X. Nie, M. R. Esopi, M. J. Janik, A. Asthagiri, *Angew. Chem. Int. Ed.*, **2013**, 52, 2459 – 2462.

[47] C. Long, X. Li, J. Guo, Y. Shi, S. Liu, Z. Tang, *Small Methods*, **2019**, 3, 1800369.

[48] A. J. Garza, A. T. Bell, M. Head-Gordon, *ACS Catal.*, **2018**, 8, 1490 – 1499.

[49] Y. Zheng, A. Vasileff, X. Zhou, Y. Jiao, M. Jaroniec, S.-Z. Qiao, *J. Am. Chem. Soc.*, **2019**, 141, 7646 – 7659.

[50] J. L. Anthony, J. L. Anderson, E. J. Maginn, J. F. Brennecke, *J. Phys. Chem. B*, **2005**, 109, 6366 – 6374.

[51] R. Sander, *Atmos. Chem. Phys.*, **2015**, 15, 4399 – 4981.

[52] Y. Wang, M. Hatakeyama, K. Ogata, M. Wakabayashi, F. Jin, S. Nakamura, *Phys. Chem. Chem. Phys.*, **2015**, 17, 23521 – 23531.

[53] B. A. Rosen, A. Salehi-Khojin, M. R. Thorson, W. Zhu, D. T. Whipple, P. J. Kenis, R. I. Masel, *Science*, **2011**, 334, 643 – 644.

[54] G.-R. Zhang, B. J. M. Etzold, *Journal of Energy Chemistry*, **2016**, 25, 199 – 207.

[55] U. Kernchen, B. Etzold, W. Korth, A. Jess, *Chem. Eng. Technol.*, **2007**, 30, 8, 985 – 994.

[56] U. Kernchen, B. Etzold, W. Korth, A. Jess, *Chemie Ingenieur Technik*, **2007**, 79, 807 – 819.

[57] H.-P. Steinrück, P. Wasserscheid, *Catal Lett*, **2015**, 145, 380 – 397.

[58] J. Snyder, T. Fujita, M. W. Chen, J. Erlebacher, *Nature Materials*, **2010**, 9, 904 – 907.

[59] G.-R. Zhang, M. Munoz, B. J. M. Etzold, *Angew. Chem. Int. Ed.*, **2016**, 55, 2257 – 2261.

[60] I. Martinaiou, T. Wolker, A. Shahraeia, G.-R. Zhang, A. Janßen, S. Wagner, N. Weidler, R. W. Stark, B. J. M. Etzold, U. I. Kramm, *Journal of Power Sources*, **2018**, 375, 222 – 232.

[61] J. Feng, S. Zeng, J. Feng, H. Dong, X. Zhang, *Chin. J. Chem.*, **2018**, 36, 961—970.

[62] B. C. M. Martindale, R. G. Compton, *Chem. Commun.*, **2012**, 48, 6487 – 6489.

[63] E. E. L. Tanner, C. Batchelor-McAuley, R. G. Compton, *J. Phys. Chem. C*, **2016**, 120, 26442 – 26447.

[64] D. W. Yang, Q. Y. Li, F. X. Shen, Q. Wang, L. Li, N. Song, Y. N. Dai, J. Shi, *Electrochim. Acta*, **2015**, 189, 32.

[65] J. L. DiMeglio, J. Rosenthal, *J. Am. Chem. Soc.*, **2013**, 135, 8798 - 8801.

[66] J. Medina-Ramos, J.L. DiMeglio, J. Rosenthal, *J. Am. Chem. Soc.*, **2014**, 136, 8361 - 8367.

[67] J. Medina-Ramos, S. S. Lee, T. T. Fister, A. A. Hubaud, R. L. Sacci, D. R. Mullins, J. L. DiMeglio, R. C. Pupillo, S. M. Velardo, D. A. Lutterman, J. Rosenthal, P. Fenter, *ACS Catal.*, **2017**, 7, 7285 – 7295.

[68] M. Asadi, B. Kumar, A. Behranginia, B. A. Rosen, A. Baskin, N. Repnin, D. Pisasale, P. Phillips, W. Zhu, R. Haasch, R. F. Klie, P. Kral, J. Abiade, A. Salehi-Khojin, *Nature Communications*, **2014**, 5, 4470.

[69] Y. Oh, X. Hu, *Chem. Commun.*, **2015**, 51, 13698 – 13701.

[70] Q. Zhu, J. Ma, X. Kang, X. Sun, H. Liu, J. Hu, Z. Liu, B. Han, *Angew. Chem. Int. Ed.*, **2016**, 55, 9012 – 9016.

[71] X. Zhang, Y. Zhao, S. Hu, M. E. Gliege, Y. Liu, R. Liu, L. Scudiero, Y. Hu, S. Ha, *Electrochimica Acta*, **2017**, 247, 281 – 287.

[72] N. Hollingsworth, S. F. R. Taylor, M. T. Galante, J. Jacquemin, C. Longo, K. B. Holt, N. H. de Leeuw, C. Hardacre, *Angew. Chem. Int. Ed.*, **2015**, 54, 1 – 6.

[73] A. Atifi, D. W. Boyce, J. L. DiMeglio, J. Rosenthal, *ACS Catal.*, **2018**, 8, 2857 – 2863.

[74] X. Y. Wang, S. Q. Liu, K. L. Huang, Q. J. Feng, D. L. Ye, B. Liu, J. L. Liu, G. H. Jin, *Chinese Chemical Letters*, **2010**, 21, 987 – 990.

[75] Q. Feng, S. Liu, *Asian Journal of Chemistry*, **2011**, 23, 4823 – 4826.

[76] T. Pardal, S. Messias, M. Sousa, A. S. R. Machado, C. M. Rangel, D. Nunes, J. V. Pinto, R. Martins, M. N. da Ponte, *Journal of CO2 Utilization*, **2017**, 18, 62 – 72.

[77] F. Zhou, S. Liu, B. Yang, P. Wang, A. S. Alshammari, Y. Deng, *Electrochemistry Communications*, **2015**, 55, 43 – 46.

[78] G. Zhao, T. Jiang, B. Han, Z. Li, J. Zhang, Z. Liu, J. He, W. Wu, *J. of Supercritical Fluids*, **2004**, 32, 287 – 291.

[79] S. Ponnurangam, C. M. Yun, I. V. Chernyshova, *ChemElectroChem*, **2016**, 3, 74 – 82.

[80] Z. Han, R. Kortlever, H.-Y. Chen, J. C. Peters, T. Agapie, *ACS Cent. Sci.*, **2017**, 3, 853 – 859.

[81] T. N. Huan, P. Simon, G. Rousse, I. Génois, V. Artero, M. Fontecave, *Chem. Sci.*, **2017**, 8, 742 – 747.

[82] B. A. Rosen, J. L. Haan, P. Mukherjee, B. Braunschweig, W. Zhu, A. Salehi-Khojin, D. D. Dlott, R. I. Masel, *J. Phys. Chem. C*, **2012**, 116, 15307–15312.

[83] N. G. Rey, D. D. Dlott, *J. Phys. Chem. C*, **2015**, 119, 20892 – 20899.

[84] T. Pajkossy, *Solid State Ionics*, **2005**, 176, 1997 – 2003.

[85] D.-W. Yang, Q. Y. Li, F. X. Shen, Q. Wang, L. Li, N. Song, Y. N. Dai, J. Shi, *Electrochim. Acta*, **2016**, 189, 32 – 37.

[86] A. Marjolin, J. A. Keith, *ACS Catal.*, **2015**, 5, 1123 – 1130.

[87] D. Niu, H. Wang, H. Li, Z. Wu, X. Zhan, *Electrochimica Acta*, **2015**, 158, 138 – 142.

[88] G. P. S. Lau, M. Schreier,.D. Vasilyev, R. Scopelliti, M. Grätzel, P. J. Dyson, *J. Am. Chem. Soc.*, **2016**, 138, 7820 – 7823.

[89] M. A. Montiel, J. Solla-Gullo, V. Montiela, C. M. Sanchez-Sanchez, *Phys. Chem. Chem. Phys.*, **2018**, 20, 19160 – 19167.

[90] H.-K. Lim, Y. Kwon, H. S. Kim, J. Jeon, Y.-H. Kim, J.-A. Lim, B.-S. Kim, J. Choi, H. Kim, *ACS Catal.*, **2018**, 8, 2420 – 2427.

[91] L. Sun, G. K. Ramesha, P. V. Kamat, J. F. Brennecke, *Langmuir*, **2014**, 30, 6302 – 6308.

[92] https://web.archive.org/web/20100327114304/http://jcbmac.chem.brown.edu/myl/hen/carbondioxideHenry.html, geprüft am 15.01.2021, 13:16.

[93] T. Saeki, K. Hashimoto, A. Fujishima, N. Kimura, K. Omata, *J. Phys. Chem.*, **1995**, 99, 8440 – 8446.

[94] H. De Jesus-Cardona, C. del Moral, C. R. Cabrera, *Journal of Electroanalytical Chemistry*, **2001**, 513, 45 – 51.

[95] T. Mizuno, A. Naitoh, K. Ohta, *J. Electroanal. Chem.*, **1995**, 391, 199 - 201.

[96] S. Kaneco, N.-h. Hiei, Y. Xing, H. Katsumata, H. Ohnishi, T. Suzuki, K. Ohta, *Electrochimica Acta*, **2002**, 48, 51 – 55.

[97] S. Kaneco, K. Iiba, H. Katsumata, T. Suzuki, K. Ohta, *Chemical Engineering Journal*, **2007**, 128, 47 – 50.

[98] S. Kaneco, K. Iiba, N.-h. Hiei, K. Ohta, T. Mizuno, T. Suzuki, *Electrochimica Acta*, **1999**, 44, 4701 – 4706.

[99] S. Kaneco, K. Iiba, H. Katsumata, T. Suzuki, K. Ohta, *J Solid State Electrochem*, **2007**, 11, 490 – 495.

[100] T. Mizuno, K. Ohta, M. Kawamoto, A. Saji, *Energy Sources*, **1997**, 19, 249 – 257.

[101] M. Bevilacqua, J. Filippi, H. A. Miller, F. Vizza, *Energy Technol.*, **2015**, 3, 197 – 210.

[102] J. Lee, Y. Tak, *Electrochim. Acta*, **2001**, 46, 3015 – 3022.

[103] F. Köleli, T. Atilan, N. Palamut, A. M. Gizir, R. Aydin, C. H. Hamann, *J. Appl. Electrochem.*, **2003**, 33,447 – 450.

[104] F. Köleli, D. Balun, *Appl. Catal. A*, **2004**, 274, 237 – 242.

[105] H. Wang, D. Y. C. Leung, J. Xuan, *Appl. Energy*, **2013**, 102, 1057 – 1062.

[106] H. Li, C. Oloman, *Journal of Applied Electrochemistry*, **2005**, 35, 955 – 965.

[107] C. Oloman, H. Li, *ChemSusChem*, **2008**, 1, 385 – 391.

[108] M. Alvarez-Guerra, S. Quintanilla, A. Irabien, *Chem. Eng. J.*, **2012**, 207 – 208, 278 – 284.

[109] B. Innocent, D. Liaigre, D. Pasquier, F. Ropital, J.-M. Leger, K. B. Kokoh, *J. Appl. Electrochem.*, **2009**, 39, 227 – 232.

[110] J. Wu, F. G. Risalvato, S. Ma, X.-D. Zhou, *J. Mater. Chem. A*, **2014**, 2, 1647 – 1651.

[111] M. Bevilacqua, J. Filippi, A. Lavacchi, A. Marchionni, H. A. Miller, W. Oberhauser, E. Vesselli, F. Vizza, *Energy Technol.*, **2014**, 2, 522 – 525.

[112] K. Jiang, R. B. Sandberg, A. J. Akey, X. Liu, D. C. Bell, J. K. Nørskov, K. Chan, H. Wang, *Nature Catalysis*, **2018**, 1, 111 – 119.

[113] G. Kyriacou, A. Anagnostopoulos, *J. Electroad. Chem.*, **1992**, 322, 233 – 246.

[114] A. Wuttig, Y. Surendranath, *ACS Catal.*, **2015**, 5, 4479 – 4484.

[115] Z. P. Jovanov, J. F. de Araujo, S. Li, P. Strasser, *J. Phys. Chem. C*, **2019**, 123, 2165 – 2174.

[116] K. Y. Leung, C. C. L. McCrory, *ACS Appl. Energy Mater.*, **2019**, 2, 11, 8283 – 8293.

[117] S. Pujiastuti, H. Onggo, *AIP Conference Proceedings*, **2016**, 1711, 060006.

[118] P. J. Hore, *Journal of Magnetic Resonance*, **1983**, 54, 539 - 542.

[119] N.-T. Suen, S.-F. Hung, Q. Quan, N. Zhang, Y.-J. Xu, H. M. Chen, *Chem. Soc. Rev.*, **2017**, 46, 337 - 365.

[120] J. H. Koh, H. S. Jeon, M. S. Jee, E. B. Nursanto, H. Lee, Y. J. Hwang, B. K. Min, *J. Phys. Chem. C*, **2015**, 119, 883 - 889.

[121] C. W. Li, J. Ciston, M. W. Kanan, *Nature*, **2014**, 508, 504 – 507.

[122] E. Bertheussen, T. V. Hogg, Y. Abghoui, A. K. Engstfeld, I. Chorkendorff, I. E. L. Stephens, *ACS Energy Lett.*, **2018**, 3, 634 – 640.

[123] R. Chen, H.-Y. Su, D. Liu, R. Huang, X. Meng, X. Cui, Z.-Q. Tian, D. H. Zhang, D. Deng, *Angewandte Chemie*, **2020**, 132, 160 – 166.

[124] K. J. P. Schouten, Z. Qin, E. Pérez Gallent, M. T. M. Koper, *J. Am. Chem. Soc.*, **2012**, 134, 9864 – 9867.

[125] A. A. Peterson, F. Abild-Pedersen, F. Studt, J. Rossmeisl, J. K. Nørskov, *Energy Environ. Sci.*, **2010**, 3, 1311 - 1315.

[126] M. Ma, K. Djanashvili, W. A. Smith, *Angewandte Chemie*, **2016**, 55, 6680 – 6684.

[127] I. V. Chernyshova, P. Somasundaran, S. Ponnurangam, *Proc. Natl. Acad. Sci. U.S.A.*, **2018**, 115, E9261 - E9270.

[128] D. Ren, Y. Deng, A. D. Handoko, C. S. Chen, S. Malkhandi, B. S. Yeo, ACS Catal., **2015**, 5, 2814 - 2821.

[129] G.-R. Zhang, S.-D. Straub, L.-L. Shen, Y. Hermans, P. Schmatz, A. M. Reichert, J. P. Hofmann, I. Katsounaros, B. J. M. Etzold, *Angew. Chem. Int. Ed.*, **2020**, 59, 18095 – 18102.

8. Appendix

8.1. List of chemicals and consumables

The following chemicals and materials were used during this work:

Table 1: Chemicals and materials used in this work.

Substance/Item	**Specification**	**Manufacturer**
Water	1.1 µS/cm, Ph. Eur., USP, NF, purified	VWR Chemicals
Potassium carbonate	99.995 %	Alfa Aesar
Maleic acid	99 %	Arcos Organics
Sulfuric acid	96 %	Merck
Iso-propanol	99.9 %	Carl Roth
Ortho-phosphoric acid	85 %	Merck
Copper sulfate pentahydrate	99.999 %	Alfa Aesar
Dimethyl viologen chloride hydrate	98 %	Arcos Organics
Sodium sulfate decahydrate	99+ %	Arcos Organics
Hydrogen Peroxide	30 % in water	Fisher Bioreagents
Deuterium oxide	99.9 %	Sigma Aldrich
Silica gel	150 A	Arcos Organics
Carbon dioxide	99.995 %	Westfalen
Argon	99.999 %	Westfalen
Hydrogen	99.999 %	Westfalen
Synthetic Air	99.999 %	Westfalen
Sample gas mixtures (H_2, CO, CH_4, C_2H_4, C_2H_6, C_3H_6, C_3H_8, Xe in CO_2	Volume fractions of 0.1 %. 0.2 % or 0.3 %, all certified	Linde

- *continued* -

Copper plate	1 mm. 99.99 %	Alfa Aesar
Nafion N117		Chemours
Fumapem FAA-3-50		FuMa-Tech
Selemion AMV		AGC Engineering

8.2. Technical drawings of PEEK electrolyzer

For the PEEK electrolyzer with the bottom feed inlet for the cathodic half-cell, the technical drawings are presented (figures 64, 65, 66).

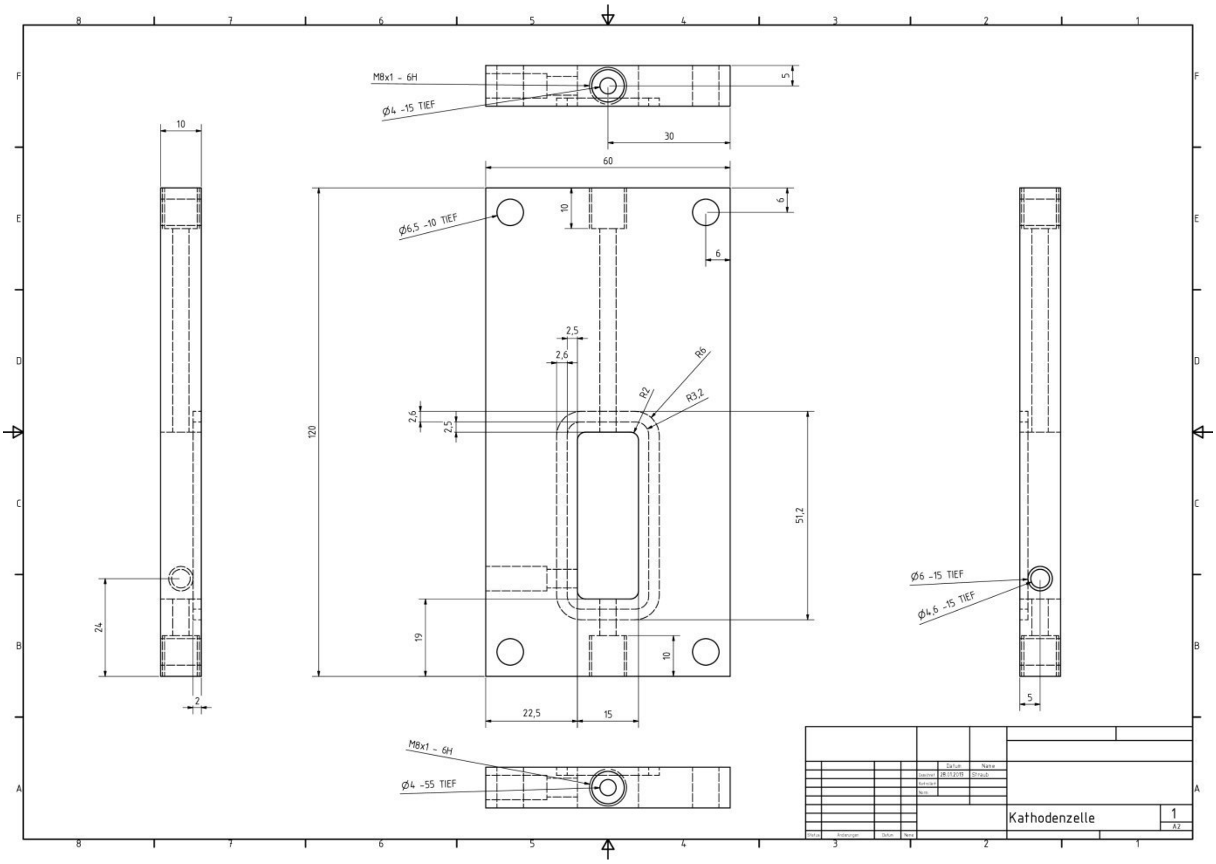

Figure 64: Technical drawing of the cathodic half-cell with bottom feed inlet.

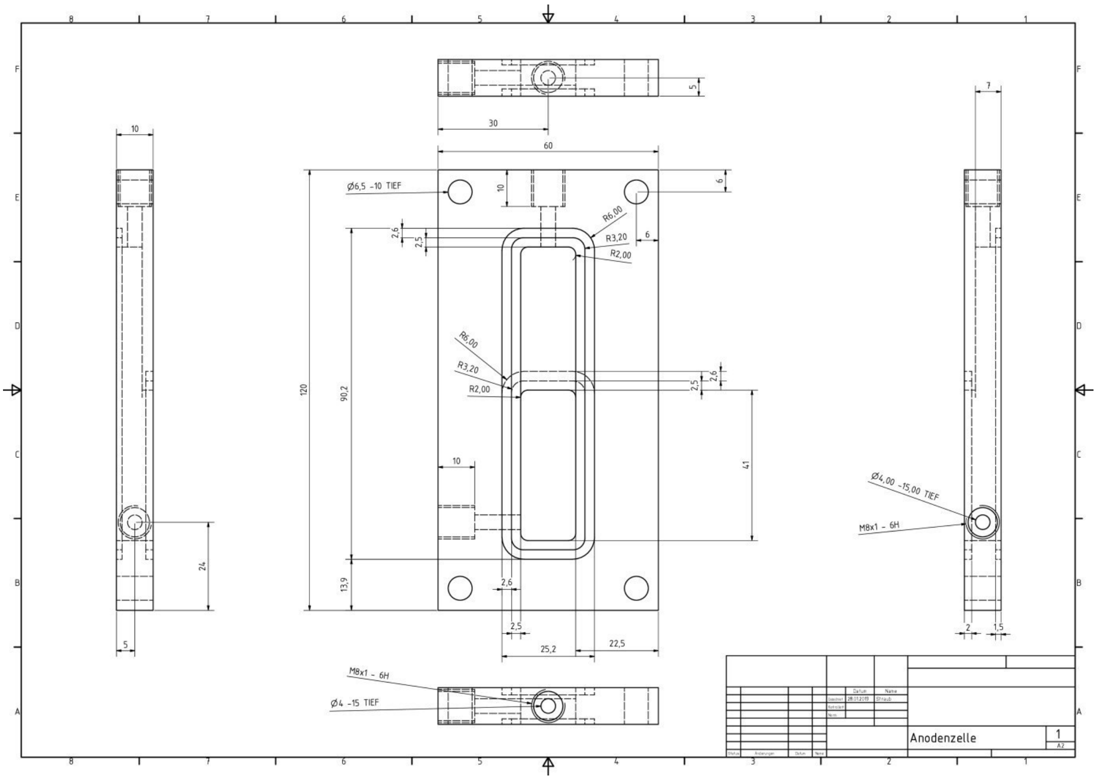

Figure 65: Technical drawing of the anodic half-cell.

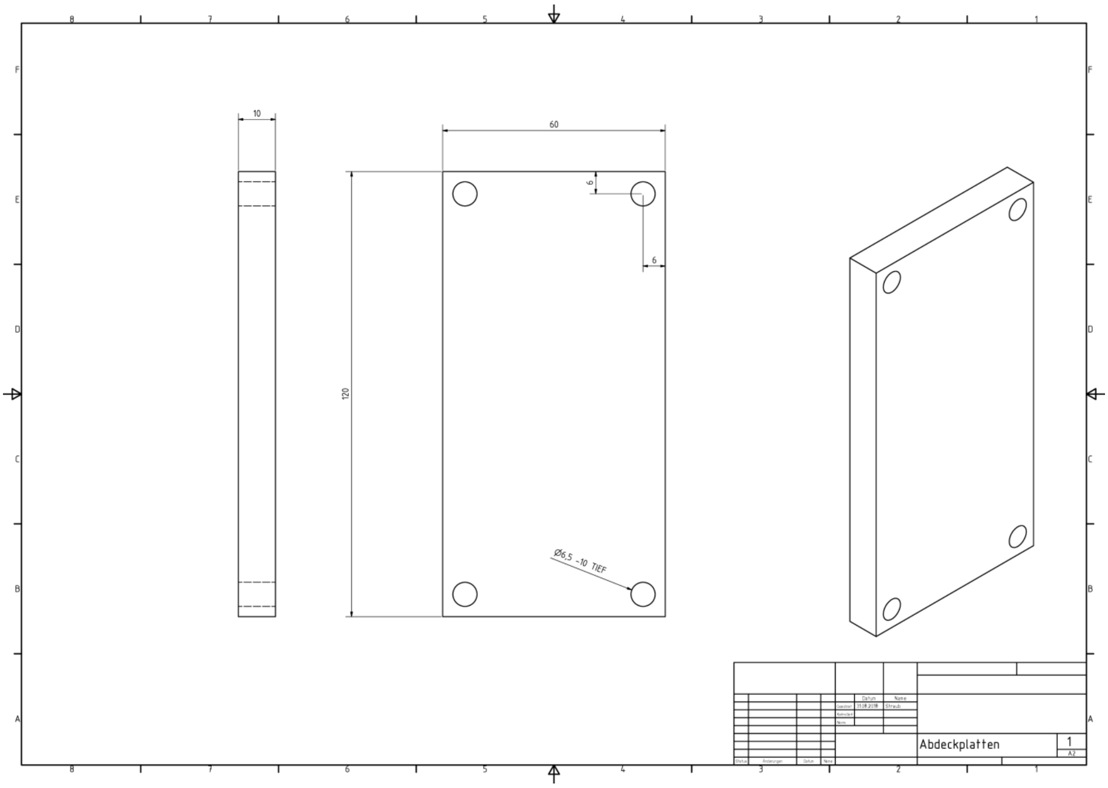

Figure 66: Technical drawing of the fixation plate.

8.3. MFC calibration

MFC's cathode 1 and 2 as well as anode 2 are of the type FG-201CV-AGD-33-V-DA-000 and were bought calibrated by certificate from Bronkhorst. Anode 1 is of the type F201C-FAC-33-V and was calibrated by using a bubble counter, drawn in scheme 22. The bubble counter consists of a scaled glass tube, where at the bottom some soap solution can be brought in contact with the forwarded calibration gas. The MFC is connected to the bottom of the scaled glass tube. For the calibration, the temperature T in °C and the pressure p in mbar were recorded. For the scale parts between 5 % and 70 % established by the MFC controlling box, the time in seconds for a CO_2 bubble to pass through a defined volume V in mL was noted. Each measurement was repeated three times. Out of the arithmetic mean time values t_m in seconds, the normalized volume flux V_N in ml_N/min was calculated by

$$V_N[ml_N/min] = V[ml] \cdot 60 \frac{s}{min} \cdot 273.15\,K \cdot \frac{p[mbar]}{t_m[s] \cdot (T[°C]+273.15)K \cdot 1013.25\,mbar} \qquad \text{(X)}$$

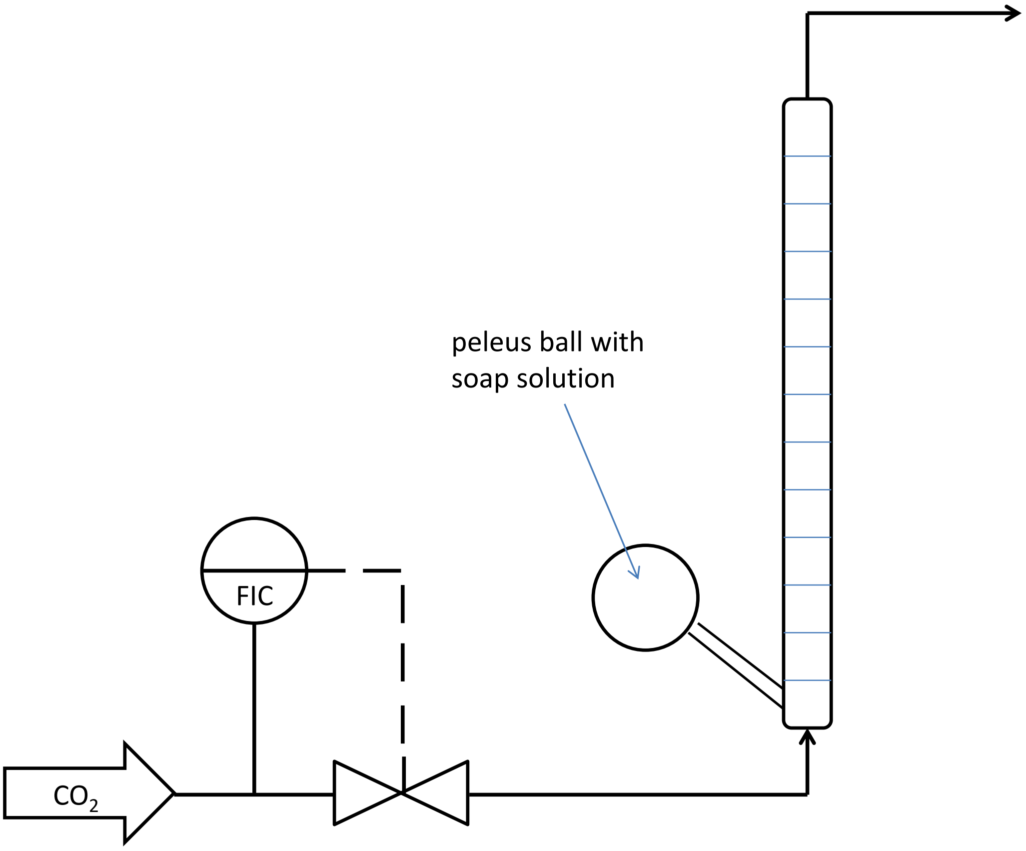

Scheme 22: Experimental set-up for MFC calibration. Bubble counter.

The results are shown in table 2 and figure 67.

Table 2: Experimental data for the calibration of anode 1 with the bubble counter.

SKT [%]	**t_1 [s]**	**t_2 [s]**	**t_3 [s]**	**T [°C]**	**p [mbar]**	**V [ml]**	**t_m [s]**	**V_N [ml_N/min]**
5.0	28.41	30.22	30.15	15	985	1	29.59	1.87
10.0	140.31	139.89	140.13	23	985	10	140.11	3.84
20.0	71.10	70.52	69.86	23	985	10	70.49	7.63
30.0	46.21	46.39	46.11	23	985	10	46.24	11.64
40.0	35.33	35.10	36.01	15	985	10	35.48	15.58
50.0	28.15	28.03	28.12	15	985	10	28.10	19.68
60.0	23.83	24.18	24.09	15	985	10	24.03	23.01
70.0	20.56	21.32	20.73	15	984	10	20.87	26.47

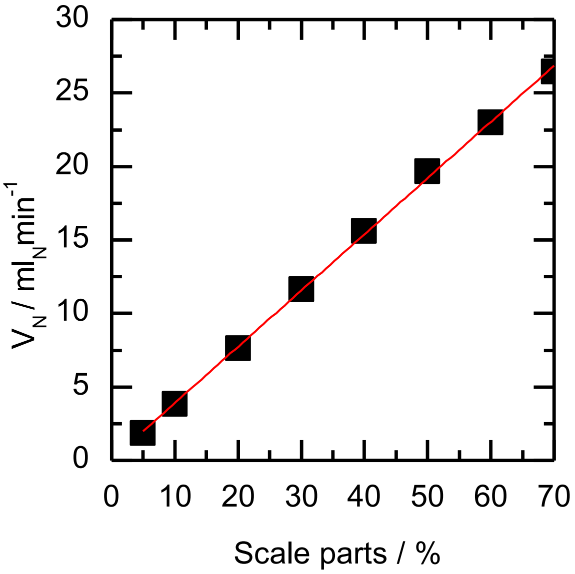

Figure 67: Calibration curve for anode 1.

8.4. GC calibration

The online GC was calibrated by installing three different sample gas mixtures of H_2, CO, CH_4, C_2H_4, C_2H_6, C_3H_6 and C_3H_8 in CO_2 matrix with 0.1 v-% Xe in different concentrations described in table 1. The components propene, propane, carbon dioxide and xenon were not calibrated. The sample gas mixtures were flown with the MFC's cathode 1 to the GC measured with the protocol described in the experimental section with an extended measuring method (Calibration_Ar). Each concentration was measured four times and the arithmetic mean was calculated for the measured peak area. The retention times, the concentration in v-%, the peak area and the standard deviation of the peak area of the gas phase components are given in table 3.

Table 3: Retention times, concentration in v-%, peak area and standard deviation of the peak are of the gas phase components H_2, CO, CH_4, C_2H_4 and C_2H_6.

Component	**Retention time [min]**	**concentration [v-%]**	**Peak area [-]**	**Standard deviation [-]**
Hydrogen	1.57	0.094	13357.25	1089.50
		0.196	28761.75	1676.17
		0.298	43247.50	3913.12
Carbon monoxide	2.31	0.103	1341.00	26.09
		0.206	2691.50	143.54
		0.300	3829.50	245.87
Methane	3.16	0.100	2938458.75	75410.66
		0.201	5885892.00	201296.73
		0.299	8698123.75	614478.59
Ethylene	8.03	0.099	5618426.75	129915.25
		0.189	10760745.50	322831.89
		0.339	19154488.25	1663890.44
Ethane	8.99	0.103	5956514.00	118093.78
		0.203	11818867.75	359907.70
		0.303	17521039.50	1167210.22

Plotting the arithmetic mean of the measured peak areas against the volume fraction gives the calibration curve for each gas, depicted in figure 68.

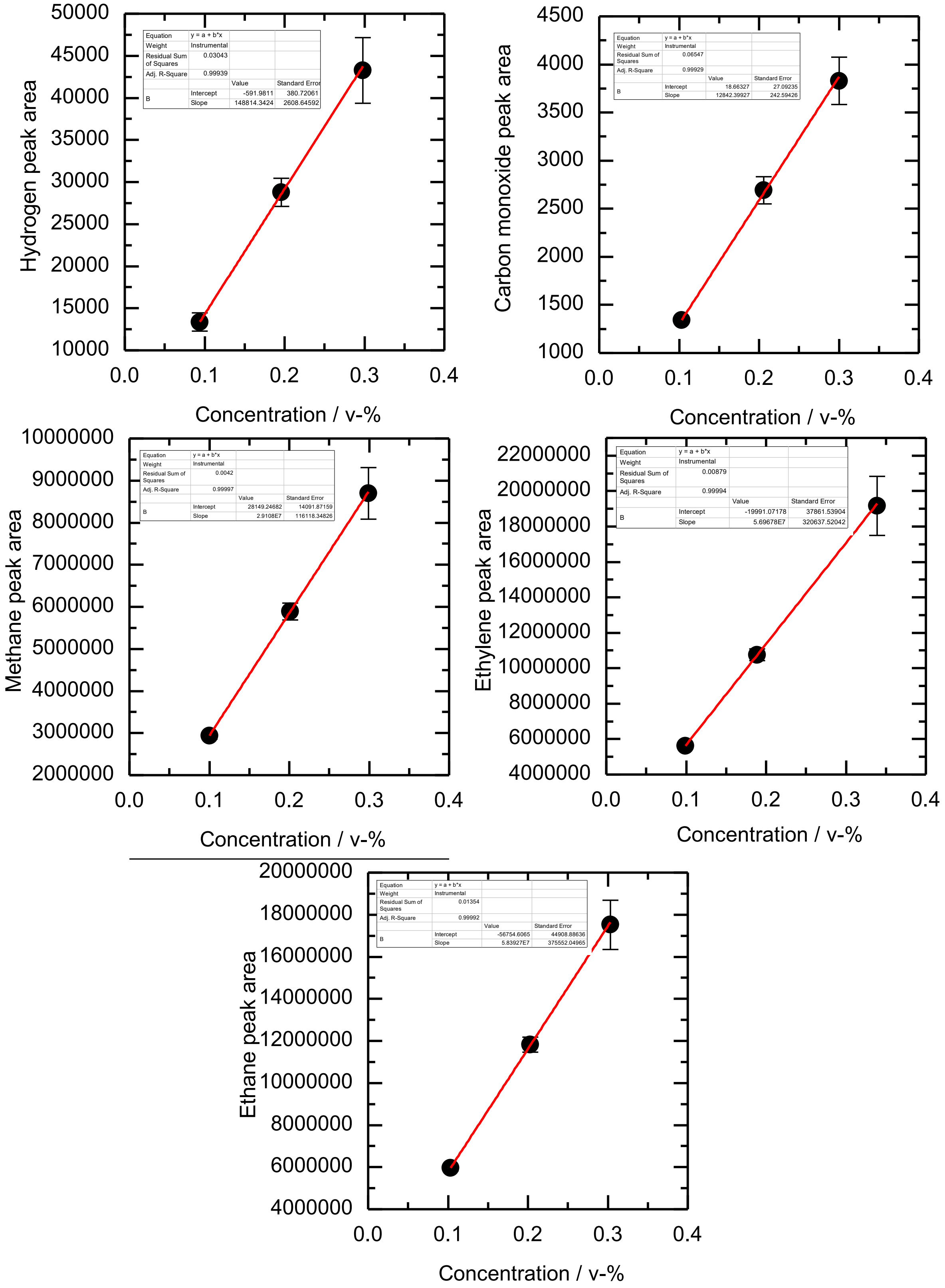

Equation	y = a + b*x		
Weight	Instrumental		
Residual Sum of Squares	0.03043		
Adj. R-Square	0.99939		
		Value	Standard Error
B	Intercept	-591.9811	380.72061
	Slope	148814.3424	2608.64592

Equation	y = a + b*x		
Weight	Instrumental		
Residual Sum of Squares	0.06547		
Adj. R-Square	0.99929		
		Value	Standard Error
B	Intercept	18.66327	27.09235
	Slope	12842.39927	242.59426

Equation	y = a + b*x		
Weight	Instrumental		
Residual Sum of Squares	0.0042		
Adj. R-Square	0.99997		
		Value	Standard Error
B	Intercept	28149.24682	14091.87159
	Slope	2.9108E7	116118.34826

Equation	y = a + b*x		
Weight	Instrumental		
Residual Sum of Squares	0.00879		
Adj. R-Square	0.99994		
		Value	Standard Error
B	Intercept	-19991.07178	37861.53904
	Slope	5.69678E7	320637.52042

Equation	y = a + b*x		
Weight	Instrumental		
Residual Sum of Squares	0.01354		
Adj. R-Square	0.99992		
		Value	Standard Error
B	Intercept	-56754.6065	44908.88636
	Slope	5.83927E7	375552.04965

Figure 68: Calibration curves for H_2, CO, CH_4, C_2H_4 and C_2H_6 with appropriate linear regression.

8.5. Reference electrode calibration

Ag/AgCl (3M NaCl) reference electrodes from C3 Analytics (RE-1S) were calibrated by the following protocol. A 3 neck bottle was filled with a saturated potassium chloride electrolyte with a pH of 7. The Ag/AgCl reference electrode was used as working electrode and a silver wire as counter electrode. The experimental section is shown in scheme 23.

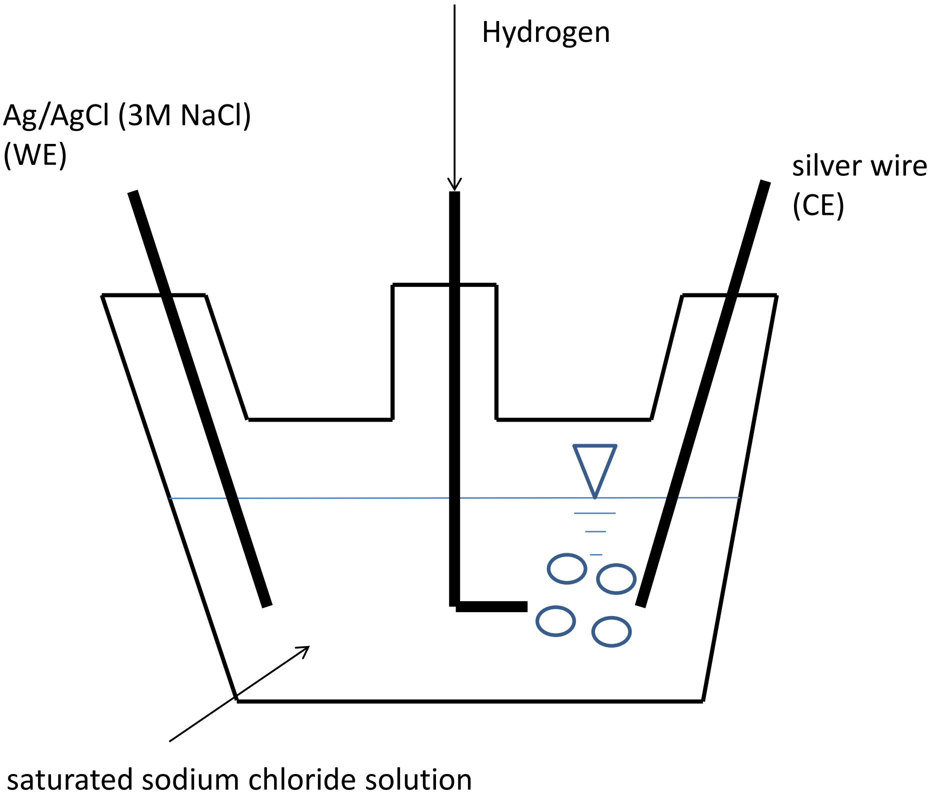

Scheme 23: Experimental set-up for the calibration of the reference electrodes.

The electrolyte was purged for 30 min with hydrogen. With continuing hydrogen flow, the open circuit potential (OCP) was recorded until it was stable. This value was used for the potential conversion von Ag/AgCl to RHE described in the experimental section. The measured values for the different reference elctrodes were always around 600 mV.

8.6. Copper foam synthesis

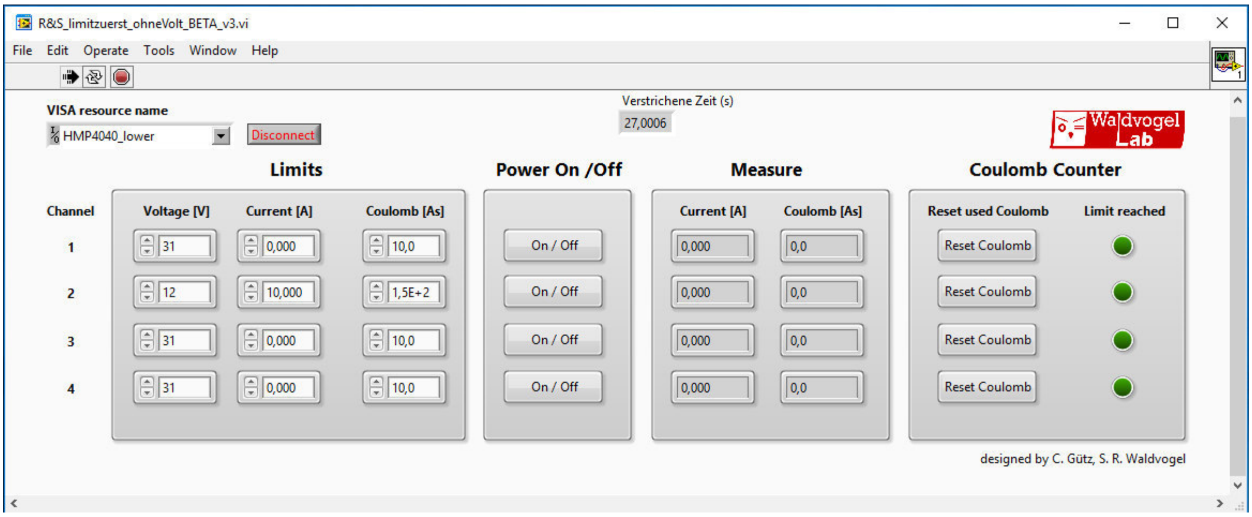

R&S_limitzuerst_ohneVolt_BETA_v3.vi

VISA resource name: HMP4040_lower

Verstrichene Zeit (s): 27,0006

	Limits			Measure	
Channel	Voltage [V]	Current [A]	Coulomb [As]	Current [A]	Coulomb [As]
1	31	0,000	10,0	0,000	0,0
2	12	10,000	1,5E+2	0,000	0,0
3	31	0,000	10,0	0,000	0,0
4	31	0,000	10,0	0,000	0,0

Figure 69: LabView interface for the copper foam deposition process.

Table 4: Deposited mass m of different copper foam materials.

Foam catalyst	**Deposited mass m [µg]**
CuF-SO4-15	43.2 ± 3.8
CuF-SO4-15-200	45.4 ± 4.3
CuF-SO4-15-500	44.5 ± 3.9
CuF-SO4-15-1200	46.8 ± 2.4
CuF-SO4-40	53.6 ± 9.4
CuF-SO4-60	75.9 ± 12.5

The copper foam materials are named in the following manner. The **CuF-SO4** indicates a copper foam material, which is synthesized in a copper sulfate containing deposition solution. The first number indicates 1/10th of the established coulombs during the deposition process. The second number indicates the stirring speed in rpm established for the electrodeposition process.

Figure 70: Instrument for copper foam thickness measurement.

Table 5: Foam thickness d_F, pore size dp and web width ds of different copper foam catalysts.

Foam catalyst	**d_F [µm]**	**d_P [µm]**	**d_S [µm]**
CuF-SO4-15	47.6 ± 6.4	28.4 ± 3.1	14.8 ± 3.0
CuF-SO4-15-200	69.1 ± 9.6	45.8 ± 5.6	22.1 ± 4.8
CuF-SO4-15-500	66.1 ± 9.4	62.1 ± 5.4	42.1 ± 7.0
CuF-SO4-15-1200	67.7 ± 9.1	75.8 ± 9.7	47.9 ± 8.8
CuF-SO4-40	60.6 ± 8.5	54.4 ± 10.2	40.4 ± 6.6
CuF-SO4-60	87.8 ± 12.1	99.4 ± 9.5	61.1 ± 12.9

8.7. Electrochemical active surface (ECAS) by methyl viologen method

8.7.1. Determination of diffusion coefficient with copper plate

The diffusion coefficient was determined with the methylviologen method described in the experimental section under the assumption of an R_f of one for the copper plate and thus the usablility of the Randles-Sevcik equation. The CV curves at different scanning rates and the Randles-Sevcik plot for the pristine copper plate are drawn in figure 71.

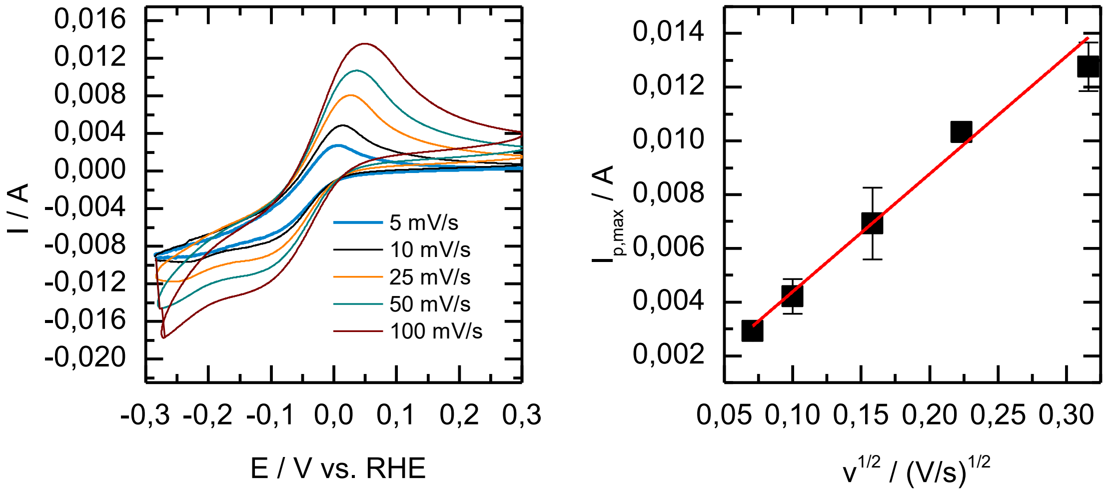

Figure 71: Cyclovoltammetry curves at different scan rates (left) and Randles-Sevcik plot (right) for the pristine copper plate.

The diffusion coefficient of methyl viologen was determined to $D = 2.05 \cdot 10^{-6}\ \frac{\mathrm{cm}^2}{\mathrm{s}} \pm 2.13 \cdot 10^{-7}\ \frac{\mathrm{cm}^2}{\mathrm{s}}$.

8.7.2. Determination of ECAS for copper foam catalysts and IL impregnated catalysts

With the method described in the previous chapter, the electrochemical surface area (ECAS) is determined via the Randles-Sevcik plots. The CV and the Randles-Sevcik plots for the different pristine copper foam materials and the IL impregnated copper foam materials are given in figures 72, 73, 74. The determined ECAS for the different copper foam materials are given in table 6.

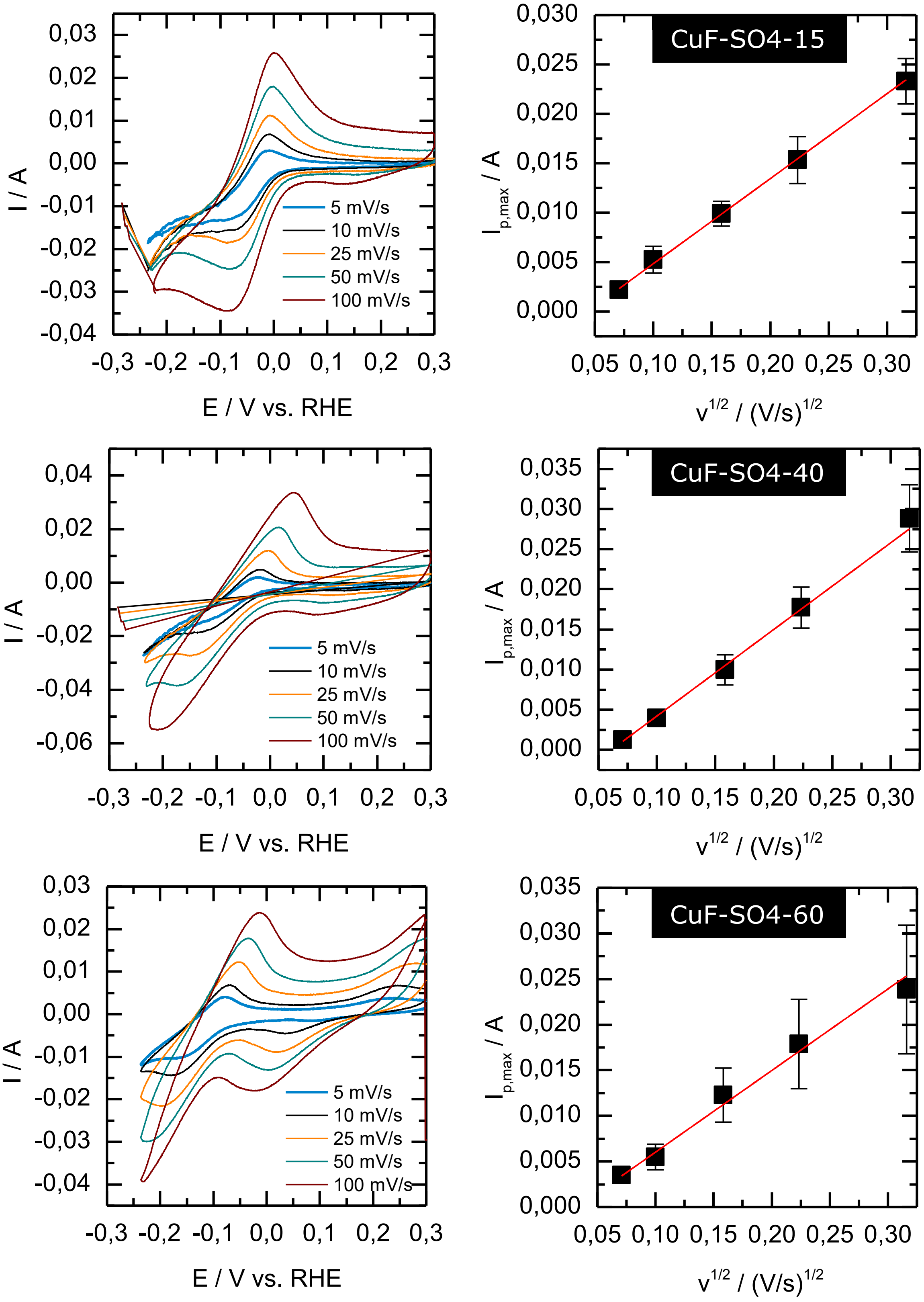

Figure 72: Cyclovoltammetry curves at different scan rates (left) and Randles-Sevcik plot (right) for CuF-SO4-15, CuF-SO4-40 and CuF-SO4-60.

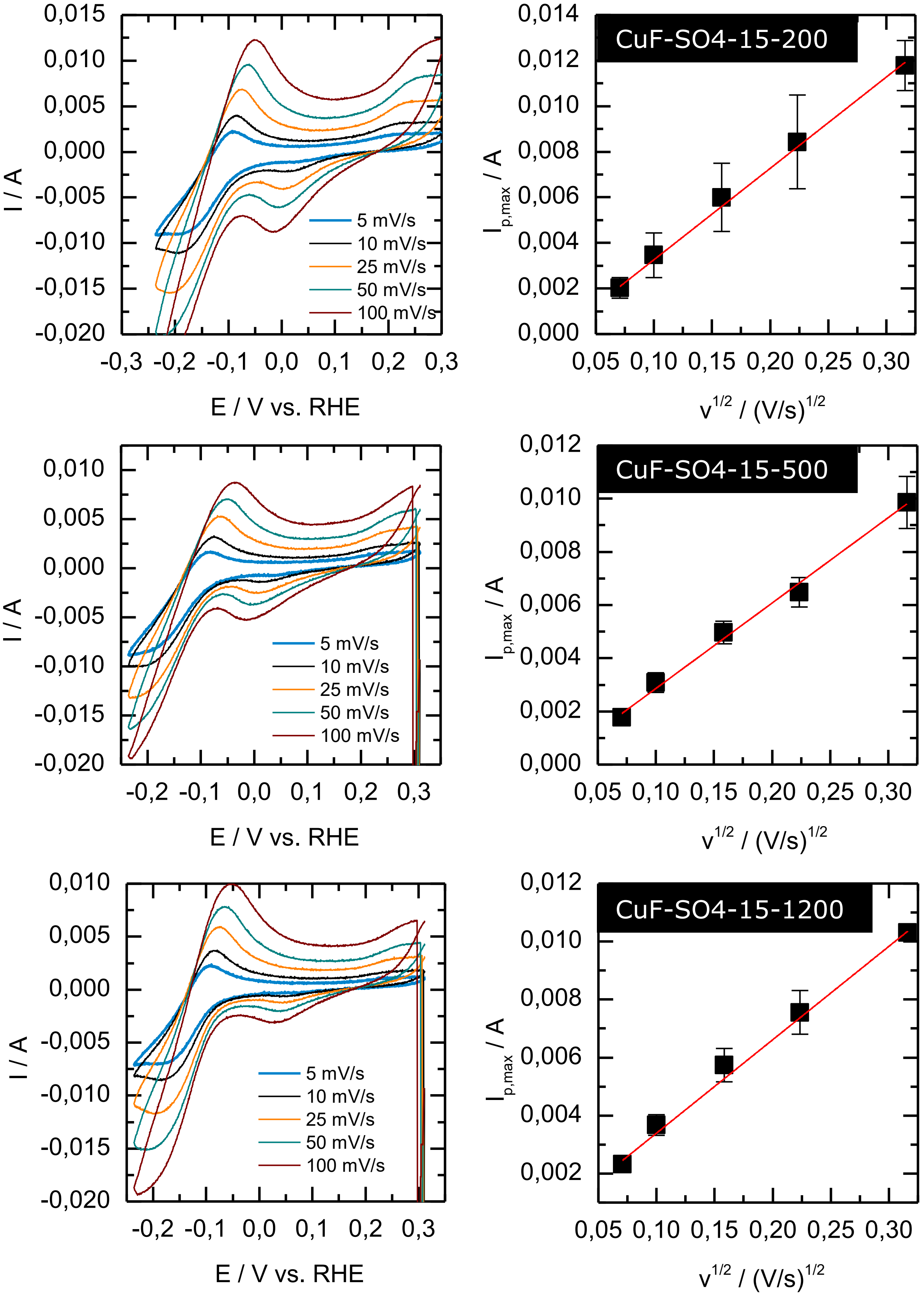

Figure 73: Cyclovoltammetry curves at different scan rates (left) and Randles-Sevcik plot (right) for CuF-SO4-15-200, CuF-SO4-15-500 and CuF-SO4-15-1200.

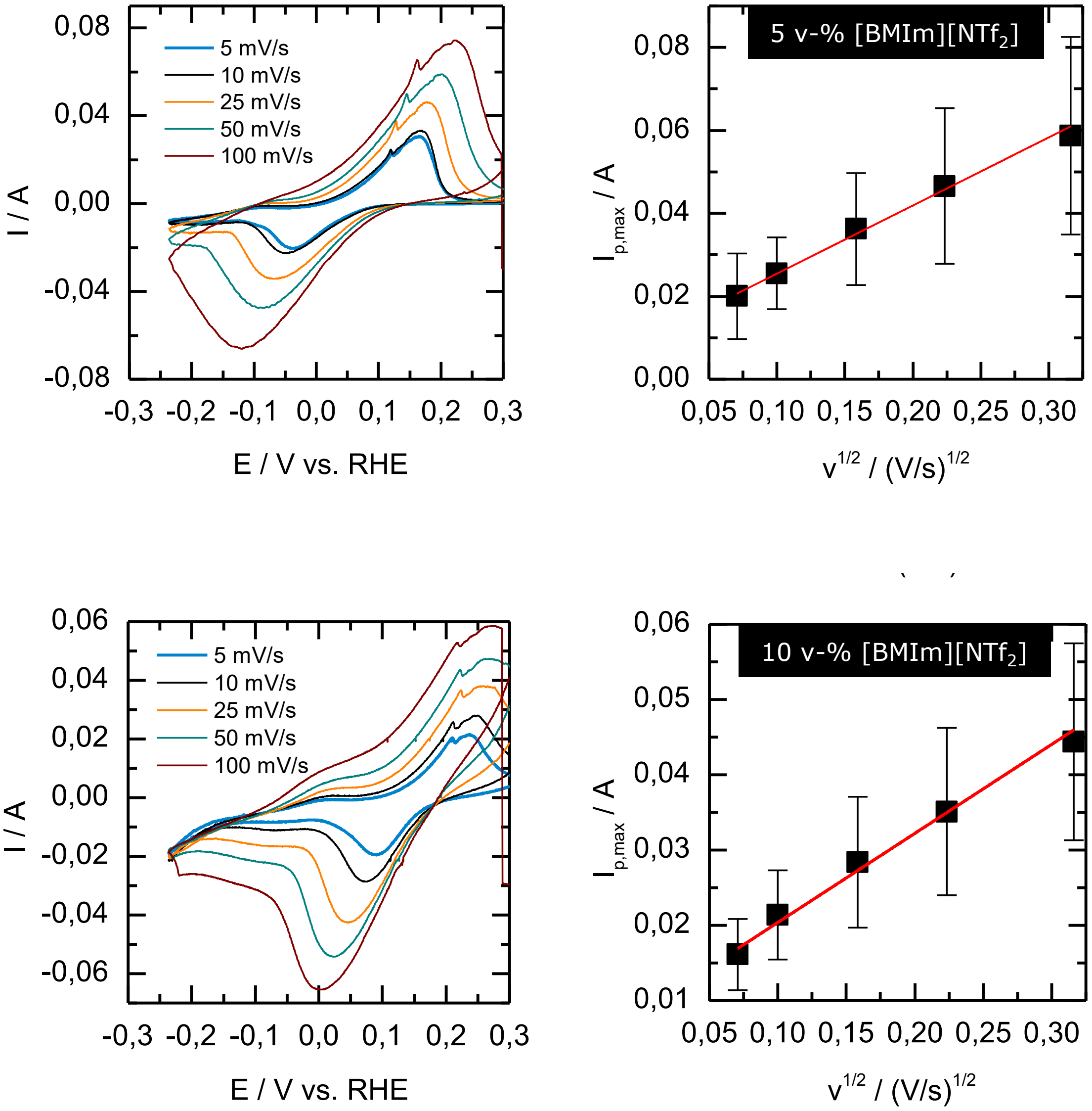

Figure 74: Cyclovoltammetry curves at different scan rates (left) and Randles-Sevcik plot (right) for SCILL-15(5)[BMIm][NTf$_2$] and SCILL-15(10)[BMIm][NTf$_2$].

Table 6: Electrochemical active surface (ECAS) and roughness factor (R_f) determined by the methyl viologen method for different copper foam catalysts and IL impregnated catalysts.

	ECAS [cm^2]	R_f
Cu plate	5.7	1
CuF-SO4-15	22.4 ± 4.4	3.9 ± 0.8
CuF-SO4-15-200	10.4 ± 1.0	1.8 ± 0.2
CuF-SO4-15-500	8.36 ± 0.7	1.5 ± 0.1
CuF-SO4-15-1200	8.37 ± 0.5	1.5 ± 0.1
CuF-SO4-40	28.0 ± 7.8	4.9 ± 1.4
CuF-SO4-60	23.3 ± 0.8	4.1 ± 0.2
SCILL-15(5)[BMIm][NTf_2]	42.8 ± 6.8	7.5 ± 1.2
SCILL-15(10)[BMIm][NTf_2]	30.8 ± 9.5	5.4 ± 1.7

8.8. Electrochemical reduction of CO_2

8.8.1. Experimental protocol adapted for the PEEK reactor

Each experiment started after purging the electrolyte for 30 min with CO_2 at the established flow rate with a pre EIS measurement (figure 75) in the frequency range between 10000 to 0.01 Hz at an applied potential of -1.7 V vs. Ag/AgCl (3M NaCl). All measurements were done with a PARSTAT multichannel potentiostat and controlled by the VersaStudio software.

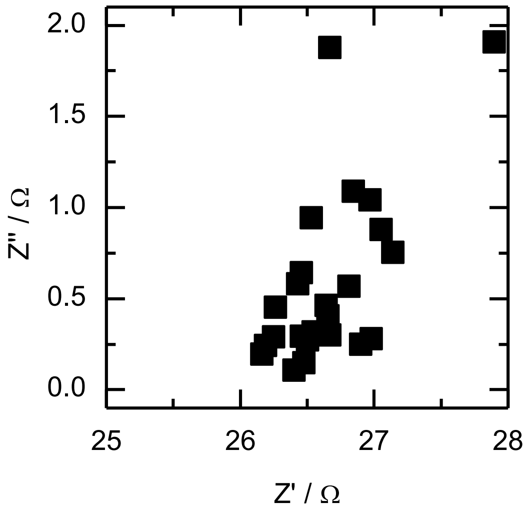

Figure 75: Nyquist plot of the pre EIS measurement for the example of CuF-SO4-15.

The pre impedance measurement is followed by a pretreating CV measurement for five cycles. The last cycle for CuF-SO4-15 is depicted in figure 76. Here, no iR-compensation was used. The potential range was chosen between -0.5 to -1.8 V vs. Ag/AgCl (3M NaCl) with a scan rate of 0.2 V/s.

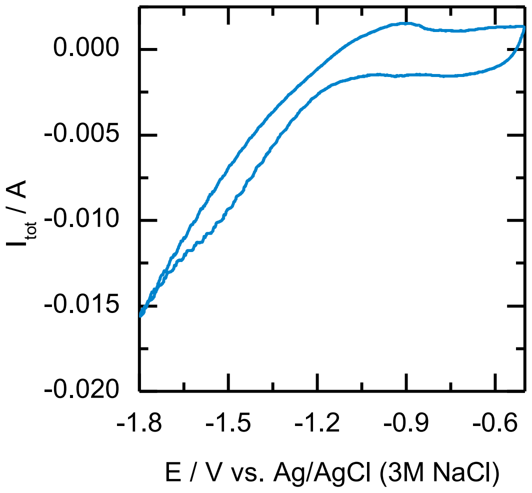

Figure 76: 5th cycle of the pretreatment CV at a scan rate of 0.2 V/s. Example from CuF-SO4-15.

Then, a pre LSV measurement is done in the potential range between 0 and -1.7 V vs. Ag/AgCl (3M NaCl) at a scan rate of 0.2 V/s (figure 77).

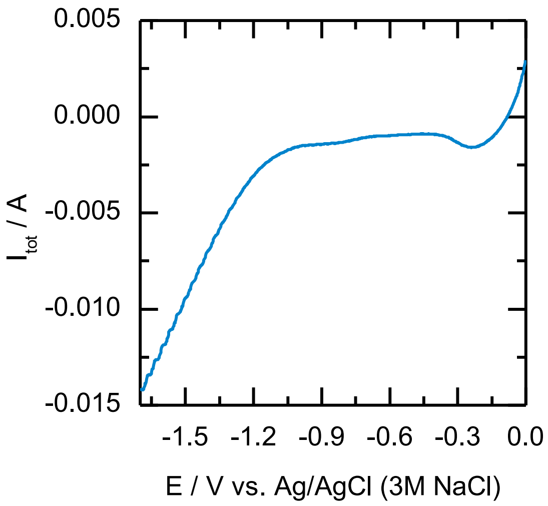

Figure 77: Pre LSV curve at 0.2 V/s. Example from CuF-SO4-15.

Then the post EIS was measured in the frequency range of 100 to 0.01 Hz at a potential of -0.9 V vs. Ag/AgCl (3M NaCl). The solution resistance here was determined at the point, where Z'' is zero ohms (figure 78).

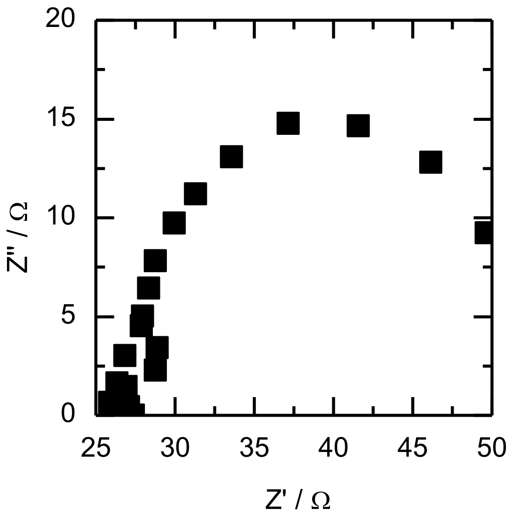

Figure 78: Nyquist plot for the post EIS. Example from CuF-SO4-15.

With the iR compensation described in the experimental section, chronoamperometry curves at different applied potentials were recorded over 1 h. Shown in the following figures 79 to 88 are the normalizes current densities in mA/cm^2 (geometric surface area: 1 cm^2). Also the iR corrected potentials are given according to the calculation given in the experimental section. Here, the chronoamperometry curves will be given for all used catalysts.

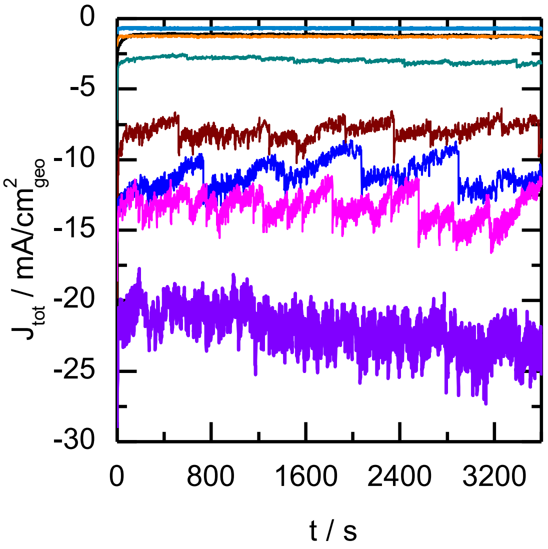

Figure 79: Chronoamperometry curves for CuF-SO4-15 at -0.55 V (light blue), -0.59 V (black), -0.65 V (orange), -0.7 V (cyan), -0.76 V (brown), -0.8 V (dark blue), -0.85 V (rose) and -0.91 V (purple). All potentials against RHE.

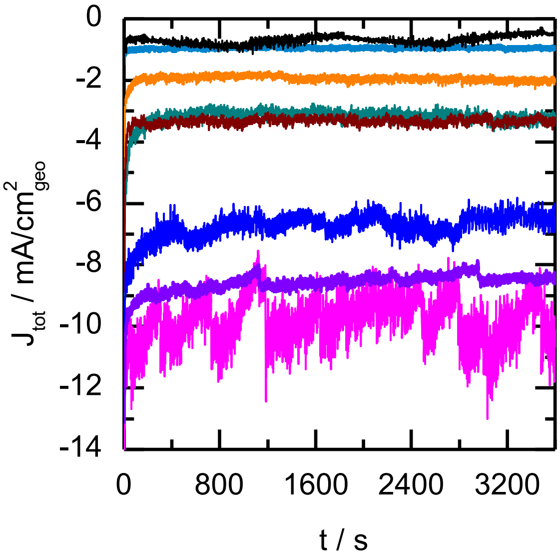

Figure 80: Chronoamperometry curves for CuF-SO4-15-200 at -0.55 V (light blue), -0.61 V (black), -0.65 V (orange), -0.71 V (cyan), -0.75 V (brown), -0.81 V (dark blue), -0.86 V (rose) and -0.89 V (purple). All potentials against RHE.

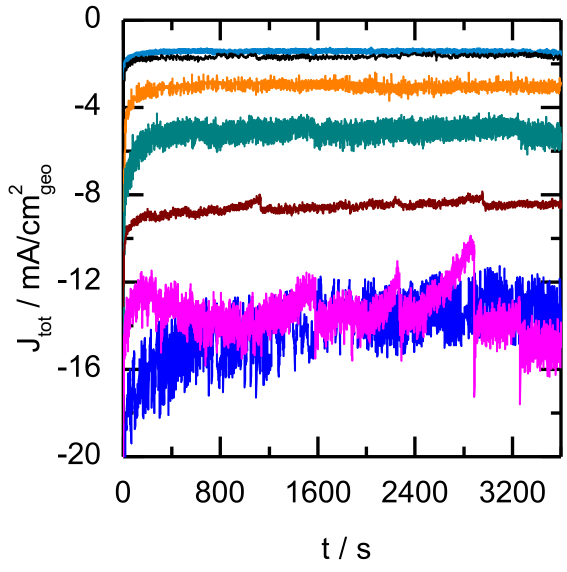

Figure 81: Chronoamperometry curves for CuF-SO4-15-500 at -0.55 V (light blue), -0.61 V (black), -0.65 V (orange), -0.71 V (cyan), -0.75 V (brown), -0.81 V (dark blue), -0.86 V (rose) and -0.89 V (purple). All potentials against RHE.

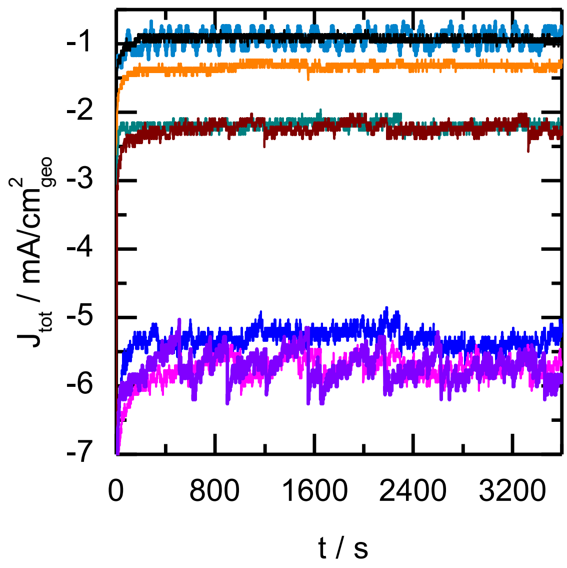

Figure 82: Chronoamperometry curves for CuF-SO4-15-1200 at -0.55 V (light blue), -0.61 V (black), -0.65 V (orange), -0.71 V (cyan), -0.75 V (brown), -0.81 V (dark blue), -0.86 V (rose) and -0.89 V (purple). All potentials against RHE.

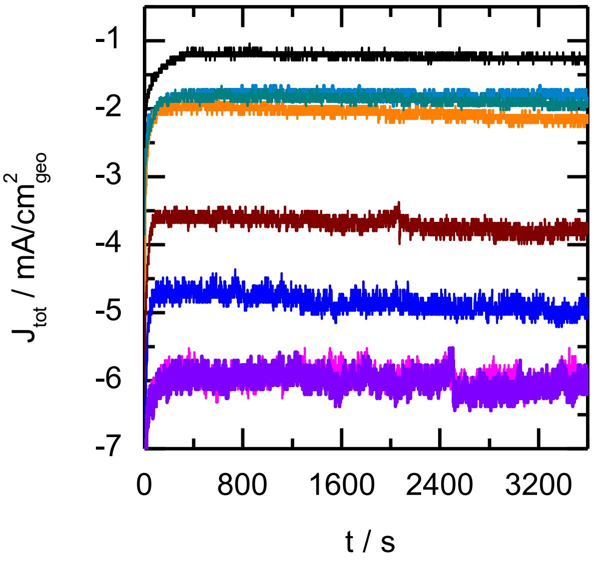

Figure 83: Chronoamperometry curves for CuF-SO4-40 at -0.55 V (light blue), -0.60 V (black), -0.65 V (orange), -0.70 V (cyan), -0.74 V (brown), -0.78 V (dark blue), -0.83 V (rose) and -0.87 V (purple). All potentials against RHE.

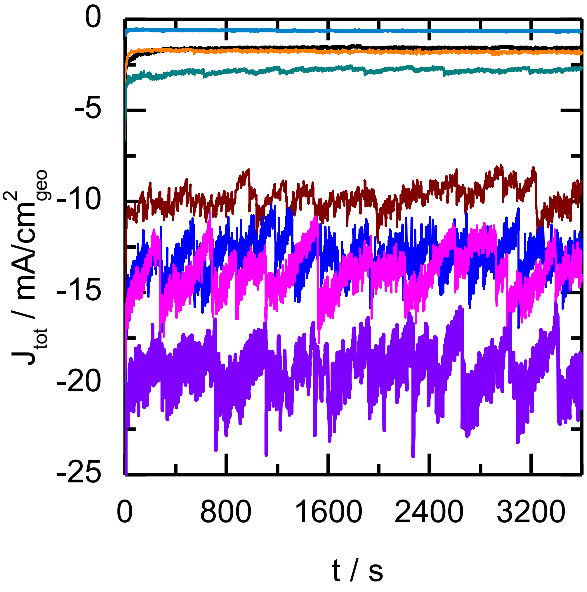

Figure 84: Chronoamperometry curves for SCILL-15(5)[BMIm][NTf$_2$] at -0.55 V (light blue), -0.60 V (black), -0.65 V (orange), -0.70 V (cyan), -0.75 V (brown), -0.80 V (dark blue), -0.85 V (rose) and -0.91 V (purple). All potentials against RHE.

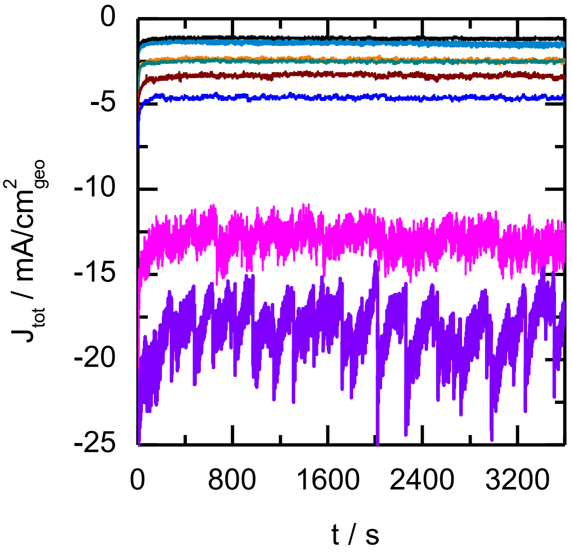

Figure 85: Chronoamperometry curves for SCILL-15(5)[BMMIm][NTf$_2$] at -0.52 V (light blue), -0.56 V (black), -0.58 V (orange), -0.62 V (cyan), -0.67 V (brown), -0.70 V (dark blue), -0.82 V (rose) and -0.88 V (purple). All potentials against RHE.

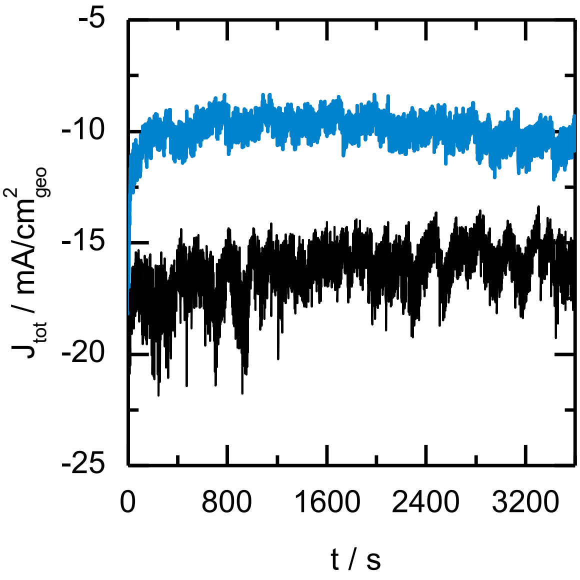

Figure 86: Chronoamperometry curves for 5v-%[BMIm][NTf$_2$] (blue) and 5v-%[BMIm][OTf] (black) at -0.81 V vs. RHE.

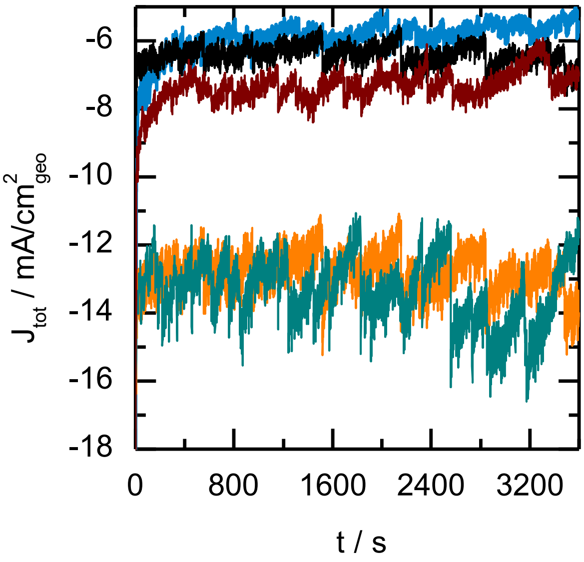

Figure 87: Chronoamperometry curves for CuF-SO4-15 at different CO_2 flow rates at -0.85 V vs. RHE. 5 ml/min (blue), 10 ml/min (black), 20 ml/min (orange), 30 ml/min (cyan), 40 ml/min (brown).

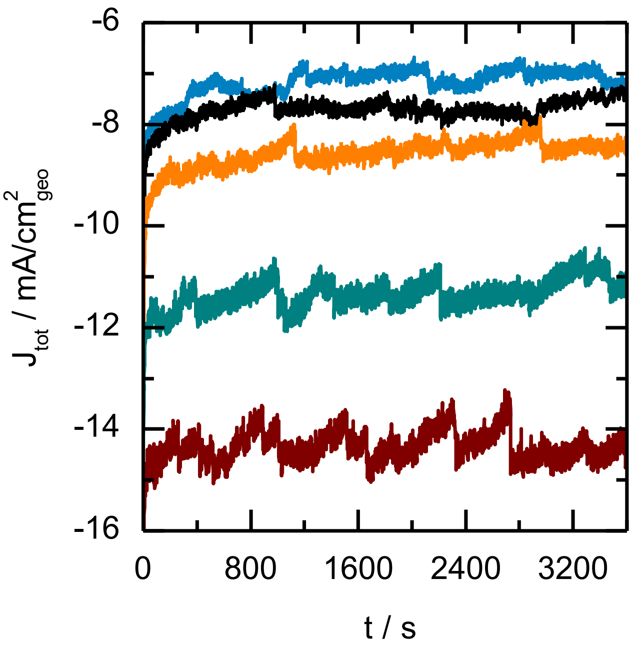

Figure 88: Chronoamperometry curves for CuF-SO4-15 without substrate pretreatment at -0.80 V (light blue), -0.84 V (black), -0.91 V (orange), -0.94 V (cyan), -1.05 V (brown). All potentials against RHE.

After the chronoamperometry measurement, a final end EIS was measured with the same parameters set up for the post impedance. The resulting Nyquist plot is shown in figure 89.

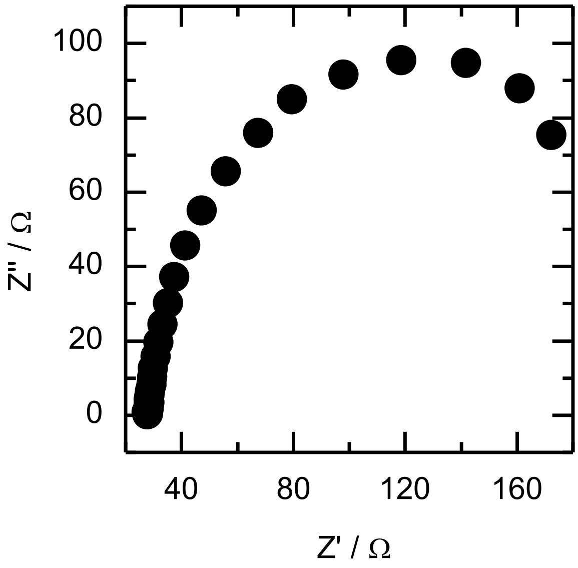

Figure 89: Nyquist plot of the end EIS. Example from CuF-SO4-15.

Finally, a LSV (End LSV) with the same parameters like for the Pre LSV was conducted (figure 90).

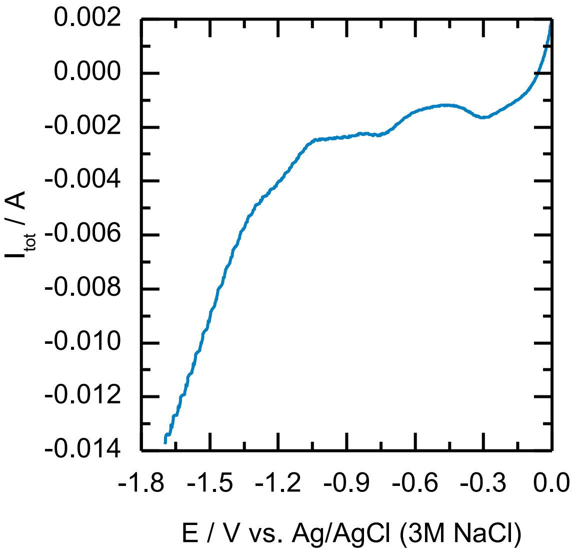

Figure 90: End LSV curve at a scan rate of 0.2 V/s. Example from CuF-SO4-15.

8.8.2. H-type glass cell

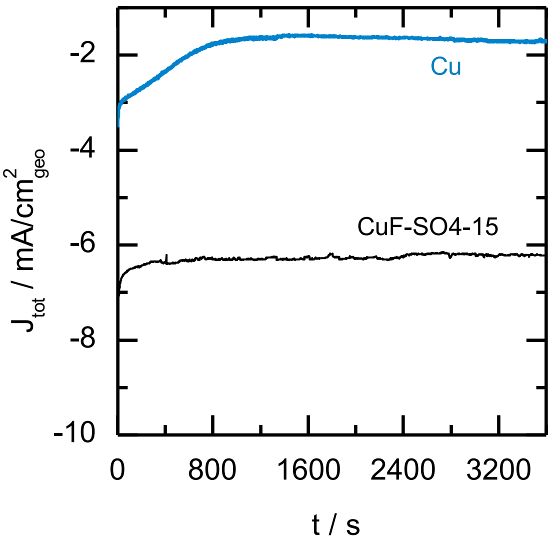

Figure 91: Chronoamperometry curves for Cu plate and CuF-SO4-15 at -1.0 V vs. RHE.

8.8.3. Analytical procedure and calculations

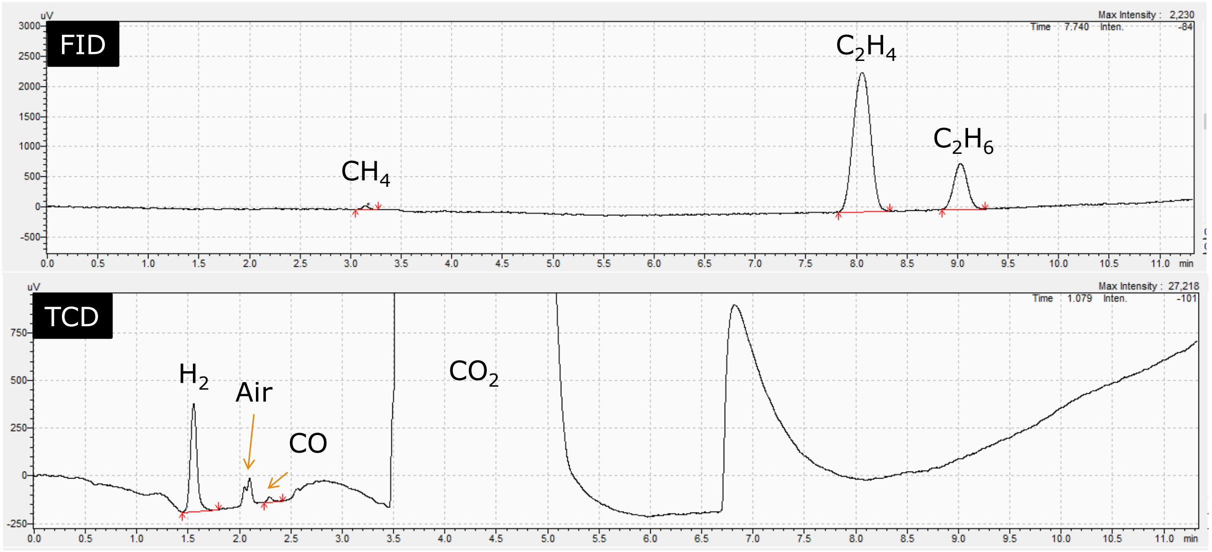

Figure 92: Online GC chromatograms obtained for the example of CuF-SO4-15 at -0.85 V vs. RHE. FID (top) and TCD (bottom).

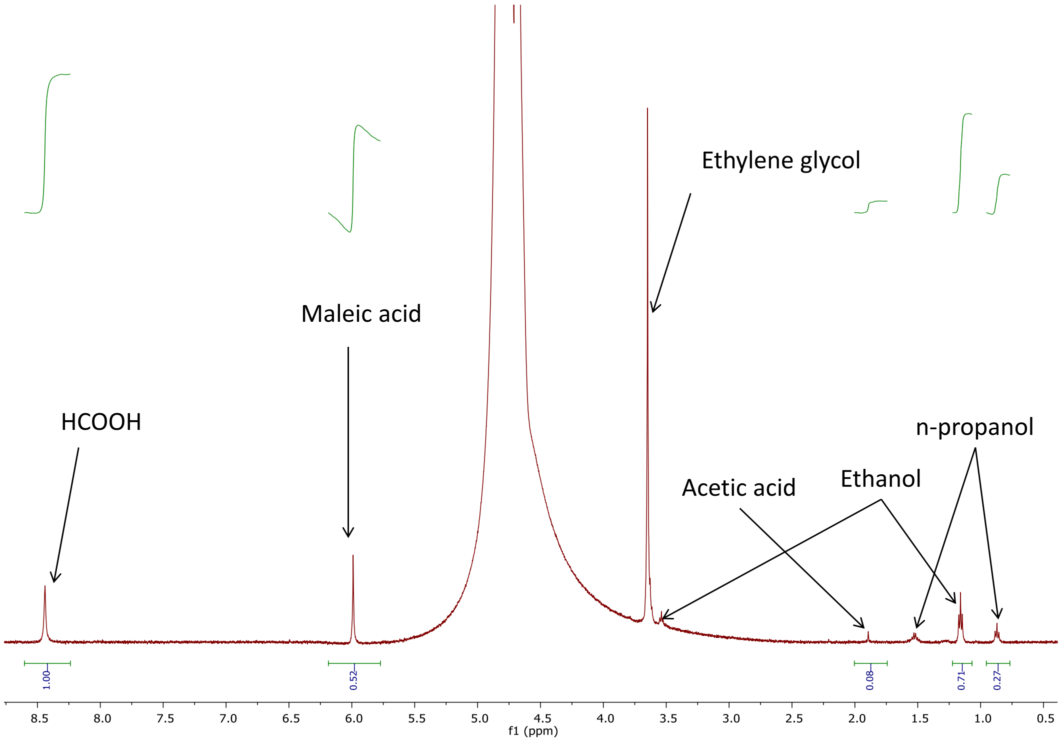

Figure 93: Water suppressed ^{1}H-NMR spectrum for the example of CuF-SO4-15 at -0.85 V vs. RHE.

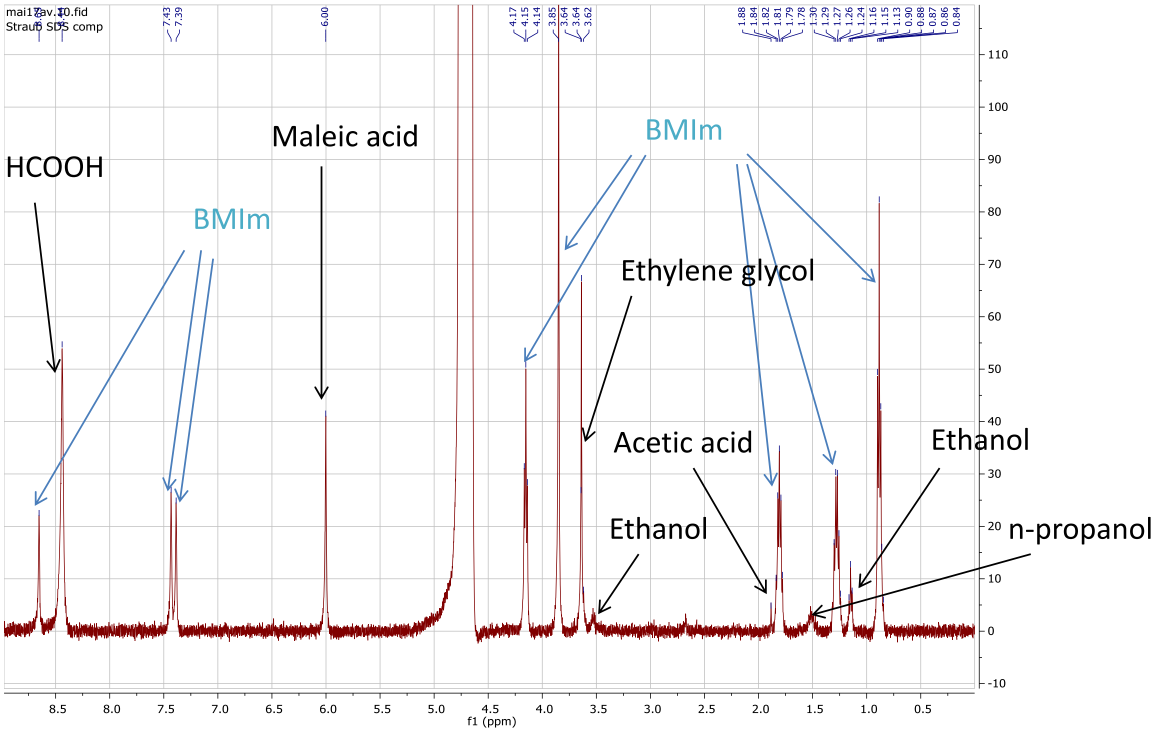

Figure 94: Water suppressed ^{1}H-NMR spectrum for a mixture of detected liquid phase products and [BMIm][NTf$_2$].

Table 7: ^{1}H-NMR chemical shifts of detected components.

Compound	**Chemical shift [ppm]**
n-propanol	0.88, 1.51
ethanol	1.15, 3.53
Acetic acid	1.88
Ethylene glycol	3.64
Maleic acid	6.0
Formic acid	8.43

For the calculation of the gas phase FE, the Excel template depicted in figure 95 was used. Out of the measured GC peak integrals (Int), the volume fraction (v-%) was determined by the appropriate calibration function for each component. The ppm was calculated by multiplying the volume fraction with a factor of 10000. With the CO_2 flow rate in m^3/s, the transferred number of electrons z of the appropriate component, the faraday constant F = 96485 As/mol, the atmospheric pressure p = 100000 Pa, the universal gas constant R = 8.314 J/(mol*K) and the room temperature T = 298.15 K, the CO_2 flow rate in mol/s and the partial current I_i of the appropriate component could be calculated by

$$\dot{n}_{CO_2}[mol/s] = \frac{p[Pa] \cdot V_{CO_2}[m^3/s]}{R[J/(mol \cdot K)] \cdot T[K]} \tag{XI}$$

$$I_i[A] = \frac{v-\% \cdot z[1] \cdot F[As/mol] \cdot \dot{n}_{CO_2}[mol/s]}{100} \tag{XII}$$

Electron transfer numbers for different gas and liquid phase products could be found in the paper from the group of Jaramillo [10].

The faradaic efficiency can then be calculated according to equation (VIII). The arithmetic mean out of three to five single measurements was calculated for each component and the total FE of gas phase products is calculated by the sum of the FE of the components.

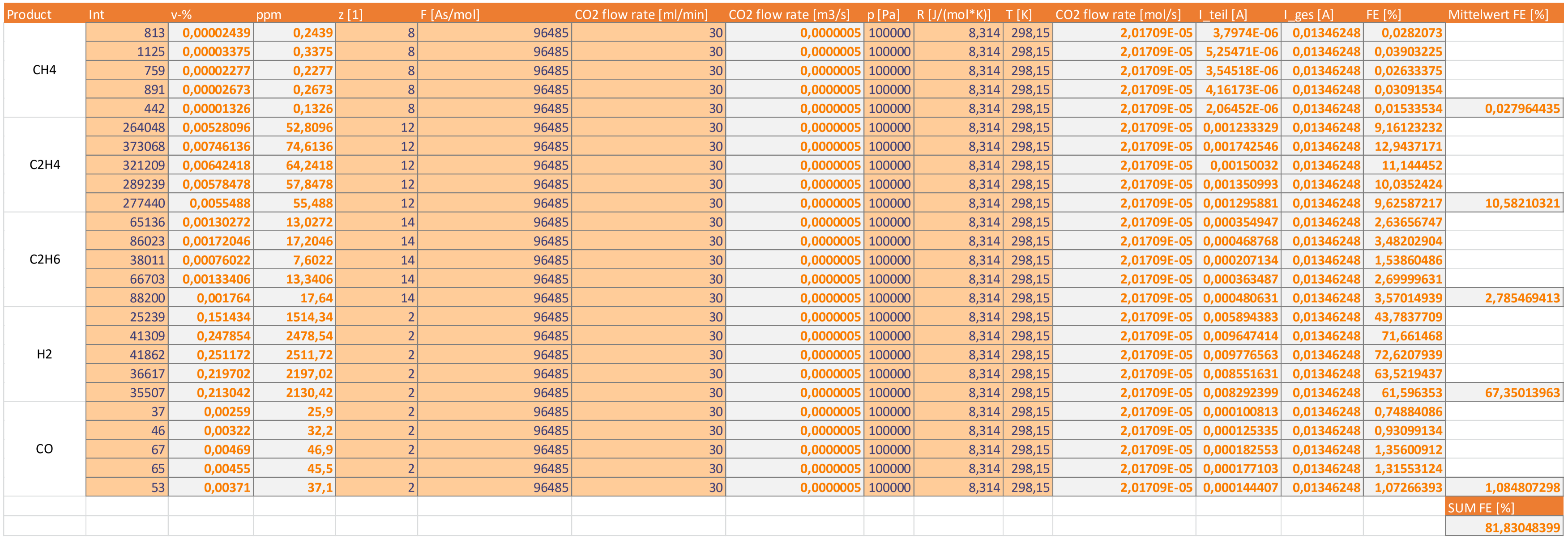

Product	Int	v-%	ppm	z [1]	F [As/mol]	CO2 flow rate [ml/min]	CO2 flow rate [m3/s]	p [Pa]	R [J/(mol*K)]	T [K]	CO2 flow rate [mol/s]	I_teil [A]	I_ges [A]	FE [%]	Mittelwert FE [%]
CH4	813	0,00002439	0,2439	8	96485	30	0,0000005	100000	8,314	298,15	2,01709E-05	3,7974E-06	0,01346248	0,0282073	
	1125	0,00003375	0,3375	8	96485	30	0,0000005	100000	8,314	298,15	2,01709E-05	5,25471E-06	0,01346248	0,03903225	
	759	0,00002277	0,2277	8	96485	30	0,0000005	100000	8,314	298,15	2,01709E-05	3,54518E-06	0,01346248	0,02633375	
	891	0,00002673	0,2673	8	96485	30	0,0000005	100000	8,314	298,15	2,01709E-05	4,16173E-06	0,01346248	0,03091354	
	442	0,00001326	0,1326	8	96485	30	0,0000005	100000	8,314	298,15	2,01709E-05	2,06452E-06	0,01346248	0,01533534	0,027964435
C2H4	264048	0,00528096	52,8096	12	96485	30	0,0000005	100000	8,314	298,15	2,01709E-05	0,001233329	0,01346248	9,16123232	
	373068	0,00746136	74,6136	12	96485	30	0,0000005	100000	8,314	298,15	2,01709E-05	0,001742546	0,01346248	12,9437171	
	321209	0,00642418	64,2418	12	96485	30	0,0000005	100000	8,314	298,15	2,01709E-05	0,00150032	0,01346248	11,144452	
	289239	0,00578478	57,8478	12	96485	30	0,0000005	100000	8,314	298,15	2,01709E-05	0,001350993	0,01346248	10,0352424	
	277440	0,0055488	55,488	12	96485	30	0,0000005	100000	8,314	298,15	2,01709E-05	0,001295881	0,01346248	9,62587217	10,58210321
C2H6	65136	0,00130272	13,0272	14	96485	30	0,0000005	100000	8,314	298,15	2,01709E-05	0,000354947	0,01346248	2,63656747	
	86023	0,00172046	17,2046	14	96485	30	0,0000005	100000	8,314	298,15	2,01709E-05	0,000468768	0,01346248	3,48202904	
	38011	0,00076022	7,6022	14	96485	30	0,0000005	100000	8,314	298,15	2,01709E-05	0,000207134	0,01346248	1,53860486	
	66703	0,00133406	13,3406	14	96485	30	0,0000005	100000	8,314	298,15	2,01709E-05	0,000363487	0,01346248	2,69999631	
	88200	0,001764	17,64	14	96485	30	0,0000005	100000	8,314	298,15	2,01709E-05	0,000480631	0,01346248	3,57014939	2,785469413
H2	25239	0,151434	1514,34	2	96485	30	0,0000005	100000	8,314	298,15	2,01709E-05	0,005894383	0,01346248	43,7837709	
	41309	0,247854	2478,54	2	96485	30	0,0000005	100000	8,314	298,15	2,01709E-05	0,009647414	0,01346248	71,661468	
	41862	0,251172	2511,72	2	96485	30	0,0000005	100000	8,314	298,15	2,01709E-05	0,009776563	0,01346248	72,6207939	
	36617	0,219702	2197,02	2	96485	30	0,0000005	100000	8,314	298,15	2,01709E-05	0,008551631	0,01346248	63,5219437	
	35507	0,213042	2130,42	2	96485	30	0,0000005	100000	8,314	298,15	2,01709E-05	0,008292399	0,01346248	61,596353	67,35013963
CO	37	0,00259	25,9	2	96485	30	0,0000005	100000	8,314	298,15	2,01709E-05	0,000100813	0,01346248	0,74884086	
	46	0,00322	32,2	2	96485	30	0,0000005	100000	8,314	298,15	2,01709E-05	0,000125335	0,01346248	0,93099134	
	67	0,00469	46,9	2	96485	30	0,0000005	100000	8,314	298,15	2,01709E-05	0,000182553	0,01346248	1,35600912	
	65	0,00455	45,5	2	96485	30	0,0000005	100000	8,314	298,15	2,01709E-05	0,000177103	0,01346248	1,31553124	
	53	0,00371	37,1	2	96485	30	0,0000005	100000	8,314	298,15	2,01709E-05	0,000144407	0,01346248	1,07266393	1,084807298
															SUM FE [%]
															81,83048399

Figure 95: Calculation template for gas phase faradaic efficiencies.

For the liquid phase analysis, the faradaic efficiencies were calculates according to the template drawn in figure 96. Out of the data for the maleic acid standard solution (volume V in µl and concentration c in mol/l), the moles of maleic acid in the NMR sample could be calculated. With the weight mass of the liquid sample m in g and the assumed density of 1 g/ml, the sample volume could be calculated in liters. With the integral of the maleic standard peak, the integral of the product peak and the proton ratio between the maleic acid peak and the used product peak, the moles of product could be calculated. The moles of the product in the whole electrolyte volume n_{ges} in mol is calculated by multiplying the moles of product in the sample volume with the ration of the electrolyte volume and the sample volume. With the faraday constant in As/mol, the electron transfer number z and the electrolysis time in s, the partial current can be calculated by the faraday law

$$I_i[A] = \frac{n_{ges}[mol] \cdot z[1] \cdot F[As/mol]}{t[s]} \qquad \text{(XIII)}$$

The faradaic efficiency can be calculated according to equation (VIII). The total FE of liquid phase products is calculated by the sum of the FE of the components. The overall sum of FE is calculated by the sum of the total FE of gas and liquid phase.

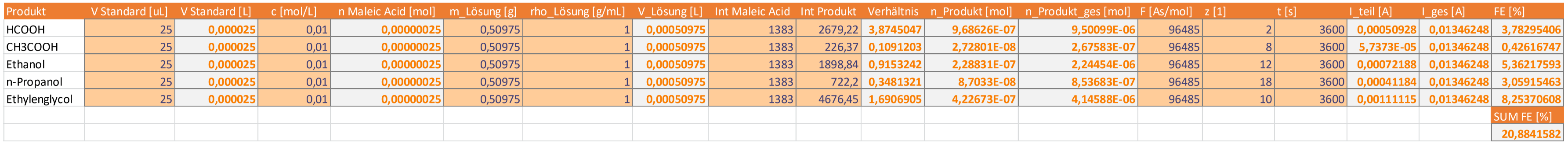

Produkt	V Standard [uL]	V Standard [L]	c [mol/L]	n Maleic Acid [mol]	m_Lösung [g]	rho_Lösung [g/mL]	V_Lösung [L]	Int Maleic Acid	Int Produkt	Verhältnis	n_Produkt [mol]	n_Produkt_ges [mol]	F [As/mol]	z [1]	t [s]	I_teil [A]	I_ges [A]	FE [%]
HCOOH	25	0,000025	0,01	0,00000025	0,50975	1	0,00050975	1383	2679,22	3,8745047	9,68626E-07	9,50099E-06	96485	2	3600	0,00050928	0,01346248	3,78295406
CH3COOH	25	0,000025	0,01	0,00000025	0,50975	1	0,00050975	1383	226,37	0,1091203	2,72801E-08	2,67583E-07	96485	8	3600	5,7373E-05	0,01346248	0,42616747
Ethanol	25	0,000025	0,01	0,00000025	0,50975	1	0,00050975	1383	1898,84	0,9153242	2,28831E-07	2,24454E-06	96485	12	3600	0,00072188	0,01346248	5,36217593
n-Propanol	25	0,000025	0,01	0,00000025	0,50975	1	0,00050975	1383	722,2	0,3481321	8,7033E-08	8,53683E-07	96485	18	3600	0,00041184	0,01346248	3,05915463
Ethylenglycol	25	0,000025	0,01	0,00000025	0,50975	1	0,00050975	1383	4676,45	1,6906905	4,22673E-07	4,14588E-06	96485	10	3600	0,00111115	0,01346248	8,25370608
																		SUM FE [%]
																		20,8841582

Figure 96: Calculation template for liquid phase faradaic efficiencies.

8.8.4. FE’s obtained with the PEEK reactor

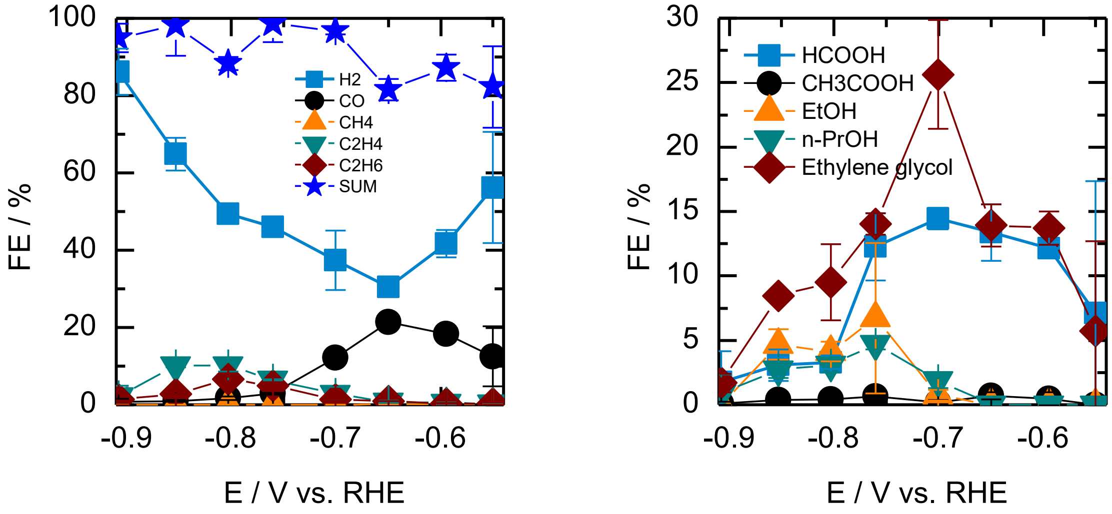

Figure 97: Gas phase (left) and liquid phase (right) FE’s for CuF-SO4-15.

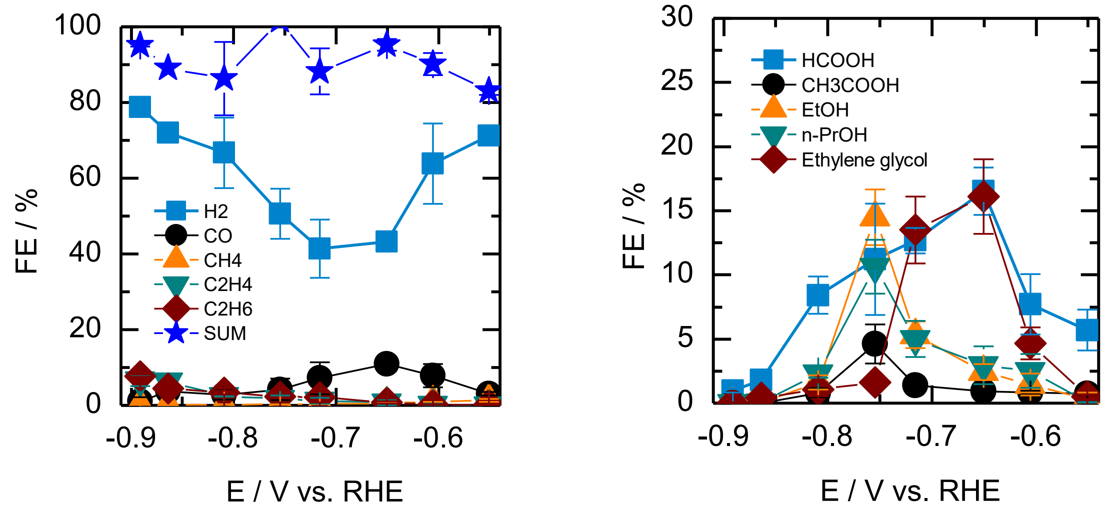

Figure 98: Gas phase (left) and liquid phase (right) FE’s for CuF-SO4-15-200.

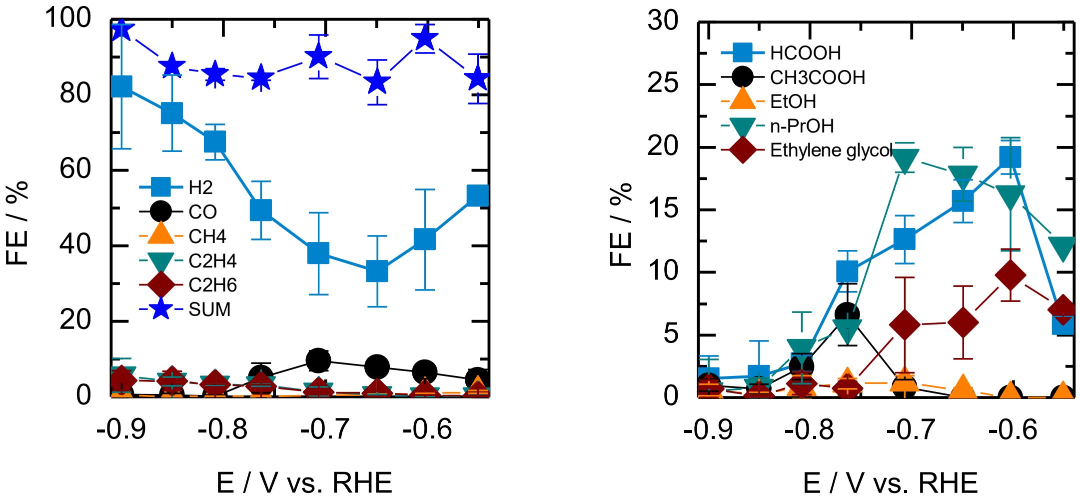

Figure 99: Gas phase (left) and liquid phase (right) FE's for CuF-SO4-15-500.

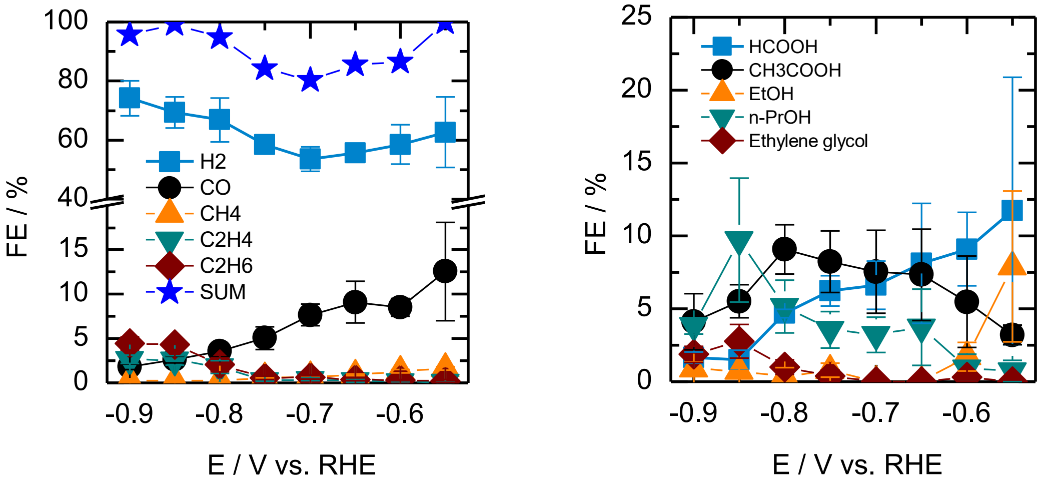

Figure 100: Gas phase (left) and liquid phase (right) FE's for CuF-SO4-15-1200.

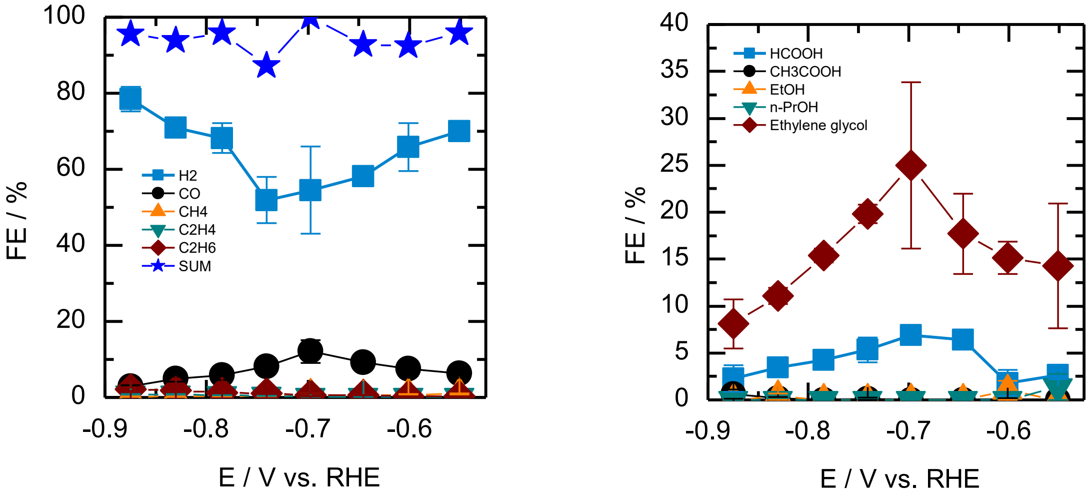

Figure 101: Gas phase (left) and liquid phase (right) FE's for CuF-SO4-40.

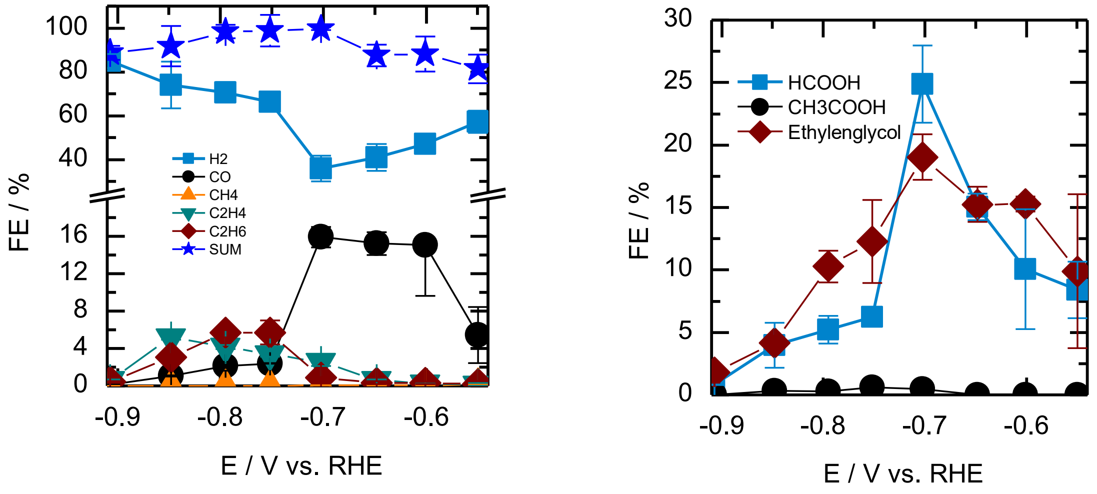

Figure 102: Gas phase (left) and liquid phase (right) FE's for SCILL-15(5)[BMIm][NTf$_2$].

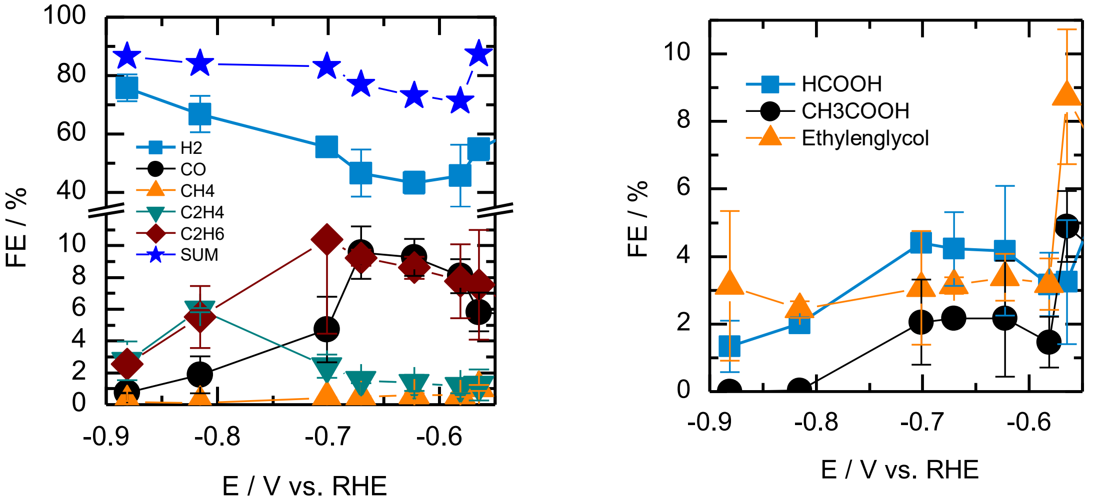

Figure 103: Gas phase (left) and liquid phase (right) FE's for SCILL-15(5)[BMMIm][NTf$_2$].

Lebenslauf

Sascha-Dominic Straub, Dipl.-Chem.

Oberneugasse 1a
68307 Mannheim-Sandhofen
Tel.: +49176/84307886
E-Mail: sascha-d.straub@gmx.de

Geburtsdatum: 14.04.1992

Geburtsort: Kaiserslautern

Familienstand: ledig

Berufserfahrung

01/2020	**Stellvertretender Produktionsleiter** der Produktion I, Lipoid GmbH, Ludwigshafen am Rhein

Promotion und Abschlussarbeit

Seit 11/2016	**Promotion** und wissenschaftlicher Mitarbeiter am Ernst-Berl-Institut für Technische und Makromolekulare Chemie an der TU Darmstadt im Arbeitskreis von Prof. Dr.-Ing. B. J. M. Etzold
	Thema: „ *Copper foam catalysts in CO2 electroreduction – Development of an experimental measuring procedure and the structural and chemical modification of the catalyst* “
09/2016	**Diplomarbeit** bei Clariant Produkte Deutschland, Frankfurt Höchst, unter Betreuung von Prof. Dr. W. R. Thiel
	Thema: „*Catalytic etherification of glycerol to higher oligomers*“

Studium und Ausbildung

Seit 2016	Abschluss als „**Diplom-Chemiker**“ mit dem Schwerpunkt Katalyse
2011 - 2016	Chemiestudium an der TU Kaiserslautern
2002 – 2011	Burggymnasium Kaiserslautern
1998 – 2002	Grundschule Kaiserslautern-Erfenbach

Weitere Tätigkeiten

02/2016 – 03/2016	Praktikum in der chemischen Industrie bei Clariant Produkte Deutschland, Frankfurt Höchst
07/2015 – 01/2016	Hilfswissenschaftlicher Mitarbeiter im Arbeitskreis von Prof. Dr. W. R. Thiel an der TU Kaiserslautern
03/2014	Betreuer im Blockpraktikum *„Allgemeine Chemie für Bio- und Chemieingenieurwesen“* an der TU Kaiserslautern
10/2013	Übungsleiter für den Vorkurs Mathematik im Fachbereich Chemie an der TU Kaiserslautern
07/2011 – 08/2011	Ferienarbeiter bei PFAFF Industriesysteme und Maschinen AG, Kaiserslautern

Weiterbildungen

07/2019	Agiles Projektmanagement
06/2019	Führungskompetenz
02/2019	Projektmanagement für Einsteiger/innen (Industrieperspektive)
05/2018	Swagelok Sicherheitsseminar „Rohre und Verschraubungen“

Sonstige Kenntnisse

Sprachen:

- Englisch (verhandlungssicher)
- Französisch (Schulkenntnisse)
- Spanisch (Grundkenntnisse)
- Schwedisch (Grundkenntnisse)
- Russisch (Grundkenntnisse)

EDV-Kenntnisse:

- MS Office (Word, Excel, PowerPoint, Access, Teams, Projects)
- Origin (Datenaufbereitung und Darstellung)
- LabVIEW (Automation, Messdatenerfassung und Verarbeitung)
- Matlab®
- Aspen Plus® (Prozesssimulation)
- Analytiksoftware für GC, HPLC und NMR (LabSolutions, Bruker TopSpin, MestReNova)
- C/C++ (Programmiersprache)
- Inventor (CAD-Modellierung)

Sonstige Kenntnisse:

- DoE (Grundkenntnisse)
- Materialflussanalyse (Grundkenntnisse)

Interessen

Fussball, Bodyweight-Fitness, Sporternährung